Biases in Cosmic Microwave Background Secondary Anisotropies Measurements

by

Hongbo Cai

Submitted to the Graduate Faculty of

the Dietrich School of Arts and Sciences in partial fulfillment

of the requirements for the degree of

Doctor of Philosophy

University of Pittsburgh

2023

UNIVERSITY OF PITTSBURGH

DIETRICH SCHOOL OF ARTS AND SCIENCES

This dissertation was presented

by

Hongbo Cai

It was defended on

September 20, 2022

and approved by

Arthur Kosowsky, Dept. of Physics and Astronomy, University of Pittsburgh

Andrew Zentner, Dept. of Physics and Astronomy, University of Pittsburgh

Jeff Newman, Dept. of Physics and Astronomy, University of Pittsburgh

Brian Batell, Dept. of Physics and Astronomy, University of Pittsburgh

Hy Trac, Dept. of Physics, Carnegie Mellon University

Biases in Cosmic Microwave Background Secondary Anisotropies Measurements

Hongbo Cai, PhD

University of Pittsburgh, 2023

The development of Cosmic Microwave Background (CMB) experiments is leading to spectacular insights into understanding the universe through the measurements of CMB secondary anisotropies. In this thesis, we demonstrate topics in CMB secondary anisotropies and extracting science from them.

In the first part of the thesis, we investigated the bias to the measurement of cosmic microwave background lensing (CMB lensing) power spectrum from the kinematic Sunyaev-Zel'dovich (kSZ) effect. We investigate for the first time the bias to CMB lensing reconstruction from temperature anisotropies due to the reionization-induced kSZ signal and show that it is negligible for both ongoing and upcoming experiments based on current numerical simulations of reionization. We also revisit the bias induced by the late-time kSZ field, using more recent kSZ simulations.

In the second part of the thesis, we present a new publicly available code, `class_rot`, which enables fast non-perturbative calculation of cosmic microwave background polarization power spectra due to both isotropic and anisotropic polarization rotation from cosmic birefringence. We describe the implementation of `class_rot` in terms of both mathematical formalism and coding architecture. We also provide usage examples and demonstrate the accuracy of the code by comparing with simulations.

In the third part of the thesis, we study how the presence of anisotropic cosmic birefringence impacts on lensing power spectrum measurements. We show that a scale-invariant cosmic birefringence with an amplitude of $A_{\rm CB} = 10^{-7}$ can induce a $1-2\%$ bias to the measured lensing power spectrum for both CMB-S3-like and CMB-S4-like experiments. Our findings suggest that a birefringence signal well below our current limit can still bias the lensing measurements by around 10% if unaccounted for. Cosmic birefringence, therefore, is potentially an important source of error to mitigate for the precision CMB lensing measure-

ments in the future.

Table of Contents

List of Tables

List of Figures

Preface

I would like to express my deepest gratitude to my supervisor Dr. Arthur Kosowsky, for his invaluable guidance, support, and mentorship throughout my research journey.

I would also like to thank the members of my thesis committee (alphabetical order), Dr. Andrew Zentner, Dr. Jeff Newman, Dr. Brian Batell and Dr. Hy Trac. Special thanks to Dr. Tao Han, Dr. Pengjie Zhang and Dr. Xinmin Zhang.

My sincere thanks to my collaborators, Mathew S. Madhavacheril, J. Colin Hill and Toshiya Namikawa. I am particularly grateful to my friend and collaborator Yilun Guan for so much inspiring discussion on physics.

Many thanks to my friends during my PhD journey (alphabetical order), Lisong Chen, Iris Leung, Andi Li, Shu Liu, Yang Ma, Qian Song, Pengshan Pan, Pok Man, Keping Xie, Qianru Yang and Bomin Zhang.

Lastly I deeply appreciate my parents, all my families and my girlfriend.

1.0 Introduction

This chapter is meant to depict a big picture of the universe and introduce the basic knowledge of modern theoretical and observational cosmology. The knowledge introduced in this chapter is not original but is the foundation of my research introduced in the following chapters. There are two sections in this chapter:

- **The Standard Model of Cosmology:** Section. 1 introduces the standard model of cosmology which is the framework of modern cosmology. Subsection. 1.1 and Subsection. 1.2 introduce the two aspects of the standard model of cosmology respectively: the homogeneous universe and the inhomogeneous universe.
- **The Cosmic Microwave Background (CMB)** In Section. 2, I will introduce how we observe the universe using a powerful tool called the Cosmic Microwave Background (CMB) which is the most ancient light in the universe generated in the process of recombination and emitted only 380,000 years after the big bang. In Subsection. 2.1, I introduce the mechanism of primary CMB including CMB temperature and polarization anisotropies. In Subsection. 2.2, I introduce briefly four secondary CMB contributions which are related directly to my work in this thesis: CMB lensing, cosmic birefringence, reionization and the Kinetic Sunyaev-Zel'dovich (kSZ) effect.

I use the natural units, in which the speed of light and Planck's constant are set equal to one $c = \hbar \equiv 1$.

1 Standard model of cosmology

We live in an expanding universe. The universe is even expanding faster and faster according to the evidence like the observation of distant supernovae [9, 10]. It must have been expanding for a very long time.

How should we explain the current stage of the universe and describe the history of the

universe? How should we understand what we observe from the universe? The concordance model of cosmology or say the Standard Model of cosmology is the ΛCDM model: a Euclidean universe dominated today by non-baryonic cold dark matter (CDM) and a cosmological parameter (Λ). None of the two ingredients are part of the Standard Model particles. Except the cold dark matter, there are other components existing in the universe like radiation and baryon particles which are less dominated than cold dark matter and cosmological parameter today, but played more important roles in the earlier times.

There are two levels of ΛCDM model: the homogeneous universe and inhomogeneous universe. The previous one refers that we consider a smooth universe as a background approximately. I will introduce it in Subsection. 1.1. The latter one adds perturbations around the smooth universe, which I will explain briefly in Subsection. 1.2. Especially according to the most plausible mechanism, these perturbations are generated in the epoch of inflation initially when the universe grew exponentially with time.

Equipped with the ΛCDM model along with the observations of CMB (Microwave Cosmic Background) and LSS (Large-scale structures), we are able to construct a timeline of the universe. The epoch in the universe can usually be characterized by different parameters like: the time since the big bang t, the scale factor a, the redshift z or the temperature of the cosmic background radiation T. For example, today, the age of universe $t \approx 13.7$ billion years, the scale factor $a = 1$, the redshift $z = 0$, and the temperature $T = 2.73K = 2.35 \times 10^{-4} eV$; The epoch of recombination when CMB photons decoupled from matter happened at $t \approx 380,000$ years, $a \approx 1/1100$, $z \approx 1100$ and $T \approx 3000K \approx 1/4eV$.

1.1 The homogeneous universe

We firstly assume that the universe is homogeneous and isotropic approximately, i.e., there is no preferred position or preferred direction. This assumption works well on very large scales (above 200Mpc) and can derive some classical results in cosmology like the age of the universe. In mathematics, the approximation of homogeneity and isotropy simplifies equations significantly, because the variables dependence of position is dropped. In this subsection in the context of a smooth universe, I will introduce briefly the geometry, the

kinematics, the dynamics along with the main constituents which make of our universe. Generally speaking, the governed rule is the general relativity, and cosmology is like the study of fluid mechanics under the influence of gravity.

1.1.1 Geometry

In general relativity, we use a generic metric $g_{\mu\nu}(t, \mathbf{x})$ to describe the universe in geometry, which returns the physical distance between two infinitesimally close points around $(t, \mathbf{x})$ in spacetime in a given coordinate. In the homogeneous universe approximation, the metric naturally does not depend on position. The Friedmann-Lemîatre-Robertson-Walker (FLRW) metric is used to describe the homogeneous expanding universe. It is convenient to express the Friedmann-Lemîatre-Robertson-Walker (FLRW) metric in spherical polar coordinate

$$ds^2 = g_{\mu\nu}dx^\mu dx^\nu = -dt^2 + a^2(t)\left(\frac{dr^2}{1-Kr^2} + r^2 d\Omega^2\right), \tag{1}$$

where t is the cosmic time, and the spatial coordinates are called the comoving coordinates, $d\Omega^2 \equiv d\theta^2 + \sin^2\theta d\phi^2$, $a(t)$ is called the scale factor, and K is the curvature parameter. It is useful to define the conformal time η by:

$$ad\eta = dt, \tag{2}$$

and the comoving distance traveled by a photon between η_i and η equals to

$$\eta - \eta_i = \int_{t_I}^{i} \frac{dt'}{a(t')}. \tag{3}$$

The advantage of using the conformal time in the comoving coordinate, as far as my understanding, is that the speed of light is still equal to 1 as it is in the physical coordinate using cosmic time. Using conformal time, then we can rewrite the FLRW metrix as

$$ds^2 = a(\eta)^2\left(-d\eta^2 + \frac{dr^2}{1-Kr^2} + r^2 d\Omega^2\right). \tag{4}$$

There is no evidence that the spatial curvature of the universe K is non-zero, but I will keep it for the sake of completeness.

1.1.2 Kinematics

How do particles move in the universe described FLRW metric? Given the spacetime, the paths of free particles can be described by the geodesic equation

$$\frac{dP^{\mu}}{d\lambda} + \Gamma_{\nu\rho}(\mathbf{x})^{\mu} P^{\nu} P^{\rho} = 0, \tag{5}$$

where $\Gamma^{\mu}_{\nu\rho}$ is the Christoffel symbol which can be obtained from the metric $g_{\mu\nu}(\mathbf{x})$ by

$$\Gamma^{\mu}_{\alpha\beta} \equiv \frac{1}{2} g^{\mu\lambda} \left(\partial_{\alpha} g_{\beta\lambda} + \partial_{\beta} g_{\alpha\lambda} - \partial_{\lambda} g_{\alpha\beta} \right) \tag{6}$$

, and λ is an affine parameter which works both for massless particles and massive particles. An important conclusion we can derive from the geodesic equation in the FLRW metric is that the energy of a massless particle is inversely proportional to the scale factor a, and hence its wavelength gets larger and larger as the universe is expanding.

1.1.3 Dynamics

How do we obtain the spacetime evolution of the universe? The evolution of the universe is governed by the General Relativity expressed by

$$G_{\mu\nu} + \Lambda g_{\mu\nu} = 8\pi G T_{\mu\nu}, \tag{7}$$

where Λ is the cosmological constant, $G_{\mu\nu}$ is the Einstein tensor, and $T_{\mu\nu}$ is the energy-momentum or energy-stress tensor.

$G_{\mu\nu}$ can be computed from the metric $g_{\mu\nu}$ given by

$$G_{\mu\nu} = R_{\mu\nu} - \frac{1}{2} R, \tag{8}$$

where $R_{\mu\nu}$ is the Ricci tensor, and R is the Ricci scalar as the contraction of the Ricci tensor (R)

The isotropic and homogeneous approximation of the universe requires that the matter content of the universe should be a perfect fluid. The energy-momentum tensor of a perfect fluid is given by

$$T_{\mu\nu} = (\rho + P) U_{\mu} U_{\nu} - P g_{\mu\nu}, \tag{9}$$

and its covariant form is

$$T^{\mu}{}_{\nu} = g^{\mu\lambda}T_{\lambda\nu} = (\rho + P)U^{\mu}U_{\nu} - Pg^{\mu}_{\nu}, \tag{10}$$

where ρ and P are the energy density and the pressure of the fluid the rest-frame of the fluid, and $U^{\mu} \equiv \frac{dX^{\mu}}{ds}$ is the relative four-velocity between the fluid and the observer. For an comoving observer in the homogeneous and isotropic universe scenario, $U^{\mu} = (1, 0, 0, 0)$, and we have

$$T^{\mu}{}_{\nu} = \begin{pmatrix} \rho & 0 & 0 & 0 \\ 0 & -P & 0 & 0 \\ 0 & 0 & -P & 0 \\ 0 & 0 & 0 & -P \end{pmatrix}. \tag{11}$$

Then, we obtain the continuity equation

$$\dot{\rho} + 3\frac{\dot{a}}{a}(\rho + P) = 0, \tag{12}$$

and the Friedmann equations

$$\left(\frac{\dot{a}}{a}\right)^2 = \frac{8\pi G}{3}\rho - \frac{K}{a^2}, \tag{13}$$

$$\frac{\ddot{a}}{a} = -\frac{4\pi G}{3}\left(\rho + 3P\right), \tag{14}$$

where the dot denotes derivation with respect to cosmic time. The Hubble parameter is defined as $H = \frac{\dot{a}}{a}$, and we can rewrite Eq. (11) as

$$H^2 = \frac{8\pi G}{3}\rho - \frac{K}{a^2}. \tag{15}$$

In the Friedmann equations, ρ and P should be the total energy density and pressure contributed by all constituents in the universe

$$\rho = \sum_i \rho_i, \quad P = \sum_i P_i. \tag{16}$$

where i can be r for radiation (γ for photons and ν for neutrinos), m for matter (c for cold dark matter, b for baryons) and λ for vacuum energy (cosmological constant). These cosmological constituents are categorized based on their different constants equation of state:

$w = P/\rho$. As a result, the corresponding energy density relations with the scale factor are different. It is easy to get the solution by plugging w into Eq. (12)

$$\rho \propto a^{-3(1+w)}, \tag{17}$$

and hence

$$\rho \propto \begin{cases} a^{-3} & \text{matter} \\ a^{-4} & \text{radiation} \\ a^{0} & \text{vacuum} \end{cases} . \tag{18}$$

Using Eq. (15), here we can define the critical density today $\rho_{\text{crit},0}$ which is the total energy density in a flat universe ($a = 1$,$K = 0$)

$$\rho_{\text{crit},0} = \frac{3H_0^2}{8\pi G}, \tag{19}$$

where H_0 is the Hubble parameter today. We can use the critical density to define dimensionless density parameters for all the constituents in the universe today:

$$\Omega_{i,0} \equiv \frac{\rho_{\text{i},0}}{\rho_{\text{crit},0}}. \tag{20}$$

From now on, I will drop the 0 in the subscripts of $\rho_{\text{crit},0}$ and $\Omega_{i,0}$ for convenience, and we can have

$$\frac{H^2}{H_0^2} = \Omega_r a^{-4} + \Omega_m a^{-3} + \Omega_\Lambda. \tag{21}$$

From Eq. (21), we can see that given the density parameters of the constituents and the Hubble parameter today, we are able to know the Hubble parameter in the history at a certain scale factor a.

1.2 The inhomogeneous universe

The assumption of homogeneous and isotropic universe is only useful on very large scales (> 200Mpc). Obviously, we are not really living in a homogeneous universe. To investigate things like the formation and evolution of structures (galaxies and their clusters), we need to consider the deviation from the homogeneous and isotropic universe, i.e., the perturbations in the FLRW metric and stress-energy tensor. The evidences from cosmic microwave background (CMB) show that CMB temperature has anisotropies at the level of a few parts in 10^5, which suggests that the perturbations are relatively small, and it is safe to apply linear perturbation theory mostly, i.e., to solve the linearized perturbed Einstein equations and Boltzmann equations.

The perturbed metric can be written as

$$g_{\mu\nu} = \bar{g}_{\mu\nu} + \delta g_{\mu\nu}, \tag{22}$$

where $\bar{g}_{\mu\nu}$ is the homogeneous FLRW metric introduced in the previous section as the background spacetime, and $\delta g_{\mu\nu}$ is the small perturbation. Similarly, we can write the perturbed stress-energy tensor with mixed indices as2

$$T^{\mu}{}_{\nu} = \bar{T}^{\mu}{}_{\nu} + \delta T^{\mu}{}_{\nu}. \tag{23}$$

We usually write the linear-order perturbed Einstein equations with mixed indices as

$$\delta G^{\mu}{}_{\nu} = 8\pi G \delta T^{\mu}{}_{\nu}. \tag{24}$$

The metric perturbation $\delta g_{\mu\nu}$ has 10 degrees of freedom. The scalar-vector-tensor (SVT) decomposition can be performed on the metric, and the 10 degree of freedom can be categorized as 4 scalar-type perturbations (1 degree of freedom for each), 2 divergenceless vector-type perturbations (2 degrees of freedom for each) and 1 divergenceless traceless rank-2 tensor-type perturbation (2 degrees of freedom). The reason why we use SVT decomposition is that the scalar, vector and tensor perturbations evolve independently in Einstein equations at linear-order, so they can be treated separately.

There are two points about the perturbed metric we need to notice. The first one is that the metric defined in Eq. (22) is not uniquely defined. We can choose different coordinates in which the corresponding metric is defined as long as the spacetime interval is invariant

$$\mathrm{d}s^2 = g_{\mu\nu}(X)\mathrm{d}X^\mu \mathrm{d}X^\nu = \tilde{g}_{\alpha\beta}(\tilde{X})\mathrm{d}\tilde{X}^\alpha \mathrm{d}\tilde{X}^\beta. \tag{25}$$

$\tilde{X}^\mu$ represents a new coordinate given by $\tilde{X}^\mu \equiv X^\mu + \xi^\mu(\tilde{X})$, where $\xi^\mu(\tilde{X})$ is a infinitesimally small vector field as the gauge generator. This implies that there are 4 redundant degrees of freedom. The second point is that perturbation values may change when coordinates change, which are not physical. Thus, we have to choose a proper scheme, in which the redundant degrees of freedom are get rid of, and the perturbations are invariant under changes of coordinates. A choice of coordinates is referred as gauge in the context of perturbation theory in relativity. In cosmology, we usually use the Newtonian Gauge. Under this gauge, 2 degrees of freedom from scalar-type perturbations as the gravitational potentials, 2 degrees of freedom from vector-type perturbations, and 2 degrees of freedom from tensor-type perturbation as the two polarizations for gravitational waves are contained. All of the perturbations are gauge-invariant.

The perturbed Einstein equation itself is not enough to depict the full picture of the inhomogeneous universe. We also need equations to describe the statistical behavior of the thermodynamics system which is not in a state of equilibrium, i.e., how the constituents in the universe evolve in the given spacetime of the universe. The evolution equations of matter and radiation are given by the perturbed Boltzmann equation which describes the spatial and direction dependence of the distribution function $f(\mathbf{x}, \mathbf{p}, t)$ with collision terms.

Armed with the background equations introduced in the previous chapter and the perturbed equations in the chapter, we are able to give the evolution of perturbations on different scales and calculate their power spectra in a certain epoch. For example, one of the most important topics is to depict matter fluctuations. Fig. 1 [1] shows the linear-theory matter power spectrum at $z = 0$ inferred from different probes (the dotted line shows the impact of non-linear clustering at $z = 0$). The black line is given by ΛCDM model which shows great agreement with data.

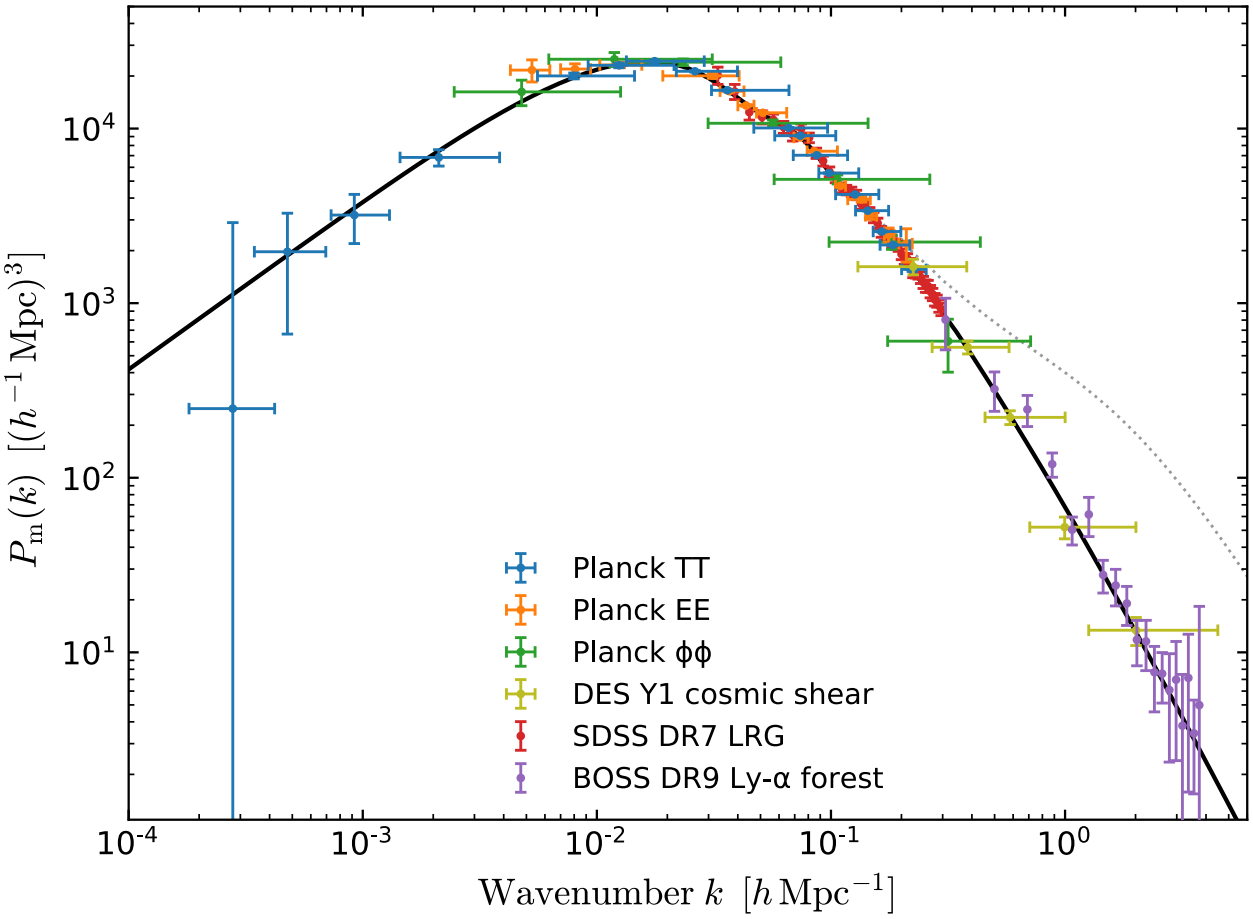

Figure 1: The (linear theory) matter power spectrum (at $z = 0$) inferred from different cosmological probes.The black line is given by ΛCDM model which shows great agreement with data. The dotted line shows the impact of non-linear clustering at $z = 0$. This figure is taken from [1]

We can use a set of cosmological parameters to describe the evolution of the universe by Lambda Cold Dark Matter (ΛCDM) model. The basic ΛCDM can be characterized by six independent cosmological parameters. Here we choose a specific combination of the six parameters,

- Baryon density $\Omega_{\rm b}h^2$
- Cold dark matter (CDM) density $\Omega_{\rm c}h^2$
- Cosmological constant (Dark energy density) Ω_Λ
- Amplitude of primordial scalar perturbations power spectrum $A_{\rm s}$
- Spectra index of primordial scalar perturbations power spectrum $n_{\rm s}$
- Optical depth due to reionization $\tau_{\rm rei}$.

The best-fit fiducial values are given in [2], in which we can find that $\Omega_{m,0} = 0.3089 \pm 0.0062$, $\Omega_{c,0} = 0.2589 \pm 0.0057$, $\Omega_\Lambda = 0.6911 \pm 0.0062$ with the 68% CL intervals. This shows that we only know well about the 5% energy content in the universe today.

There are several points I would like to mention. (1). The parameters above are constrained by the power spectrum of CMB temperature and polarization power spectra which I will introduce in the Section. sec:CMB. Partial degeneracies exist as the price this multidimensional space. (2). Some other parameters can be derived from the six parameters like the Hubble parameter H_0, the sound horizon at recombination $r_{\rm s}(\eta_*)$ and the redshift of reionization epoch $z_{\rm rei}$. Thus, the combination of the six parameters listed above is not the only option (3). In addition to the six basic, some other parameters are not directly constrained by CMB power spectra but can be better constrained by other tools. For example, CMB lensing can be used to constrain the sum of neutrino masses [a] and the curvature of the universe.

[a] Massive neutrino energy density are too small at early times but can suppress the matter overdensity power spectrum.

2 Cosmic microwave background

In the previous sections, I have introduced the homogeneous universe as the background and the inhomogeneous universe with perturbations. One would like to ask that if there is way to study the early universe and observe the inhomogeneities in that period? Fortunately, the Cosmic Microwave Background (CMB) as the oldest light of the universe provides a powerful way for us to study the early universe and probes its inhomogeneities.

Before the epoch of recombination, the photons were tightly couple to the electrons and protons as a baryon-photon fluid. In the epoch of recombination(about $380,000$ years after the big bang) when the temperature dropped below $1eV$ which is not high enough to maintain the equilibrium, photons decoupled with electrons. As a result, free electrons fraction dropped dramatically and photons free-screamed from the last scattering surface as the CMB photons we observe today. The observed CMB temperature is pretty uniform corresponding to a blackbody spectrum of about $2.725K$. But there are still little anisotropies fluctuating at the level of $1/10^5$. These anisotropies of CMB reflect directly the inhomogeneities in the epoch of recombination and the physics in the early universe, and its power spectra allows us to determine things like the cosmological parameters.

Because my work presented in this thesis is centered around how to extract information from CMB, it is necessary to introduce CMB carefully and include some calculation details. I will firstly introduce the primary CMB in Subsection. 2.1, and four CMB secondary contributions in the post-recombination era which are related to my work in Subsection. 2.2.

2.1 Primary CMB

2.1.1 CMB temperature anisotropies

We usually use $\Theta(\hat{\mathbf{n}}) = \delta T(\hat{\mathbf{n}})/T$ to denote the CMB temperature anisotropies. We can use spherical harmonics to decompose $\Theta(\hat{\mathbf{n}})$ as

$$\Theta(\hat{\mathbf{n}}) = \sum_{l=0}^{\infty} \sum_{m=-l}^{l} a_{\mathrm{T},\ell m} Y_{\ell m}(\hat{\mathbf{n}}), \tag{26}$$

where the T in the subscript of $a_{\mathrm{T},\ell m}$ denotes temperature field. Taking advantage of the orthonormality of spherical harmonics

$$\int d^2\hat{\mathbf{n}} Y_{\ell m}(\hat{\mathbf{n}}) Y^*_{\ell' m'}(\hat{\mathbf{n}}) = \delta_{\ell\ell'}\delta_{mm'}, \tag{27}$$

Eq. (26) can be inverted as

$$a_{\mathrm{T},\ell m} = \int d\Omega\ \Theta(\hat{\mathbf{n}}) Y^*_{\ell m}(\hat{\mathbf{n}}). \tag{28}$$

For pure Gaussian perturbations, the expectation and variance of $a_{\mathrm{T},\ell m}$ are given by

$$\langle a_{\mathrm{T},\ell m}\rangle = 0,\ \langle a_{\mathrm{T},\ell m} a^*_{\mathrm{T},\ell' m'}\rangle = \delta_{\ell\ell'}\delta_{mm'} C_{\mathrm{TT},\ell}, \tag{29}$$

where $C_{\mathrm{TT},\ell}$ is the CMB temperature power spectrum.

Next we take a look at how we figure $\Theta(\hat{\mathbf{n}})$ in Eq. (28) mathmatically. Firstly, we need to realize that $\Theta(\hat{\mathbf{n}})$ represents the temperature anisotropies at this moment where we observe them (i.e. the Earth). Hence, it is more intuitive to express it as

$$\Theta(\hat{\mathbf{n}}) \to \Theta(\eta_0, \mathbf{x}_0, \hat{\mathbf{p}}), \tag{30}$$

where η_0 is the conformal time for now, $\mathbf{x}_0$ is our location, and $\hat{\mathbf{n}} = -\hat{\mathbf{p}}$ represents our line-of-sight which is opposite to the direction of incoming photons. We firstly fix the spatial variables using Fourier transformation by

$$\Theta(\eta_0, \mathbf{x}_0, \hat{\mathbf{p}}) = \int \frac{d^3\mathbf{k}}{(2\pi)^3} \Theta(\eta_0, \mathbf{k}, \hat{\mathbf{p}}) e^{i\mathbf{k}\cdot\mathbf{x}}. \tag{31}$$

As introduced in the Subsection. 1.2, the scalar, vector and tensor perturbations evolve independently at linear-order. Vector perturbations decayed very fast in the expanding spacetime, and scalar perturbations contribute much more than tensor perturbations. I will firstly introduce scalar-perturbation contribution $\Theta^{(\mathrm{S})}(\eta_0, \mathbf{k}, \hat{\mathbf{p}})$ and then tensor-perturbation contribution $\Theta^{(\mathrm{T})}(\eta_0, \mathbf{k}, \hat{\mathbf{p}})$.

For scalar perturbations, we usually renormalize $\Theta^{(\mathrm{S})}(\eta_0, \mathbf{k}, \hat{\mathbf{p}})$ using the primordial Gaussian scalar perturbation mode $R(\eta, \mathbf{k})$ by $\Theta(\eta_0, \mathbf{k}, \hat{\mathbf{p}}) = R(\mathbf{k})\Theta^{(\mathrm{S})}(\eta_0, k, \hat{\mathbf{p}})$, where $\Theta(\eta_0, k, \hat{\mathbf{p}})$ does not depend on the direction of $\mathbf{k}$. Then we fix the variables of direction. For scalar

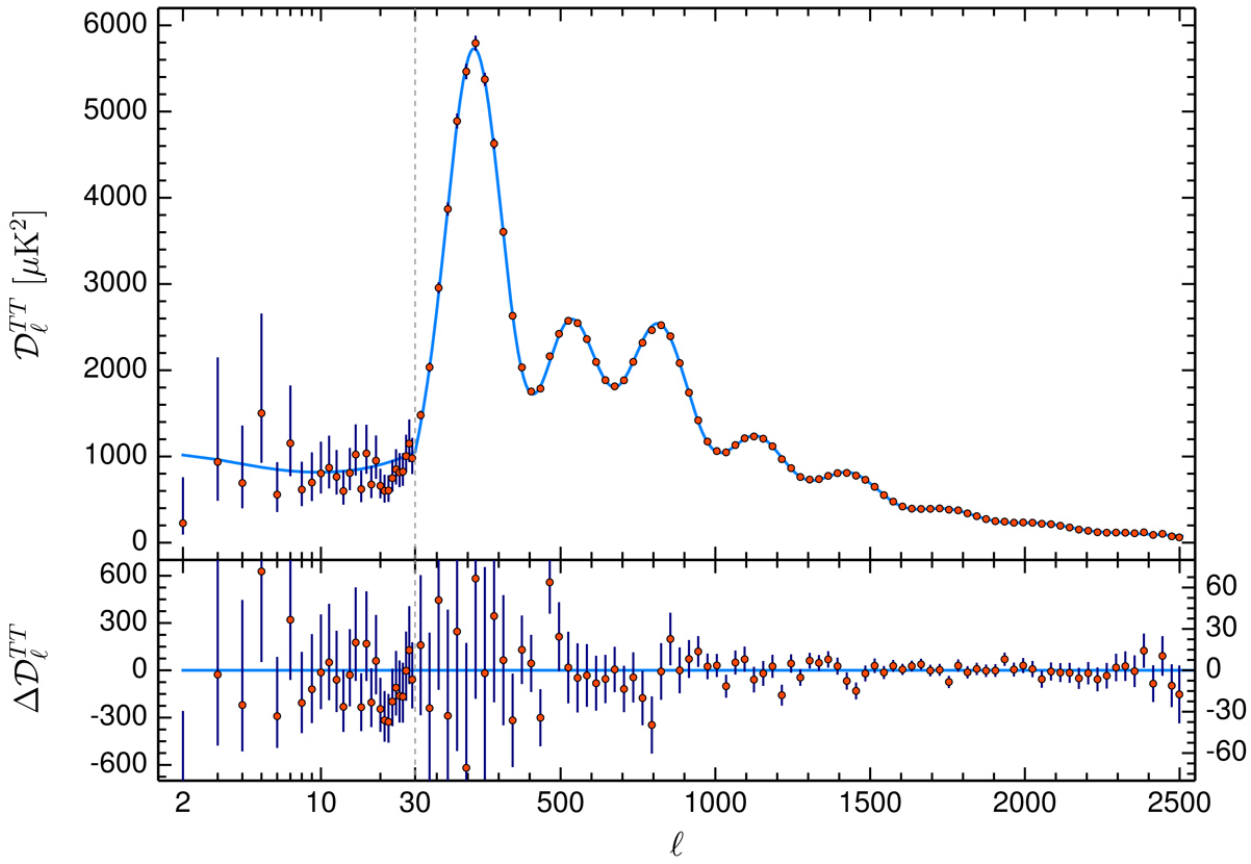

Figure 2: CMB temperature power spectrum taken from Planck 2018 results [2]. In the upper panel, the blue line represents the best-fit ΛCDM Planck 2018 model, based on the combination of TT, TE and EE. In the lower panel, the blue line represents the residuals with respect to this model. The error bars show $\pm 1\sigma$ diagonal uncertainties, including cosmic variance (approximated as Gaussian) and not including uncertainties in the foreground model at $\ell \geq 30$.

perturbations, $\Theta^{(\mathrm{S})}(\eta_0, k, \hat{\mathbf{p}})$ is axially symmetric, and we can have $\hat{\mathbf{k}} \cdot \hat{\mathbf{p}} = \mu = -\hat{\mathbf{k}} \cdot \hat{\mathbf{n}}$ and use partial wave expansion as

$$\Theta^{(\mathrm{S})}(\eta_0, k, \mu) = \sum_{\ell} (-i)^{\ell} (2\ell + 1) P_{\ell}(\mu) \Theta_{\ell}^{(\mathrm{S})}(\eta_0, k), \tag{32}$$

where $P_\ell(\mu)$ is the Legendre polynomial, and the superscript S denotes the contribution by scalar perturbations.

So far, we have only considered the CMB temperature anisotropies purely geometrically. We then connect $\Theta_\ell^{(\mathrm{S})}(\eta_0, k)$ to the physics in the early universe and the inhomogeneities at the period of recombination. We apply the line-of-sight integration technique, in which we assume the photons traveled approximately alone the line-of-sight for simplicity. We will also use the same technique for tensor perturbation contribution and CMB polarization later. We have

$$\Theta_{\ell}^{(\mathrm{S})}(\eta_0, k) = \int_0^{\eta_0} d\eta S_{\mathrm{T}}^{(\mathrm{S})}(\eta, k) j_{\ell}\left[k\left(\eta_0 - \eta\right)\right], \tag{33}$$

where $S_{\mathrm{T}}^{(\mathrm{S})}(\eta, k)$ is the source term for CMB temperature, which encapsulates the historical information of the universe for scalar perturbations from the end of inflation $\eta_{\mathrm{i}} = 0$ to now, and $j_\ell\left[k\left(\eta_0 - \eta\right)\right]$ is spherical Bessel function as a weight function. $S_{\mathrm{T}}^{(\mathrm{S})}(\eta, k)$ can be expressed as

$$S_{\mathrm{T}}^{(\mathrm{S})}(\eta, k) \equiv \left(\Psi' - \Phi'\right) e^{-\tau} + g\left(\Theta_0 + \frac{\Pi}{4} + \Psi\right) + \frac{1}{k}\left(g V_{\mathrm{b}}\right)' + \frac{3}{4k^2}(g\Pi)'', \tag{34}$$

where $\Pi = \Theta_2 + \Theta_{P2} + \Theta_{P0}$ demonstrating the inhomogeneities and anisotropies of the universe, and $g(\eta)$ is the visibility function given by

$$g(\eta) \equiv -\tau' e^{-\tau} \tag{35}$$

representing the Possionian probability that a photon is last scattered at η.

The visibility function $g(\eta)$ as a function of redshift z is shown in Fig. 3. The very top peak at round $z = 1000$ represents recombination when CMB photons decoupled with electrons. Obviously, recombination contributes most of the last-scattered CMB photons, and we can assume approximately photons are in the phase of free-streaming after recombination though there are several secondary foreground effects which may scattered photons

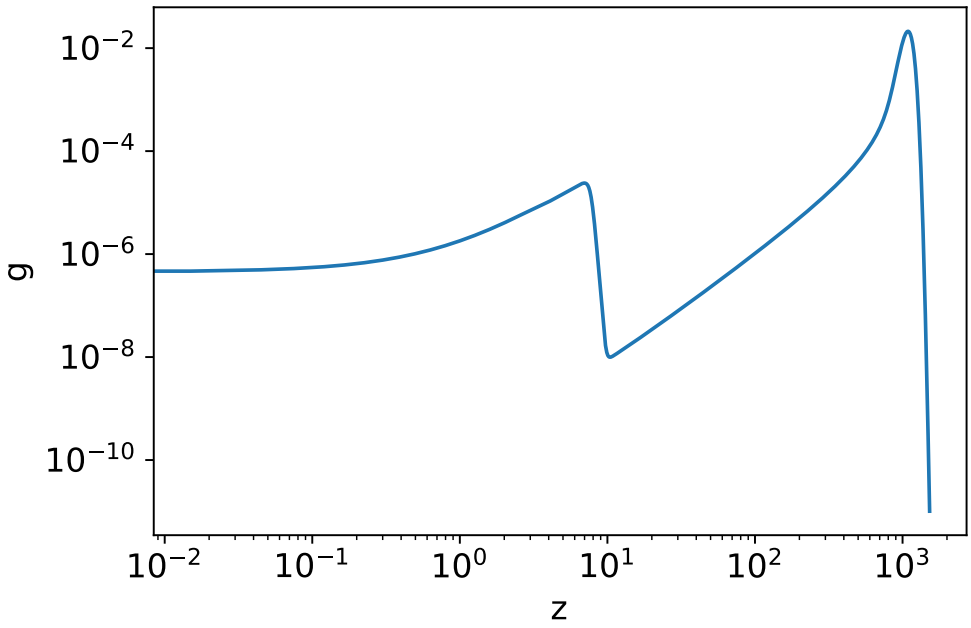

Figure 3: Visibility function g as a function of the redshift z. The result is calculated by `CLASS` [3] numerically with ΛCDM model. The very top peak at round $z = 1000$ represents recombination, and the peak at about $z = 10$ represents the epoch of reionization.

like reionization, which corresponds to the other peak at about $z = 10$ in Fig. 3. And I will discuss those secondary CMB contributions which are related to my work in this thesis briefly in next subsection.

The CMB temperature power spectrum contributed by scalar perturbations can be given by

$$C_{\mathrm{TT},\ell}^{(\mathrm{S})} = \frac{2}{\pi} \int dk k^2 \left|\Theta_\ell\left(\eta_0, k\right)\right|^2 P_{\mathcal{R}}(k) = 4\pi \int \frac{dk}{k} \left|\Theta_\ell^{(\mathrm{S})}\left(\eta_0, k\right)\right|^2 \Delta_{\mathrm{R}}^2(k) \tag{36}$$

where $\Delta_{\mathcal{R}}^2(k)$ is the power spectrum of primordial curvature perturbation as initial condition determined by inflation. In the experiments, we measure CMB power spectra as observables. Take the temperature power spectrum for example, its unbiased estimator is given by

$$\widehat{C}_{\mathrm{TT},\ell} = \frac{1}{2\ell+1} \sum_{m=-\ell}^{\ell} |a_{\mathrm{T},\ell m}|^2, \tag{37}$$

where sum indicates that each ℓ mode in $C_{\mathrm{TT},\ell}$ is estimated by $2\ell + 1$ measurements, and the variance of $\widehat{C}_{\mathrm{TT},\ell}$ is given by

$$\sigma^2(C_\ell) = \frac{2}{(2\ell+1) f_{\mathrm{sky}}} C_\ell, \tag{38}$$

where f_{sky} is fraction of the sky covered by the experiment. In Fig. 2, the CMB temperature power spectrum measured by Planck [2] is shown. In the upper panel, the blue line represents the best-fit ΛCDM Planck 2018 model, based on the combination of TT, TE and EE. In the lower panel, the blue line represents the residuals with respect to this model. The error bars show $\pm 1\sigma$ diagonal uncertainties, including cosmic variance (approximated as Gaussian) and not including uncertainties in the foreground model at $\ell \geq 30$. The cosmic variance shown in Fig. 2 is consistent with the theoretical expression given in Eq. (38). There are several features of CMB temperature power spectrum I would like to introduce below

- The most significant features are the peaks and troughs. These fluctuations of power spectrum are caused by the baryon acoustic oscillations (BAO), in which photons were coupled tightly with the electron-proton as the baryon-photon fluid through Compton scattering. The fluid propagated with the sound-speed as the sound-wave. The essence of CMB is to project the spatial fluctuations of photon and gravitational potentials distributions at recombination (contributed mostly by $(\Theta_0 + \Psi)(\eta_*, k)$) to the angular

fluctuations of photon distribution now (CMB today). Hence, the peaks of CMB power spectrum reflect directly the overdensity and the corresponding quantities in the epoch of recombination. For example, the first and the highest peak is at $\ell \approx 220$ or $\approx 0.5^\circ$ in angle, corresponding to the sound horizon which is the furthest distance the sound-wave traveled before recombination determined by the baryon-to-photon energy ratio $R \equiv \frac{3\rho_b}{4\rho_\gamma}$. The peaks height can be determined by things like the cold matter energy density, the baryon energy density and optical depth of reionization.

- At very large scales ($\ell < 30$), the CMB power spectrum is approximate flat. These scales are larger than the horizon at recombination, and hence did not involve the baryon acoustic oscillations. They can reflect directly the amplitude and index of primordial scalar perturbations. The significant variance at these scales are due to cosmic variance.
- At small scales ($\ell > 1500$), the CMB power spectrum decays exponentially, which is caused by the Silk damping. At these scales, the corresponding Fourier mode wavelengths become smaller than the mean free path length of the photon-electron scattering, and hence the scattering does not reflect density perturbations any more or say it washes out the density perturbations.

Then we focus on the tensor perturbations. As Fig. 4 shows, the contribution to CMB TT power spectrum from tensor perturbations is much smaller than scalar perturbations. The tensor contribution (Fourie mode) is $\Theta^{(\mathrm{T})}(\eta_0, \mathbf{k}, \hat{\mathbf{n}})$ and can be renormalized by the primordial tensor mode as $\Theta^{(\mathrm{T})}(\eta_0, \mathbf{k}, \hat{\mathbf{n}}) = \Theta^{(\mathrm{T})}(\eta_0, k, \mu, \phi)\beta(\mathbf{k}, \lambda)$, where

$$\langle \beta(\mathbf{k}, \lambda)\beta^* (\mathbf{k}', \lambda')\rangle = (2\pi)^3 P_h(k)\delta_{\lambda\lambda'}\delta^{(3)} (\mathbf{k} - \mathbf{k}') . \tag{39}$$

Different from the scalar perturbations in Eq. (32), tensor perturbation modes are not axially symmetric. So we need to separate them as

$$\begin{aligned}
\Theta^{(\mathrm{T})}(\eta_0, k, \mu, \phi) &= \Theta^{(\mathrm{T})}_+(\eta_0, k, \mu) \left(1 - \mu^2\right) \cos 2\phi + \Theta^{(\mathrm{T})}_\times(\eta_0, k, \mu) \left(1 - \mu^2\right) \sin 2\phi \\
&= 4\sqrt{\frac{\pi}{15}} \sum_{\lambda=\pm 2} \Theta^{(\mathrm{T})}(\eta_0, k, \mu) Y_{2\lambda}(\mu, \phi) \\
&= \sum_{\lambda=\pm 2} f_\lambda(\eta_0, k, \mu, \phi),
\end{aligned} \tag{40}$$

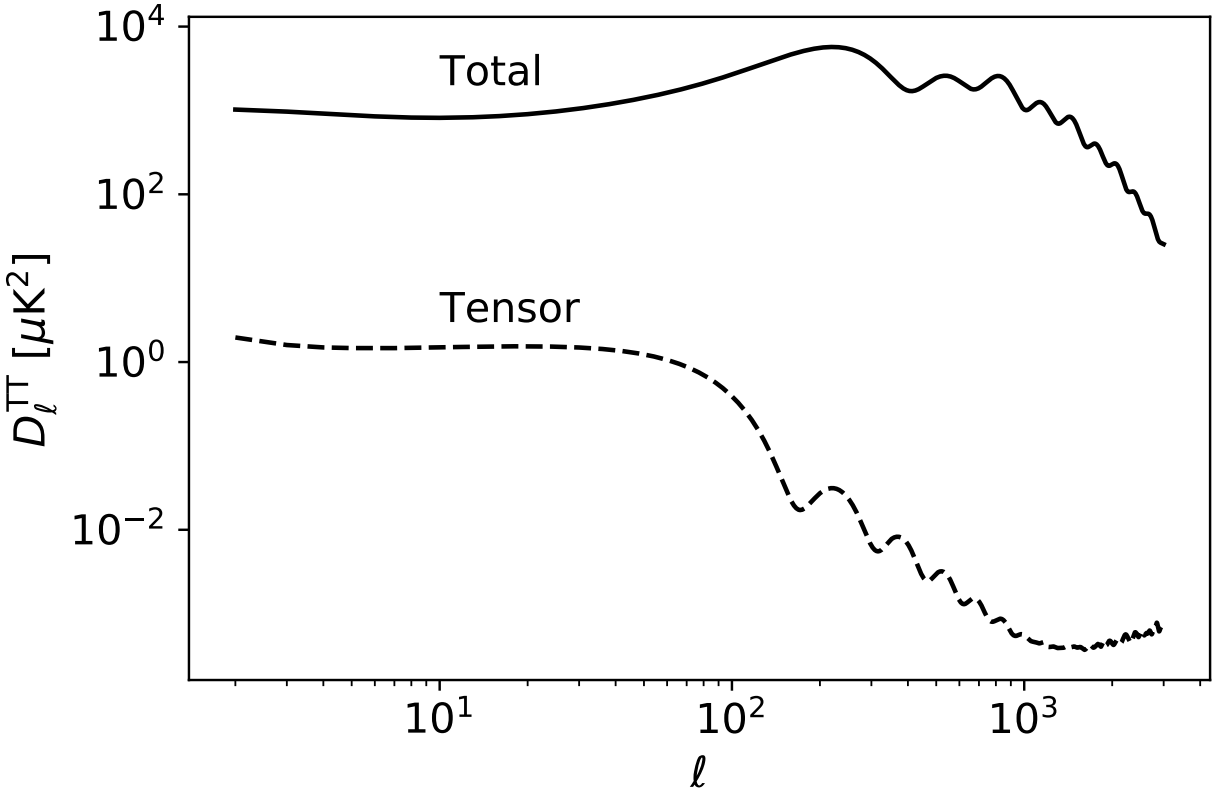

Figure 4: The total (solid line) and tensor (dotted line) CMB TT power spectra calculated by `CLASS` [3] numerically. The power spectra are multiplied by a factor of $\ell(\ell+1)/2\pi$

where

$$f_\lambda(\eta_0, k, \mu, \phi) = 4\sqrt{\frac{\pi}{15}}\Theta^{(\mathrm{T})}(\eta_0, k, \mu)Y_{2\lambda}(\mu, \phi), \tag{41}$$

and the spherical harmonics $Y_{2\lambda}(\mu, \phi)$ (corresponding to the two helicities of gravitational waves) absorb the dependence of ϕ angle, so we can focus on the evolution of $\Theta^{(\mathrm{T})}(\eta_0, k, \mu)$ which only depends on μ. The label λ represents the two possible states of helicity which are determined by tensor perturbations, and can be absorbed by the initial tensor mode $\beta(\mathbf{k}, \lambda)$. Similar to Eq. (33), we can use the line-of-sight integral to give

$$\Theta^{(\mathrm{T})}(\eta_0, k, \mu) = \int_0^{\eta_0} d\eta e^{ik\mu(\eta-\eta_0)-\tau} S_{\mathrm{T}}^{(\mathrm{T})}(\eta, k), \tag{42}$$

and the TT power spectrum contributed by tensor mode can be expressed as

$$C_{\mathrm{TT},\ell}^{(\mathrm{T})} = \frac{(\ell+2)!}{4\pi(\ell-2)!}\int_0^\infty \frac{dk}{k}\Delta_{\mathrm{h}}^2(k)\left|\int_0^{\eta_0} d\eta S^{\mathrm{T}}(\eta, k)\frac{j_\ell(kr)}{(kr)^2}\right|^2 \tag{43}$$

2.1.2 CMB polarizations anisotropies

In the previous subsection, we focus on the CMB temperature anisotropies . Can we exploit more information from CMB photons? Fortunately, linear polarization anisotropies can be produced by Thomson scattering in the process of recombination which does not take place instantaneously.

The linear polarization can be described by two Stokes parameters Q and U, which are measured by a set of orthogonal polarizers as basis. We usually use the combinations $Q \pm U$ because they have helicity 2

$$(Q \pm iU) \to e^{\pm 2i\theta}(Q \pm iU), \tag{44}$$

where θ is rotation angle of polarization plane.

As we can see from Eq. (44), Q and U are defined by the local polarizers, which change as the basis rotates, which implies that they are not physical, and we have to consider the CMB polarization globally and defined more physical quantities which are scalars or at least pseudoscalars. So we will discuss CMB polarizations in the spherical coordinate system which is compatible with CMB observation, and we can imagine the polarizations on the

sphere. The polarizer basis on the sphere are defined as $(\hat{\mathbf{e}}_\theta, \hat{\mathbf{e}}_\phi)$. It is naturally to use spin 2-weighted spherical harmonics [11] to expand them as [12, 13]

$$\begin{aligned}(Q+iU)(\hat{\mathbf{n}}) &= \sum_{\ell=2}^{\infty}\sum_{m=-\ell}^{\ell} a_{\mathrm{P},\ell m}\ {}_2Y_{\ell m}(\hat{\mathbf{n}}) \\ (Q-iU)(\hat{\mathbf{n}}) &= \sum_{\ell=2}^{\infty}\sum_{m=-\ell}^{\ell} a^*_{\mathrm{P},\ell m}\ {}_2Y^*_{\ell m}(\hat{\mathbf{n}}),\end{aligned} \tag{45}$$

, and the E and B-mode multipoles are given by

$$a_{\mathrm{E},\ell m} = -\left(a_{\mathrm{P},\ell m} + a^*_{\mathrm{P},\ell -m}\right)/2, \quad a_{\mathrm{B},\ell m} = i\left(a_{\mathrm{P},\ell m} - a^*_{\mathrm{P},\ell -m}\right)/2. \tag{46}$$

The E and B-mode maps in the real space on the sphere can be expressed as

$$\begin{aligned}E(\hat{\mathbf{n}}) &= \sum_{l=0}^{\infty}\sum_{m=-l}^{l} a_{\mathrm{E},\ell m} Y_{\ell m}(\hat{\mathbf{n}}) \\ B(\hat{\mathbf{n}}) &= \sum_{l=0}^{\infty}\sum_{m=-l}^{l} a_{\mathrm{B},\ell m} Y_{\ell m}(\hat{\mathbf{n}})\end{aligned} \tag{47}$$

It is easy to check that $E(\hat{\mathbf{n}})$ is a scalar, and $B(\hat{\mathbf{n}})$ is a pseudoscalar which gains a (-1) under spatial reflection transformation. We can give CMB polarization and cross power spectra as

$$\begin{aligned}&\langle a_{\mathrm{E},\ell m} a^*_{\mathrm{E},\ell' m'}\rangle = \delta_{\ell\ell'}\delta_{mm'} C_{\mathrm{EE},\ell},\ \langle a_{\mathrm{B},\ell m} a^*_{\mathrm{B},\ell' m'}\rangle = \delta_{\ell\ell'}\delta_{mm'} C_{\mathrm{BB},\ell}, \\ &\langle a_{\mathrm{T},\ell m} a^*_{\mathrm{E},\ell' m'}\rangle = \delta_{\ell\ell'}\delta_{mm'} C_{\mathrm{TE},\ell}, \\ &\langle a_{\mathrm{T},\ell m} a^*_{\mathrm{B},\ell' m'}\rangle = \delta_{\ell\ell'}\delta_{mm'} C_{\mathrm{TB},\ell},\ \langle a_{\mathrm{E},\ell m} a^*_{\mathrm{B},\ell' m'}\rangle = \delta_{\ell\ell'}\delta_{mm'} C_{\mathrm{EB},\ell},\end{aligned} \tag{48}$$

It is more straightforward to demonstrate the difference between E-mode and B-mode by plotting the polarization patterns generated by a pure E-mode and B-mode signal from a single multipole as shown in Fig. 5, in which you can see that B-mode signal is not left-right symmetric, featuring a different parity with E-mode. Intuitively, we may realize that the B-mode pattern might be caused by something mechanism different from what induces E-mode pattern. This is right because in the process of recombination B-mode can only be generated when there exist tensor perturbations or say primordial gravitational waves [14]. Like the previous subsection, I will discuss the contributions from scalar perturbations and tensor perturbations to CMB polarization respectively, and conclude what makes B-mode

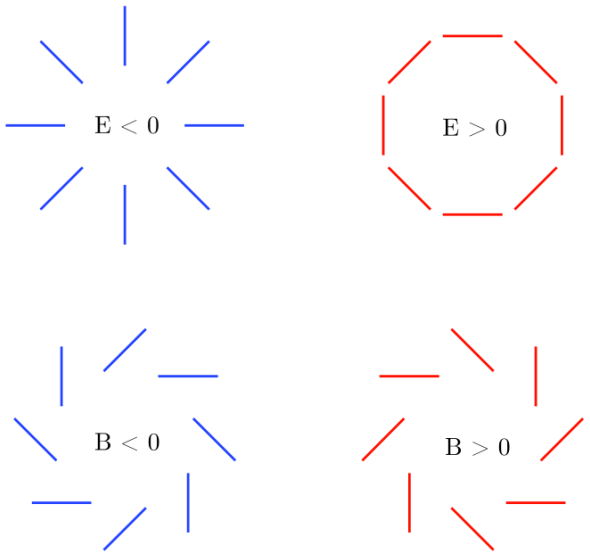

Figure 5: An illustration of polarization E- and B-modes which shows the different parities of E- and B-modes. Image is taken from [4].

so unique. I still use the line-of-sight technique for the polarization calculation like the temperature anisotropies calculation in the previous subsection.

Physically, CMB polarizations are produced by Thomson scattering (the low-energy limit of Compton scattering) in the process of recombination. Like usual, we use Fourier expansion to separate the spatial component like

$$\Theta_{\rm P}(\eta_0, \mathbf{x}_0, \hat{\mathbf{n}}) = \int \frac{d^3\mathbf{k}}{(2\pi)^3} \Theta_{\rm P}(\eta_0, \mathbf{k}, \hat{\mathbf{n}}) e^{i\mathbf{k}\cdot\mathbf{x}}, \tag{49}$$

where $\Theta_{\rm P}(\eta_0, \mathbf{x}_0, \hat{\mathbf{n}})$ can represent both Q and U maps.

Firstly we take a look at the scalar perturbation contributions by a single Fourier mode $\Theta_{\rm P}^{(\rm S)}(\eta_0, \mathbf{k}, \hat{\mathbf{n}})$. We have chosen a reference frame in which $\hat{\mathbf{k}} = \hat{\mathbf{n}}$. With only scalar perturbations, the polarizations produced by Thomson scattering is axially-symmetric, so it is safe to use partial wave expansion as

$$\Theta_{\rm P}^{(\rm S)}(\eta_0, k, \mu) = \sum_\ell (-i)^\ell (2\ell+1) P_\ell(\mu) \Theta_{{\rm P}\ell}^{(\rm S)}(\eta_0, k). \tag{50}$$

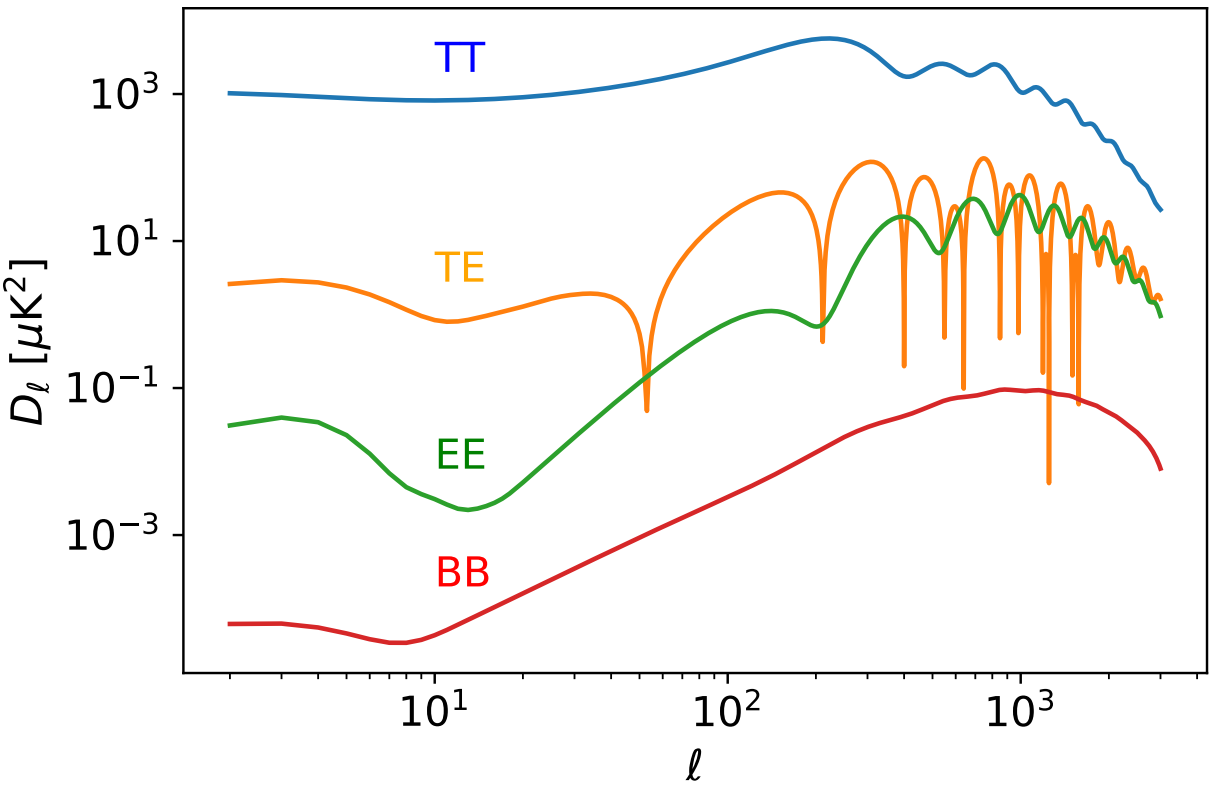

Figure 6: The CMB TT, TE, EE, BB power spectra are shown above. All the spectra are calculated by `CLASS` [3] numerically and have been multiplied by a factor of $\ell(\ell+1)/2\pi$.

We have $\Theta_{\rm P}^{(\rm S)}(\eta_0,\mathbf{k},\hat{\mathbf{n}}) = Q_{\rm P}(\eta_0,\mathbf{k},\hat{\mathbf{n}})$ in this frame according to the symmetry. Similar to Eq. (33), we can express $\Theta_{{\rm P}\ell}^{(\rm S)}(\eta_0,k)$ as

$$\Theta_{{\rm P}\ell}^{(\rm S)}(\eta_0,k) = \int_0^{\eta_0} d\eta S_{\rm P}(\eta,k) j_\ell\left[k\left(\eta_0-\eta\right)\right], \tag{51}$$

where $S_{\rm P}^{(\rm S)}(\eta,k)$ is the source term for polarization with scalar perturbations, which plays a similar role as $S_{\rm T}^{(\rm S)}(\eta,k)$ plays in Eq. (33). The power spectra contributed by scalar perturbations are given by

$$C_{{\rm EE},\ell}^{(\rm S)} = \frac{9}{64\pi}\frac{(\ell+2)!}{(\ell-2)!}\int\frac{dk}{k}\Delta_{\rm R}^2\left|\int_0^{\eta_0} d\eta S_{\rm P}^{(\rm S)}(\eta,k)\frac{j_\ell(kr)}{(kr)^2}\right|^2 \tag{52}$$

$$C_{{\rm BB},\ell}^{(\rm S)} = 0 \tag{53}$$

$$C_{{\rm TE},\ell}^{(\rm S)} = -\frac{3}{4}\sqrt{\frac{(\ell+2)!}{(\ell-2)!}}\int\frac{dk}{k}\Delta_{\rm R}^2\Theta_\ell(k)\int_0^{\eta_0} d\eta S_{\rm P}^{(\rm S)}(\eta,k)\frac{j_\ell(kr)}{(kr)^2} \tag{54}$$

Then we discuss the contribution from tensor perturbation to CMB polarization. Like Eq. (42), there is no axial symmetry, so we have

$$\begin{aligned}\Theta_{\rm P}^{(\rm T)}(\eta_0,k,\mu,\phi) &= \Theta_{\rm P+}^{(\rm T)}(\eta_0,k,\mu)\left(1+\mu^2\right)\cos 2\phi + \Theta_{\rm P\times}^{(\rm T)}(\eta_0,k,\mu)\left(1+\mu^2\right)\sin 2\phi \\ &= 4\sqrt{\frac{\pi}{15}}\sqrt{\frac{3}{2}}\sum_{\lambda=\pm 2}\Theta_{\rm P}^{(\rm T)}(\eta_0,k,\mu)\mathcal{E}_\lambda(\mu,\phi),\end{aligned} \tag{55}$$

where

$$\Theta_{\rm P}^{(\rm T)}(\eta_0,k,\mu) = \int_0^{\eta_0} d\eta e^{ik\mu(\eta-\eta_0)} S_{\rm P}^{(\rm T)}(\eta,k). \tag{56}$$

The power spectra contributed by tensor perturbations are given by

$$C_{{\rm EE},\ell}^{(\rm T)} = \int\frac{dk}{4\pi k}\Delta_{\rm h}^2(k)\left|\int_0^{\eta_0} d\eta S_{\rm P}^{(\rm T)}(\eta,k)\left[\frac{2}{kr}j_\ell' - 2j_\ell + \frac{2+\ell(\ell+1)}{(kr)^2}j_\ell\right]\right|^2, \tag{57}$$

$$C_{{\rm BB},\ell}^{(\rm T)} = \int\frac{dk}{4\pi k}\Delta_h^2\left|\int_0^{\eta_0} d\eta S_P^T(\eta,k)\left(2j_\ell' + \frac{4}{kr}j_\ell\right)\right|^2, \tag{58}$$

and

$$C_{\mathrm{TE},\ell}^{(\mathrm{T})} = -\sqrt{\frac{(\ell+2)!}{(\ell-2)!}} \int \frac{dk}{8\pi k} \Delta_{\mathrm{h}}^2(k) \int_0^{\eta_0} d\eta S^{(\mathrm{T})}(\eta, k) \frac{j_\ell}{(kr)^2} \\ \int_0^{\eta_0} d\eta' S_{\mathrm{P}}^{(\mathrm{T})}(\eta', k) \left[\frac{2}{kr} j_\ell' - 2j_\ell + \frac{2+\ell(\ell+1)}{(kr)^2} j_\ell \right]. \tag{59}$$

The parity-odd power spectra $C_{\mathrm{TB},\ell}$ and $C_{\mathrm{EB},\ell}$ are zero according to the parities of E- and B-modes. They can be non-zero when there exists parity-violation physics like the axion-like particles which we have not well constrained [15].

Note that $C_{\mathrm{BB},\ell}$ can only be generated by tensor perturbations. Intrinsically, this is consistent with the fact that for a certain Fourier mode, the photon distribution does not maintain axial symmetry. Tensor perturbations represent primordial gravitational waves which can be generated in inflation. Hence, the detection for primordial B-mode can be a very significant evidence of inflation [14] and is one of the most important scientific goals for the ongoing and upcoming experiments.

2.2 Some secondary contributions to CMB

As what I have shown, the CMB anisotropies are contributed mostly by the photons decoupled at recombination. However, there are also secondary effects contributing to the total CMB in the post recombination-era. I will include four secondary effects below which are related to my work in this thesis.

2.2.1 CMB lensing

In the Subsection. 2.1, we calcualte the CMB temperature and polarization based on the line-of-sight approximation, which is not perfectly accurate because the path of CMB photons can be deflected by gravitational potentials according to general relativity. Here I introduce briefly the CMB lensing effect, which refers to the path deflection of CMB photons from the last scattering surface to us. An illustration of CMB lensing is shown in Fig. 9. Most of my work centered around CMB lensing and the systematic bias to CMB lensing reconstruction, here I give a brief introduction of CMB lensing and I will include much more details in the following chapters.

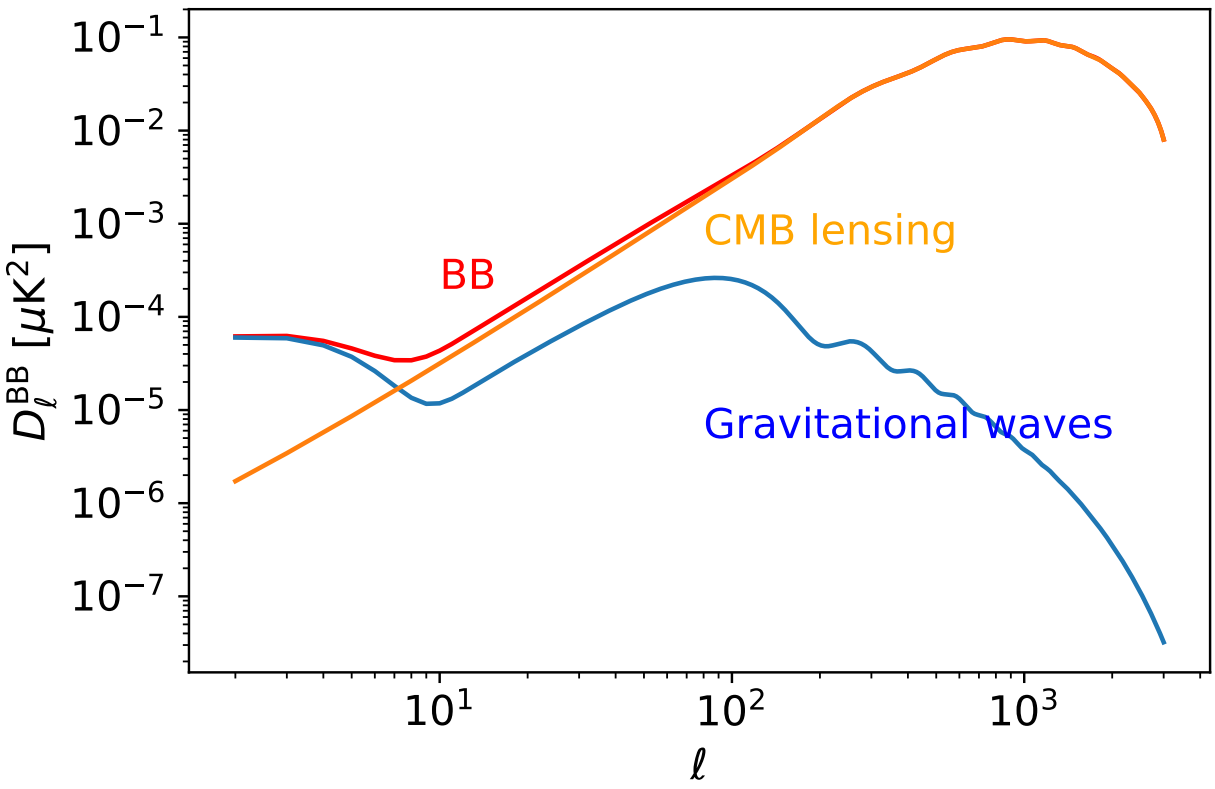

Figure 7: The total CMB BB power spectra and its contributions of CMB lensing and primordial gravitational waves. The power spectra are calculated by `CLASS` [3] numerically.

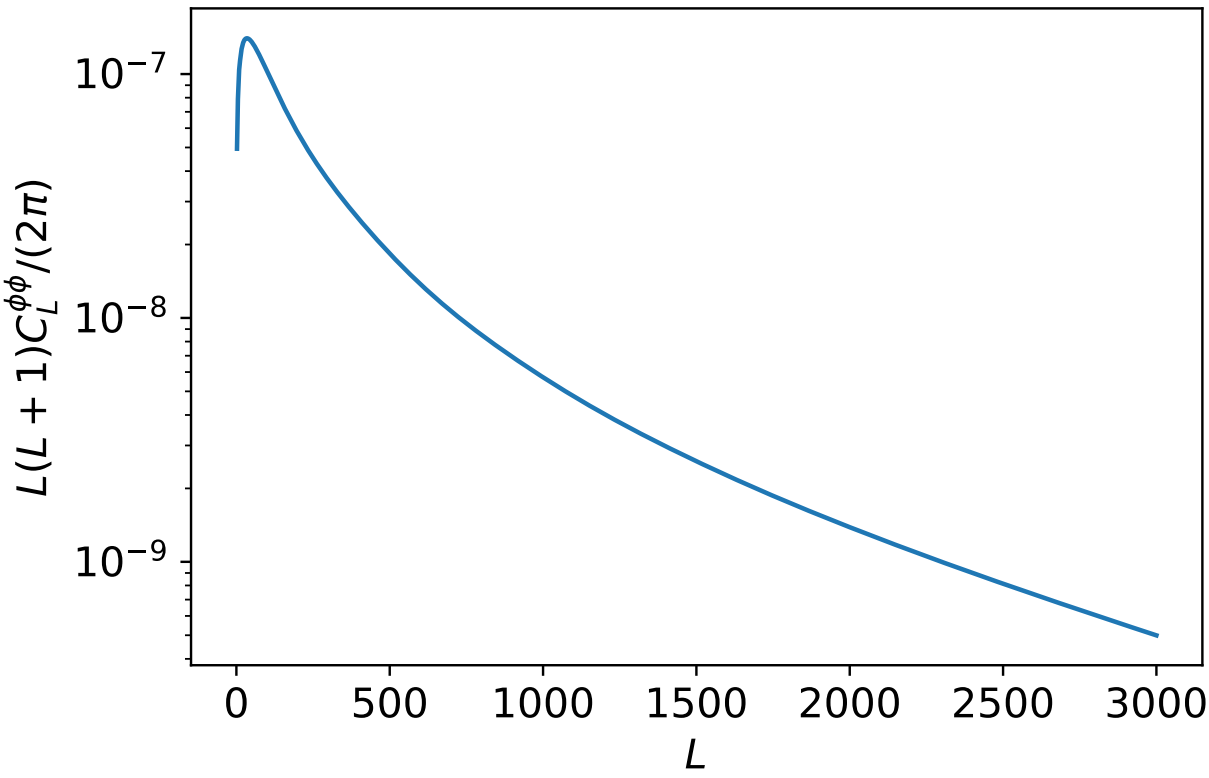

Figure 8: The theory power spectrum of CMB lensing potential for a concordance ΛCDM model calculated by `CLASS` [3] which is in good agreement with the measured one. The peak of the power spectrum is around $\ell \approx 60$. The CMB lensing power spectrum is mostly contributed by the matter fluctuations at $z \sim 2$ and mainly on scales in the linear regime $k \sim 0.05h/\mathrm{Mpc}$.

We can use a deflection field to denote the displacement of the primary CMB maps. Under Born's approximation [b] and the assumption that all CMB photons come from the last scattering surface and that non-linear effect is negligible, the deflection field can be expressed as pure gradiant of the CMB lensing potential [16] which can be written as an integral over the gravitational potentials power spectrum. The power spectrum of CMB lensing potential for a concordance ΛCDM is shown in Fig. 8. The peak is around $\ell \approx 60$. CMB lensing encodes the information of matter density perturbations especially at late-time (peaking at $z \sim 2$ and mainly on scales in the linear regime $k \sim 0.05h/\mathrm{Mpc}$). We can use the CMB lensing power spectrum as a powerful tool of constraining cosmological parameters (see [17, 18] for example) like the linear-theory matter fluctuation amplitude σ_8, the matter density Ω_m, the spatial curvature of the universe Ω_k, the sum of neutrino masses $\sum m_\nu$ and the dark energy equation of state w. CMB lensing is also an significant source of generating B-mode signal, which should be removed using the tool of de-lensing.

CMB lensing distorts CMB power spectra by smoothing out the main baryon acoustic peaks. This can be checked by the expression of the lensed CMB power spectra which has the form of a convolution of unlensed CMB power spectra and CMB lensing potential [16]. The lensing signal is hard to distinguished because it has the same frequency spectrum as the unlensed CMB. However, lensing effect imprints signals by bringing off-diagonal correlations to CMB multipoles, and hence can be reconstructed by quadratic estimators [19, 20]. The current detection of CMB lensing through CMB lensing reconstruction is 40σ [21]. The parameter combination that CMB lensing measures best is $\sigma_8\Omega_\mathrm{m}^{0.25}$ [22]. Combining with the data of baryon acoustic oscillation, we can constrain the individual parameters of σ_8, H_0 and Ω_m. And the neutrino masses $\sum m_\nu$ and the effective number of neutrino species N_eff can be constrained by combining CMB lensing power spectrum (4-point function) and CMB power spectrum (2-point function).

However, there can be some other secondary effects bringing biases to the reconstructed CMB lensing power spectrum which may affect cosmological constraints and the search of primordial B-mode signals. Among these biases to CMB lensing reconstruction, I focus

[b] The Born's approximation corresponds that we calcualte the the deflection angle approximately along the unperturbed path of CMB photon.

on the bias from the kinetic Sunyaev-Zel'dovich (kSZ) effect introduced in Chapter. 2 and anisotropic cosmic birefringence introduced in Chapter. 4.

2.2.2 Cosmic birefringence

Cosmic birefringence refers to the linear polarization rotations that CMB photons may undergo as they travel through the universe from the last scattering surface to us. Cosmic birefringence can be caused by parity-violating physics in the early universe, such as axion-like particles coupling to photons through Chern-Simons interaction [23, 24, 25], more general Lorentz-violating physics beyond the Standard Model [26], and primordial magnetic fields through Faraday rotation which is frequency-dependent [27, 28].

We can use a rotation field to describe the linear rotation of CMB polarization maps induced by cosmic birefringence. A generic rotation field can be separated into an isotropic and anisotropic part. For example, some quintessence models predict both isotropic and anisotropic cosmic birefringence [29]. The isotropic cosmic birefringence violates parity symmetry and induces odd-parity CMB TB and EB power spectra [c]. The anisotropic cosmic birefringence also contributes to CMB polarization power spectra. In Chapter. 3, I will show a method which can calculate rotated CMB power spectra accurately.

Similar to CMB lensing, anisotropic birefringence can induce off-diagnal correlations to CMB multipoles. Thus, like CMB lensing reconstruction algorithm, the anisotropic rotation field can be reconstructed by quadratic estimators [30, 31]. The current best constraint of the scale-invariant anisotropic rotation power spectrum is given by ACTPol [15] and SPTPol [32] corresponding to the 2σ upper bound on the amplitude[d] $A_{\rm CB} \leq 10^{-5}$. The expected constraints of $A_{\rm CB}$ are at the level of 10^{-7} for the next-generation ground-based CMB experiments [33, 34]. In Chapter. 4, I will show a bias from the anisotropic cosmic birefringence to CMB lensing reconstruction.

[c] However, the global polarization angle calibration can produce isotropic rotation and induce such odd-parity CMB power spectra.

[d] Note that A_{CB} defined in this paper is 10^{-4} times of that in [15] and [32].

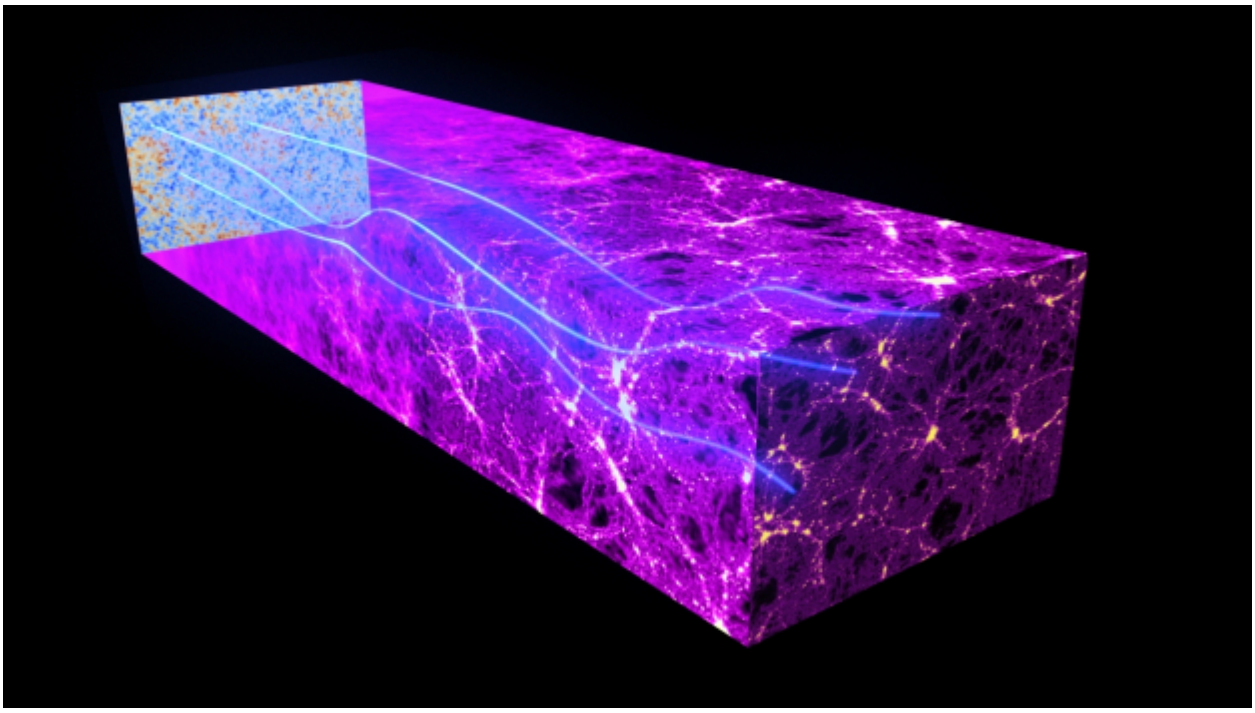

Figure 9: An illustration of the Gravitational lensing of Cosmic Microwave Background (CMB lensing). It demonstrates the CMB photons are deflected by gravitational potentials. The figure is taken from ESA and the Planck Collaboration.

2.2.3 Reionization

We know that most of the gas we observe in the late universe is ionized. However, it was neutral after recombination. Thus, hydrogen must have be reionized at some point of in the history of the universe. This process is called reionization, corresponding to the peak at about $z = 10$ of the visibility function shown in Fig. 3. In the epoch of reionization, hydrogen gets ionized again by the ultraviolet radiation of the first structures, and the free-electron fraction increased again.

We usually use a single cosmological parameter $\tau(\eta_{\rm rei})$ to parametrize reionization, which is the optical depth of reionization. The probability for a photon not to be scattered from reionization until today is given by

$$e^{-\tau(\eta_{\rm rei})}, \tag{60}$$

and according to the definition of the optical depth it can be expressed by an integral along the path as

$$\tau(\eta) \equiv \int_{\eta}^{\eta_0} d\chi n_e \sigma_{\rm T} a, \tag{61}$$

where n_e is the free-electron number density in the CMB rest frame. And naturally, its time derivative is the photon-electron interaction rate as

$$\tau' = -n_e \sigma_{\rm T} a. \tag{62}$$

The visibility function which has been introduced in Subsection. 2.1, can be determined by the optical depth at η by

$$g(\eta) \equiv -\tau' e^{-\tau}. \tag{63}$$

Here I show a simplified calculation of the fraction of photons scattered from reionization to now. We assume a instantaneous reionization in matter-domination at $\eta_{\rm rei}$, i.e. the free-electron fraction $X_{\rm e} = 1$ for $z < z_{\rm rei}$, so we have

$$\tau\left(\eta_{\rm rei}\right) = \int_{\eta_{\rm rei}}^{\eta_0} d\eta n_e \sigma_{\rm T} a = \sigma_{\rm T} \int_0^{z_{\rm rei}} \frac{dz}{(1+z)^2 H} n_e. \tag{64}$$

Of course, the calculation above is far from the reality. On the one hand, the free-electron fraction did not go up in a sudden. The best current measurements using CMB show that $z_{\rm rei} < 10$ [2], and the observations of the most distant quasars indicate that reionization

happened at $z_{\rm rei} > 6$ [35]. On the other hand, reionization is inhomogeneous (patchy). The details of reionization as the last phase transition is still uncertain.

Then we take a look at how reionization affects CMB. After CMB photons are scattered by reionization area, the temperature map can be given by

$$T(1+\Theta)e^{-\tau_{\rm rei}} + T\left(1-e^{-\tau_{\rm rei}}\right) = T\left(1+\Theta e^{-\tau_{\rm rei}}\right), \tag{65}$$

where T is the background temperature, and Θ is the perturbation. This distortion only affects multipoles at small scales within the horizon at the time of reionization ($\ell > \eta_0/\eta_{rei}$). Reionization suppresses CMB temperature power spectra overall on scale $\ell > 150$, largely degenerating with the change in $A_{\rm s}$ and $n_{\rm s}$. Reionization also produces polarization, which is only significant on very large angular scales. The degeneracy between the optical depth due to reionization and the amplitude of scalar perturbations can be broken by the E-mode polarizations at the lowest multipoles. In addition, it is shown by current models that the B-mode generated by reionization is significantly lower than that from gravitational lensing.

2.2.4 The Kinetic Sunyaev-Zel'dovich (kSZ) effect

The kSZ effect is due to the scattering of CMB photons by the bulk motion of free electrons. To understand the kSZ effect, I first show the full SZ effect, i.e. the fluctuations of CMB on small angular scales caused by the Compton scattering of CMB photons by free electrons in the intergalactic medium. The distribution function of scattered CMB photons can be given by

$$\begin{aligned} \delta f &= \int d\chi g(\chi) S \\ &= \int d\chi n_{\rm e}\sigma_{\rm T} a e^{-\tau} S, \end{aligned} \tag{66}$$

where I have applied the visibility function expressed by Eq. (63) and Eq. (62), and S is the source function. It is demonstrated in [36] that one of the leading-order terms of S is proportional to $\mathbf{v}_{\rm e}\cdot\hat{\mathbf{n}}$, where $\mathbf{v}_{\rm e}$ is the bulk velocity of ionized electrons, and $\hat{\mathbf{n}}$ is the direction of line-of-sight. The contribution of this term corresponds to the kSZ effect [e]. The

[e] By contrast, the tSZ effect is an order of magnitude larger than kSZ.

kSZ contribution to CMB temperature fluctuations should be given by

$$\Theta_{\rm kSZ} = \int d\chi n_{\rm e} \sigma_{\rm T} a e^{-\tau} \mathbf{v}_{\rm e} \cdot \hat{\mathbf{n}}, \tag{67}$$

where we can see kSZ depends on the peculiar bulk velocity of ionized photons. kSZ is very difficult to detect firstly because it contributes CMB power anisotropies at very small scales and much smaller than the signal of the thermal Sunyaev-Zel'dovich effect (tSZ effect). It remains black-body spectrum and hence cannot be separated by multi-frequency technique like tSZ. In addition, it cancels out mostly because the bulk velocity of free electrons along the line-of-sight can have either positive or negative sign, which requires very careful kSZ estimators. The SPT collaboration has given an upper limit on kSZ power spectrum at $l = 3000$ of $D_{\ell=3000,\rm kSZ} < 2.8\mu K$ [37].

Then we take a look at the contributions to kSZ from two stages: reionizaiton period and late-time period. The contribution from reionization is above $z_{\rm ov}$, where $z_{\rm ov}$ is the redshift of the end of reionization. The ionization was patchy and incomplete in the epoch of reionization, so this contribution also depends on the time and spatial variations of reionization, which are not yet well constrained. The late-time contribution is below $z_{\rm ov}$, when reionization is complete and the universe is fully ionized. Compared with reionizaiton contribution, the late-time kSZ contribution contains more information of the information of the late-time universe like the large-scale structure formation and late-time matter perturbations. Hence, it correlates with CMB lensing significantly because the latter is contributed by the matter perturbations around $z \approx 2$ the most. As a contrast, because reionization takes place at a relatively hight redshift and when the free electron field is mostly due fluctuations in the ionization fraction, we assume reionization kSZ only weekly correlates with CMB lensing. In Chapter. 2, we will see that the late-time kSZ biases CMB lensing reconstruction due to its correlation with CMB lensing, and the bias from the reionization kSZ is much smaller than that from the late-time kSZ. kSZ signal does not affect CMB polarization significantly to the lowest order.

2.0 The Bias to Cosmic Microwave Background Lensing Reconstruction from the Kinematic Sunyaev-Zel'dovich Effect at Reionization

The content of this chapter is based on the manuscript which has been published on Physical Review D journal [38]. The power spectrum of reconstructed cosmic microwave background (CMB) lensing maps is a powerful tool for constraints on cosmological parameters like the sum of the neutrino masses and the dark energy equation of state. One possible complication is the kinematic Sunyaev-Zel'dovich (kSZ) effect, due to the scattering of CMB photons by moving electrons, which can bias the reconstruction of the CMB lensing power spectrum through both kSZ-lensing correlations and the non-Gaussianity of the kSZ temperature anisotropies. We investigate for the first time the bias to CMB lensing reconstruction from temperature anisotropies due to the reionization-induced kSZ signal and show that it is negligible for both ongoing and upcoming experiments based on current numerical simulations of reionization. We also revisit the bias induced by the late-time kSZ field, using more recent kSZ simulations. We find that it is potentially twice as large as found in earlier studies, reaching values as large as several percent of the CMB lensing power spectrum signal, indicating that this bias will have to be mitigated in upcoming data analyses.

1 Introduction

Cosmic microwave background (CMB) photons are deflected by gravitational potentials while they travel from the last scattering surface to us. This effect, known as CMB lensing [39, 40], remaps the CMB intensity and polarization fields. Compared with galaxy lensing [41], CMB lensing can probe matter inhomogeneities at relatively higher redshifts. In addition, CMB lensing also helps constrain fundamental cosmological parameters [42], including the sum of the neutrino masses [43, 44, 42] and the dark energy equation of state [43].

CMB lensing can be described by the lensing potential, which is a line-of-light projection of the three-dimensional gravitational potential weighted by a geometric lensing kernel.

The lensing potential can be reconstructed using a minimum-variance quadratic estimator [45, 46] using both CMB temperature and polarization maps. Ongoing and upcoming experiments, including Advanced ACT [47], SPT-3G [48], and Simons Observatory (SO) [49], have sensitivities for which temperature maps provide most of the statistical weight for lensing reconstruction; proposed future experiments such as CMB-S4 [50] and CMB-HD [51] will have high enough sensitivity so that polarization becomes the dominant channel for lensing reconstruction.

Besides lensing, CMB temperature maps also contain signals from several secondary anisotropies including the thermal and kinematic Sunyaev-Zel'dovich effects (tSZ and kSZ), the integrated Sachs-Wolfe effect, and the Rees-Sciama effect, and foregrounds from thermal dust, radio synchrotron emission, and the cosmic infrared background (CIB). Most of these contaminants can be removed or suppressed by multifrequency component separation methods [52, 53, 54, 55]. Since the kSZ effect preserves the blackbody spectrum of the CMB [a], it cannot be removed by multifrequency component separation methods (internal linear combination, or ILC) (e.g., as possible for the tSZ or CIB fields [58])[b]. Any significant bias to CMB lensing reconstruction from the kSZ effect must be mitigated using geometric techniques such as shear-only reconstruction [61] or bias-hardened estimators [62, 63, 64].

The kSZ signal has two physically distinct pieces: the late-time contribution (below the redshift at which the universe has become fully reionized) and the reionization contribution (from the epoch before reionization is complete). The bias to CMB lensing power spectrum measurements from temperature anisotropies due to the late-time kSZ signal was investigated in [7], showing that the large-scale ($L < 500$) fractional bias can reach 0.5%, 2% and 3% for Planck, Stage-III experiments (similar to SO) and CMB-S4, respectively, when using $\ell_{\rm max} = 4000$, and about half of that for $\ell_{\rm max} = 3000$, where $\ell_{\rm max}$ is the maximum temperature multipole used in the lensing reconstruction and L is the multipole of the reconstructed lensing map. In this work, we investigate the bias due to the reionization kSZ signal for the first time, and also revisit the late-time kSZ bias. Since the kSZ effect produces negligible

[a] There are higher-order relativistic SZ terms which have the same velocity dependence as the kSZ effect [56, 57, 36], and they do not preserve blackbody spectrum.

[b] The standard ILC can induce significant bias, which can be mitigated by geometric methods such as profile hardening, and by partial joint deprojection method [59]. The best-performed combination of multifrequency and geometric methods is introduced in [60].

polarization fluctuations, we consider only temperature anisotropies. The redshift of reionization and its detailed kSZ signature are not constrained to high precision by current data; our conclusions are based on current numerical simulations of reionization from the WebSky[c] extragalactic CMB simulations [5]. Our conclusions will have some quantitative dependence on the exact reionization model assumed, although they are unlikely to differ qualitatively. In addition, a related but different analysis is performed in [65], which computes the bias to CMB lensing reconstruction arising from the fact that foreground fields (including the reionization kSZ signal) are lensed by the some of the same structures as the CMB. The bias arising from the intrinsic non-Gaussianity of the kSZ field is not considered in [65], and forms the focus of our investigation.

In this paper, we assume a ΛCDM fiducial cosmology with the Planck 2015 parameters given in the third column of Table 4 of [66].

This paper is organized as follows. We revisit the CMB lensing reconstruction using CMB temperature anisotropies in Section 2. In Section 3, we introduce the kSZ effect and explain how to estimate the bias induced by the kSZ effect on the reconstructed CMB lensing power spectrum. Analytical details of the CMB temperature trispectrum and the kSZ effect can be found in Section 4. We describe the details of our simulations and the numerical results in Section 5, and conclude in Section 6.

2 CMB lensing reconstruction from temperature anisotropies

A gravitationally lensed CMB temperature map $\tilde{T}(\hat{\mathbf{n}})$ can be expressed as

$$\tilde{T}(\hat{\mathbf{n}}) = T(\hat{\mathbf{n}} + \mathbf{d}(\hat{\mathbf{n}})), \tag{68}$$

where $\hat{\mathbf{n}}$ is the direction on the full sky, $T(\hat{\mathbf{n}})$ is the unlensed CMB temperature map, and $\mathbf{d}(\hat{\mathbf{n}})$ is the lensing deflection field. At lowest order in the deflection field, $\mathbf{d}(\hat{\mathbf{n}})$ is a pure gradient [39] given by

$$\mathbf{d}(\hat{\mathbf{n}}) = \nabla\phi(\hat{\mathbf{n}}), \tag{69}$$

[c] https://lambda.gsfc.nasa.gov/simulation/tb_mocks_data.cfm

where ∇ represents the angular derivative on the sphere defined by $\hat{\mathbf{n}}$, and $\phi(\hat{\mathbf{n}})$ is the lensing potential. The CMB lensing convergence is defined as

$$\kappa(\hat{\mathbf{n}}) = -\frac{1}{2}\nabla^2\phi(\hat{\mathbf{n}}), \tag{70}$$

which can be reconstructed by a minimum variance quadratic estimator. Under the flat-sky approximation in Fourier space, the temperature quadratic estimator is given by [67]

$$\hat{\kappa}(\mathbf{L}) = \frac{1}{2}L^2 A(\mathbf{L}) \int_{\boldsymbol{\ell}} g(\boldsymbol{\ell}, \mathbf{L}) T^{\rm tot}(\boldsymbol{\ell}) T^{\rm tot}(\mathbf{L} - \boldsymbol{\ell}), \tag{71}$$

where

$$g(\boldsymbol{\ell}, \mathbf{L}) = \frac{C_\ell^{TT}\boldsymbol{\ell}\cdot\mathbf{L} + C_{|\mathbf{L}-\boldsymbol{\ell}|}^{TT}\mathbf{L}\cdot(\mathbf{L}-\boldsymbol{\ell})}{2C_\ell^{tot}C_{|\mathbf{L}-\boldsymbol{\ell}|}^{tot}}, \tag{72}$$

$\hat{\kappa}(\mathbf{L})$ represents the estimator for $\kappa(\mathbf{L})$, and $T^{\rm tot}$ is the observed total temperature anisotropy field containing the lensed primordial fluctuations $\tilde{T}$, the blackbody secondary fluctuations, and detector noise (which we assume is uncorrelated with the other components). The normalization $A(\mathbf{L})$ and weight $g(\boldsymbol{\ell}, \mathbf{L})$ both depend on the fiducial lensed CMB power spectrum and the experiment's beam and noise properties. The C_ℓ^{tot} in the denominator is the total observed CMB temperature power spectrum. Note here we denote

$$\int_{\boldsymbol{\ell}} \equiv \int \frac{d^2\boldsymbol{\ell}}{(2\pi)^2}. \tag{73}$$

The expectation value of the power spectrum of $\hat{\kappa}$ is

$$\langle C_L^{\hat{\kappa}\hat{\kappa}}\rangle = \langle \hat{\kappa}(\mathbf{L})\hat{\kappa}^*(\mathbf{L})\rangle = \langle \hat{\kappa}(\mathbf{L})\hat{\kappa}(-\mathbf{L})\rangle, \tag{74}$$

where $\langle\ \rangle$ represents $\langle\langle\ \rangle_{\rm CMB}\rangle_{\rm LSS}$ which denotes an ensemble average over different primordial CMB Gaussian realizations and large-scale structure realizations [68]. Thus, all the maps inside the brackets are random variables. In the real simulation introduced in Section 5, the $C_L^{\hat{\kappa}\hat{\kappa}}$ are bandpowers binned on the two-dimensional reconstructed κ Fourier map.

To get an unbiased estimator of $C_L^{\kappa\kappa}$, several reconstruction biases are subtracted from $C_L^{\hat{\kappa}\hat{\kappa}}$ as

$$\begin{aligned}\hat{C}_L^{\kappa\kappa} =& \langle C_L^{\hat{\kappa}\hat{\kappa}}\rangle - (\Delta C_L^{\kappa\kappa})_{\rm Gauss} - (\Delta C_L^{\kappa\kappa})_{\rm N1} \\ & -(\Delta C_L^{\kappa\kappa})_{\rm MC} - (\Delta C_L^{\kappa\kappa})_{\rm FG},\end{aligned} \tag{75}$$

where $\hat{C}_L^{\kappa\kappa}$ is the estimator of $C_L^{\kappa\kappa}$, $(\Delta C_L^{\kappa\kappa})_{\rm Gauss}$ is the Gaussian bias induced by the Gaussian disconnected component of the trispectrum in Eq. (83),[d] $(\Delta C_L^{\kappa\kappa})_{\rm N1}$ arises from the connected terms of the CMB trispectrum containing an integral over $C_L^{\kappa\kappa}$ [68], $(\Delta C_L^{\kappa\kappa})_{\rm MC}$ is a "Monte Carlo" (MC) bias that encapsulates biases which have not been accounted for otherwise, such as higher-order corrections[e], and $(\Delta C_L^{\kappa\kappa})_{\rm FG}$ is the foreground bias. In this paper, $(\Delta C_L^{\kappa\kappa})_{\rm FG}$ is limited to the bias from the kSZ effect $(\Delta C_L^{\kappa\kappa})_{\rm kSZ}$.

3 CMB lensing power spectrum bias from the kSZ effect

The kSZ effect is induced by the bulk motion of the ionized gas when CMB photons travel through the universe [73]. The temperature fluctuations induced by the kSZ effect in a direction $\hat{\mathbf{n}}$ are given by (in units with $c = 1$)

$$\frac{\Delta T^{\rm kSZ}(\hat{\mathbf{n}})}{T_{\rm CMB}} = -\sigma_T \int \frac{d\eta}{1+z} e^{-\tau} n_e(\hat{\mathbf{n}}, \eta) \mathbf{v}_e \cdot \hat{\mathbf{n}}, \tag{76}$$

where σ_T is the Thomson scattering cross section, n_e is the local number density of free electrons, and $\mathbf{v}_e \cdot \hat{\mathbf{n}}$ is the peculiar velocity of the electrons projected along the line of sight, defined such that positive (negative) velocities point away from (toward) our vantage point. The distribution of the kSZ temperature fluctuations is non-Gaussian due to gravitational and baryonic-feedback-induced non-linearities in the gas distribution.

The kSZ effect is dominated by epochs with large electron density fluctuations. The kSZ signal has two main contributions [74]: the reionization contribution and the late-time contribution. The reionization kSZ arises from the local patchy and incomplete ionization during the epoch of reionization [75, 76, 77]. The late-time kSZ, also known as the post-reionization kSZ [78], arises after the epoch of reionization, when the universe is fully ionized.

The temperature fluctuations induced by the kSZ effect in a direction $\hat{\mathbf{n}}$ are given by (in units with $c = 1$)

$$\frac{\Delta T^{\rm kSZ}(\hat{\mathbf{n}})}{T_{\rm CMB}} = -\int d\eta g(\eta) \mathbf{p}_e \cdot \hat{\mathbf{n}} \ , \tag{77}$$

[d] In real experiments, we calculate the realization-dependent Gaussian bias $(\Delta C_L^{\kappa\kappa})_{\rm RDN0}$ which depends on the CMB realizations [62, 69].

[e] In this paper, the lensing potential we consider is Gaussian, so no $(\Delta C_L^{\kappa\kappa})_{\rm N3/2}$ appears [70, 71, 72].

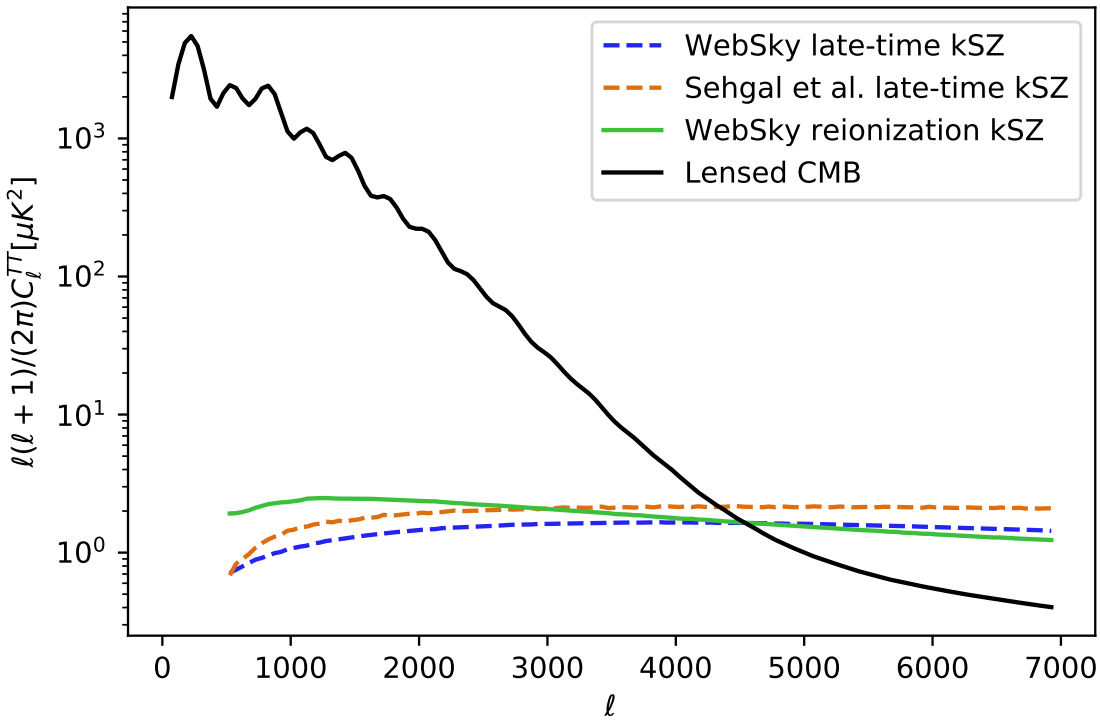

Figure 10: The CMB power spectrum from lensed CMB, reionization kSZ, and late-time kSZ. The kSZ spectra are from the WebSky simulation [5] and the Sehgal et al. simulation [6].

where $\eta(z)$ is the comoving distance to redshift z, $g(\eta)$ is the visibility function, and $\mathbf{p}_e$ is the peculiar electron momentum.

The visibility function $g(\eta)$ represents the Poissonian probability that a photon is last scattered at a time η which can be given by $g(\eta) = (d\tau/d\eta)e^{-\tau} = \sigma_T n_{e,0} a e^{-\tau}$. $n_{e,0}$ is mean physical number density of free electrons, a is the scale factor and τ is the optical depth. We define $\mathbf{p}_e = (1+\delta_e)\mathbf{v}_e$, where δ_e is the free electron density contrast, and $\mathbf{v}_e$ is the electron velocity. The free electron density contrast can be expressed as $\delta_e = (1+\delta)(1+\delta_x)$, where δ is the gas density contrast and δ_x is the ionization contrast. So we have

$$\frac{\Delta T^{\rm kSZ}(\hat{\mathbf{n}})}{T_{\rm CMB}} = -\sigma_T \int \frac{d\eta}{1+z} e^{-\tau}(1+\delta+\delta_x+\delta\delta_x)\mathbf{v}_e \cdot \hat{\mathbf{n}}, \tag{78}$$

where the first contribution ($\propto \mathbf{v}_e$) is referred to as the "Doppler" term, the second contribution ($\propto \delta\mathbf{v}_e$) is the "Ostriker-Vishniac" term, and the third contribution ($\propto \delta_x\mathbf{v}_e$) is the "patchy" term.

The ionization is inhomogeneous during the epoch of reionization, i.e., $\delta_x \neq 0$. The modeling of reionization kSZ used in this work is described in [79, 80].

Fig. 10 shows that on the smallest scales $\ell \gtrsim 4000$, the kSZ effect starts to dominate the CMB temperature power spectrum. The reionization and late-time kSZ power spectrum contributions are comparable in magnitude. The reionization kSZ is expected to be only weakly correlated with CMB lensing, but the correlation of the late-time kSZ and CMB lensing is much larger, for most of the lensing fluctuations are generated at relatively low redshift. However, the reionization kSZ signal is of potential concern for lensing reconstruction bias because of its intrinsically non-Gaussian pattern on the sky.

We assume secondary anisotropies have been removed by multifrequency component separation methods (or with geometric methods), and except the kSZ and lensing signals. The integrated Sachs-Wolfe effect is also blackbody, but is negligible except on the largest angular scales. Then the total CMB temperature map under the flat-sky approximation can be written as

$$T^{\rm tot}(\mathbf{x}) = \tilde{T}(\mathbf{x}) + T^{\rm kSZ}(\mathbf{x}), \tag{79}$$

where $\tilde{T}(\mathbf{x})$ is the lensed CMB field and $T^{\rm kSZ}(\mathbf{x})$ is the kSZ signal.

The total temperature map $T^{\rm tot}(\mathbf{x})$ contains $T^{\rm kSZ}(\mathbf{x})$ which is non-Gaussian and may correlate with lensing. When we perform CMB lensing reconstruction with temperature anisotropies using Eq. (71), we include the Fourier modes $T^{\rm kSZ}(\boldsymbol{\ell})$ in the estimator. The non-Gaussianity of kSZ and any kSZ-lensing correlation bias the estimation of $C_L^{\kappa\kappa}$ since extra connected terms are brought to the CMB temperature trispectrum as shown in Section. 4.

Estimating this bias is straightforward. We use one set of simulated kSZ realizations, described in the next section, to represent $T^{\rm kSZ}(\mathbf{x})$ in Eq. (79), and generate another set of Gaussian kSZ realizations $T^{\rm kSZ,g}(\mathbf{x})$ with the same average power spectrum. We also have a set of lensed CMB realizations $\tilde{T}(\mathbf{x})$. We define

$$T^{\rm tot,g}(\mathbf{x}) = \tilde{T}(\mathbf{x}) + T^{\rm kSZ,g}(\mathbf{x}) \tag{80}$$

which is similar to Eq. (79) except for the Gaussian kSZ term. We apply the quadratic estimator in Eq. (71) to $T^{\rm tot}(\boldsymbol{\ell})$ and $T^{\rm tot,g}(\boldsymbol{\ell})$ to obtain two sets of reconstructed lensing convergence maps with power spectra of $C^{\hat{\kappa}\hat{\kappa}}_{L,{\rm tot}}$ and $C^{\hat{\kappa}\hat{\kappa}}_{L,{\rm tot,g}}$. Since $T^{\rm tot}$ and $T^{\rm tot,g}$ have the same power spectrum and share the same lensed CMB realizations, they have the same reconstruction biases shown in Eq.(75) on average. Because $T^{\rm tot,g}(\mathbf{x})$ is Gaussian and not correlated with $\tilde{T}(\mathbf{x})$, it does not induce the $(\Delta C_L^{\kappa\kappa})_{\rm FG}$ in Eq. (75). Thus, the bias to CMB lensing reconstruction from temperature maps due to the kSZ effect can be estimated by

$$(\Delta C_L^{\kappa\kappa})_{\rm kSZ} = \langle C^{\hat{\kappa}\hat{\kappa}}_{L,{\rm tot}} \rangle - \langle C^{\hat{\kappa}\hat{\kappa}}_{L,{\rm tot,g}} \rangle, \tag{81}$$

where the brackets are the average over the two sets of reconstructed lensing convergence maps.

This method to estimate $(\Delta C_L^{\kappa\kappa})_{\rm kSZ}$ in Eq. (81) can be applied to both the reionization kSZ and the late-time kSZ signals [7]. A similar approach has also been applied in [71] to estimate the non-Gaussian lensing bias in CMB lensing reconstruction.

Since the reionization kSZ signal is only weakly correlated with the CMB lensing field[f], the kSZ trispectrum induced by its non-Gaussianity is expected to be the dominant contribution to the CMB lensing reconstuction bias. Thus, we can apply the CMB lensing

[f] The reionization kSZ simulations used in this paper are actually uncorrelated with the CMB lensing field.

reconstruction algorithm to the reionization kSZ map directly without adding the lensed CMB map and compute the bias by

$$(\Delta C_L^{\kappa\kappa})_{\rm kSZ} = \langle C_{L,\rm kSZ}^{\hat{\kappa}\hat{\kappa}} \rangle - \langle C_{L,\rm kSZ,g}^{\hat{\kappa}\hat{\kappa}} \rangle. \tag{82}$$

This bias estimate neglects terms arising from the correlation between the kSZ and CMB lensing fields. For the full kSZ signal including correlation of lensing with late-time kSZ, we need to apply the CMB lensing reconstruction algorithm to the sum of the lensed CMB map and the late-time kSZ map, and estimate the bias using Eq. (81).

4 kSZ bias to CMB temparature trispectrum

The power spectrum of $\hat{\kappa}$ can be written as

$$\begin{aligned}\langle \hat{\kappa}(\mathbf{L})\hat{\kappa}(\mathbf{L}')\rangle = \frac{1}{4}L^2 L'^2 A(\mathbf{L})A(\mathbf{L}') \\ \int_{\boldsymbol{\ell}_1,\boldsymbol{\ell}_2,\boldsymbol{\ell}_3,\boldsymbol{\ell}_4} g(\boldsymbol{\ell}_1, \boldsymbol{\ell}_1+\boldsymbol{\ell}_2) g(\boldsymbol{\ell}_3, \boldsymbol{\ell}_3+\boldsymbol{\ell}_4) \\ \langle T^{\rm tot}(\boldsymbol{\ell}_1) T^{\rm tot}(\boldsymbol{\ell}_2) T^{\rm tot}(\boldsymbol{\ell}_3) T^{\rm tot}(\boldsymbol{\ell}_4)\rangle \\ \delta(\mathbf{L}-\boldsymbol{\ell}_1-\boldsymbol{\ell}_2)\delta(\mathbf{L}-\boldsymbol{\ell}_3-\boldsymbol{\ell}_4)\end{aligned} \tag{83}$$

To understand the bias to reconstructed CMB lensing power spectrum from the late-time kSZ and the reionization kSZ, we check the trispectrum

$$\langle T^{\rm tot}(\boldsymbol{\ell}_1) T^{\rm tot}(\boldsymbol{\ell}_2) T^{\rm tot}(\boldsymbol{\ell}_3) T^{\rm tot}(\boldsymbol{\ell}_4)\rangle, \tag{84}$$

where we decompose the $T^{\rm tot}(\boldsymbol{\ell})$ as

$$T^{\rm tot}(\boldsymbol{\ell}) = \tilde{T}(\boldsymbol{\ell}) + T^{\rm kSZ}(\boldsymbol{\ell}). \tag{85}$$

Again, note that we do not include $T^{\rm det}$, since it is Gaussian with zero expectation and uncorrelated with any other components.

The lensed CMB temperature Fourier modes can be expressed as

$$\tilde{T}(\boldsymbol{\ell}) = T(\boldsymbol{\ell}) + \delta T(\boldsymbol{\ell}) + \delta^2 T(\boldsymbol{\ell}) + \mathcal{O}(\phi^3(\boldsymbol{\ell})) \tag{86}$$

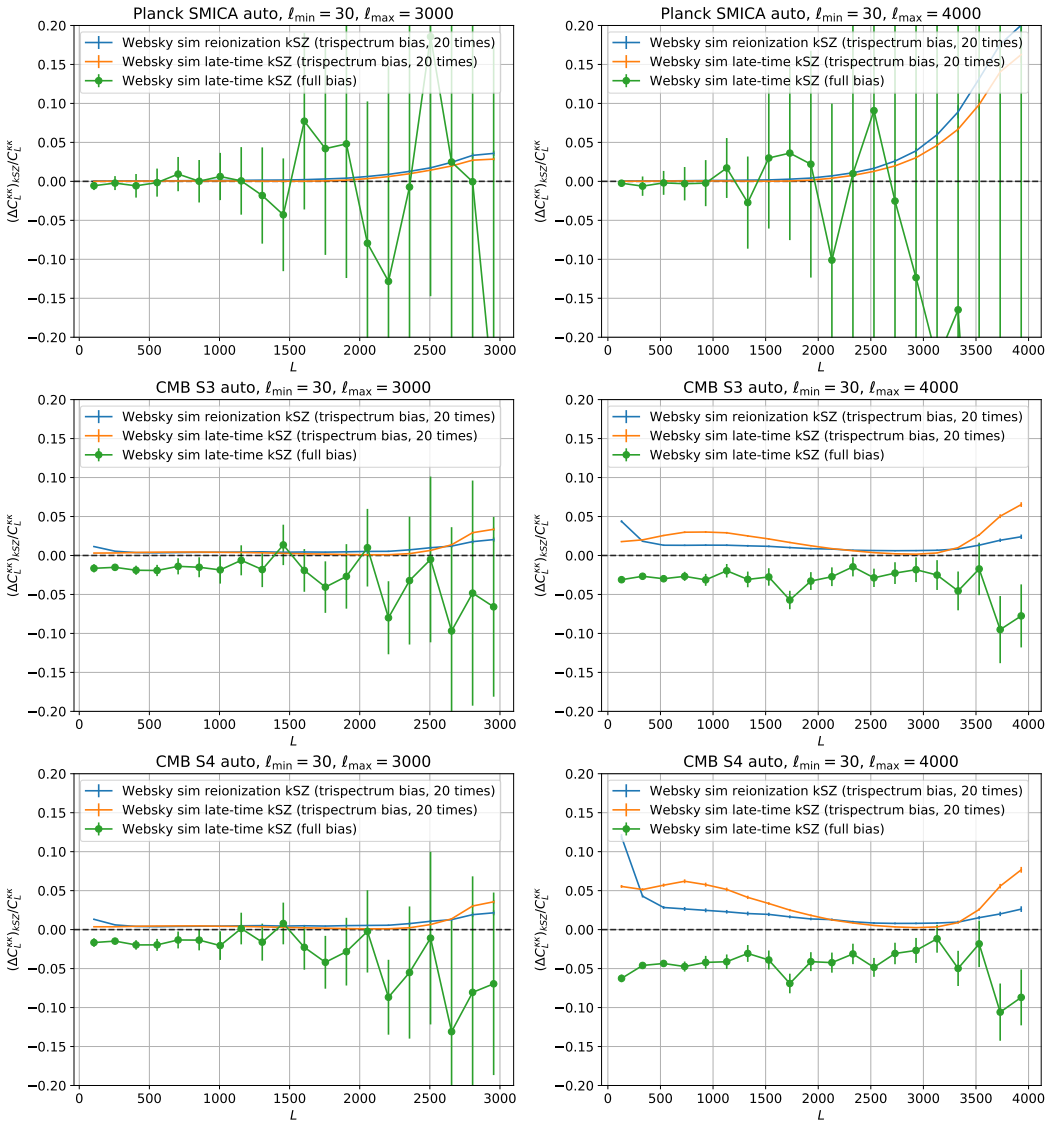

Figure 11: The fractional bias to the reconstructed CMB lensing convergence power spectrum induced by the reionization kSZ trispectrum, the late-time kSZ trispectrum, and the full late-time kSZ bias, computed using the WebSky simulation. The curves showing the reionization kSZ trispectrum bias, the late-time kSZ trispectrum bias and the corresponding error bars are multiplied by a factor of 20.

with $\mathcal{O}(\phi)$ correction

$$\delta T(\boldsymbol{\ell}) = -\int_{\boldsymbol{\ell}'} \boldsymbol{\ell}' \cdot (\boldsymbol{\ell} - \boldsymbol{\ell}') T(\boldsymbol{\ell}') \phi(\boldsymbol{\ell} - \boldsymbol{\ell}'), \tag{87}$$

and $\mathcal{O}(\phi^2)$ correction

$$\begin{aligned}\delta^2 T(\boldsymbol{\ell}) = \frac{1}{2}\int_{\boldsymbol{\ell}'}\int_{\boldsymbol{\ell}''} &\left[\boldsymbol{\ell}' \cdot \boldsymbol{\ell}''\right]\left[\boldsymbol{\ell}' \cdot (\boldsymbol{\ell} - \boldsymbol{\ell}' - \boldsymbol{\ell}'')\right] T\left(\boldsymbol{\ell}'\right) \\ &\phi\left(\boldsymbol{\ell}''\right)\phi\left(\boldsymbol{\ell} - \boldsymbol{\ell}' - \boldsymbol{\ell}''\right),\end{aligned} \tag{88}$$

where ϕ is the CMB lensing potential.

In our calculation, we only include $\delta T(\boldsymbol{\ell})$. We assume that the unlensed CMB is a Gaussian field. ϕ and $T^{\rm kSZ}$ are both not Gaussian. We ignore the ISW effect and the Rees-Sciama effect, so we do not consider the correlation of unlensed CMB with lensing $C^{T\phi}$.

We plug Eq. (80), Eq. (87) and Eq. (88) into Eq. (84), and check all the possible contractions. Any terms including odd powers of $T^{\rm kSZ}$ vanish on average according to its symmetry [7]. The fields labeled with primes correspond to the second reconstruction field $\hat{\kappa}(\mathbf{L}')$ in Eq. (83), and the fields without primes correspond to the first one.

There are several types of contraction up to the order of ϕ^2 with even power of $T^{\rm kSZ}$:

type a:

$$\begin{aligned}&\langle T^{\rm kSZ}_{\boldsymbol{\ell}_1} T^{\rm kSZ}_{\boldsymbol{\ell}_2} T'_{\boldsymbol{\ell}_3} \phi'_{\boldsymbol{\ell}_3} T'_{\boldsymbol{\ell}_4}\rangle \\ =&\langle \underbrace{T^{\rm kSZ}_{\boldsymbol{\ell}_1}}\, \underbrace{T^{\rm kSZ}_{\boldsymbol{\ell}_2}}\, \overbrace{T'_{\boldsymbol{\ell}_3}}\, \underbrace{\phi'_{\boldsymbol{\ell}_3}}\, \overbrace{T'_{\boldsymbol{\ell}_4}}\rangle \\ =&\langle T'_{\boldsymbol{\ell}_3} T'_{\boldsymbol{\ell}_4}\rangle \langle T^{\rm kSZ}_{\boldsymbol{\ell}_1} T^{\rm kSZ}_{\boldsymbol{\ell}_2} \phi'_{\boldsymbol{\ell}_3}\rangle \to \text{(a1)}\end{aligned} \tag{89}$$

type b:

$$\begin{aligned}&\langle T^{\rm kSZ}_{\boldsymbol{\ell}_1} T^{\rm kSZ}_{\boldsymbol{\ell}_2} T'_{\boldsymbol{\ell}_3} \phi'_{\boldsymbol{\ell}_3} T'_{\boldsymbol{\ell}_4} \phi'_{\boldsymbol{\ell}_4}\rangle \\ =&\langle \underbrace{T^{\rm kSZ}_{\boldsymbol{\ell}_1}}\, \underbrace{T^{\rm kSZ}_{\boldsymbol{\ell}_2}}\, \overbrace{T'_{\boldsymbol{\ell}_3}}\, \underbrace{\phi'_{\boldsymbol{\ell}_3}}\, \overbrace{T'_{\boldsymbol{\ell}_4}}\, \underbrace{\phi'_{\boldsymbol{\ell}_4}}\rangle \\ =&\langle \underbrace{T^{\rm kSZ}_{\boldsymbol{\ell}_1}}\, T^{\rm kSZ}_{\boldsymbol{\ell}_2}\, \overbrace{T'_{\boldsymbol{\ell}_3}}\, \underbrace{\phi'_{\boldsymbol{\ell}_3}}\, \overbrace{T'_{\boldsymbol{\ell}_4}}\, \underbrace{\phi'_{\boldsymbol{\ell}_4}}\rangle \to \text{(b1)} \\ +&\langle \underbrace{T^{\rm kSZ}_{\boldsymbol{\ell}_1}}\, \underbrace{T^{\rm kSZ}_{\boldsymbol{\ell}_2}}\, \overbrace{T'_{\boldsymbol{\ell}_3}}\, \underbrace{\phi'_{\boldsymbol{\ell}_3}}\, \overbrace{T'_{\boldsymbol{\ell}_4}}\, \underbrace{\phi'_{\boldsymbol{\ell}_4}}\rangle \to \text{(b2)} \\ +&\langle \underbrace{T^{\rm kSZ}_{\boldsymbol{\ell}_1}}\, \underbrace{T^{\rm kSZ}_{\boldsymbol{\ell}_2}}\, \overbrace{T'_{\boldsymbol{\ell}_3}}\, \underbrace{\phi'_{\boldsymbol{\ell}_3}}\, \overbrace{T'_{\boldsymbol{\ell}_4}}\, \underbrace{\phi'_{\boldsymbol{\ell}_4}}\rangle \to \text{(b3)} \\ +&\langle T'_{\boldsymbol{\ell}_3} T'_{\boldsymbol{\ell}_4}\rangle \langle T^{\rm kSZ}_{\boldsymbol{\ell}_1} T^{\rm kSZ}_{\boldsymbol{\ell}_2} \phi'_{\boldsymbol{\ell}_3} \phi'_{\boldsymbol{\ell}_4}\rangle_{\rm c} \to \text{(b4)}\end{aligned} \tag{90}$$

type c:

$$
\begin{aligned}
&\langle T^{\rm kSZ}_{\boldsymbol{\ell}_1} T_{\boldsymbol{\ell}_2}\phi_{\boldsymbol{\ell}_2} T'^{\rm kSZ}_{\boldsymbol{\ell}_3} T'_{\boldsymbol{\ell}_4}\phi'_{\boldsymbol{\ell}_4}\rangle \\
=&\langle \overbrace{T^{\rm kSZ}_{\boldsymbol{\ell}_1} T_{\boldsymbol{\ell}_2}\phi_{\boldsymbol{\ell}_2} T'^{\rm kSZ}_{\boldsymbol{\ell}_3} T'_{\boldsymbol{\ell}_4}\phi'_{\boldsymbol{\ell}_4}}\rangle \\
=&\langle \overbrace{T^{\rm kSZ}_{\boldsymbol{\ell}_1} T_{\boldsymbol{\ell}_2}\phi_{\boldsymbol{\ell}_2} T'^{\rm kSZ}_{\boldsymbol{\ell}_3} T'_{\boldsymbol{\ell}_4}\phi'_{\boldsymbol{\ell}_4}}\rangle \to \text{(c1)} \\
+&\langle \overbrace{T^{\rm kSZ}_{\boldsymbol{\ell}_1} T_{\boldsymbol{\ell}_2}\phi_{\boldsymbol{\ell}_2} T'^{\rm kSZ}_{\boldsymbol{\ell}_3} T'_{\boldsymbol{\ell}_4}\phi'_{\boldsymbol{\ell}_4}}\rangle \to \text{(c2)} \\
+&\langle \overbrace{T^{\rm kSZ}_{\boldsymbol{\ell}_1} T_{\boldsymbol{\ell}_2}\phi_{\boldsymbol{\ell}_2} T'^{\rm kSZ}_{\boldsymbol{\ell}_3} T'_{\boldsymbol{\ell}_4}\phi'_{\boldsymbol{\ell}_4}}\rangle \to \text{(c3)} \\
+&\langle T_{\boldsymbol{\ell}_2} T'_{\boldsymbol{\ell}_4}\rangle\langle T^{\rm kSZ}_{\boldsymbol{\ell}_1}\phi_{\boldsymbol{\ell}_2} T'^{\rm kSZ}_{\boldsymbol{\ell}_3}\phi'_{\boldsymbol{\ell}_4}\rangle_{\rm c} \to \text{(c4)}
\end{aligned}
\tag{91}
$$

type d:

$$
\begin{aligned}
&\langle T^{\rm kSZ}_{\boldsymbol{\ell}_1} T^{\rm kSZ}_{\boldsymbol{\ell}_2} T'^{\rm kSZ}_{\boldsymbol{\ell}_3} T'^{\rm kSZ}_{\boldsymbol{\ell}_4}\rangle \\
=&\langle \overbrace{T^{\rm kSZ}_{\boldsymbol{\ell}_1} T^{\rm kSZ}_{\boldsymbol{\ell}_2}}\, \overbrace{T'^{\rm kSZ}_{\boldsymbol{\ell}_3} T'^{\rm kSZ}_{\boldsymbol{\ell}_4}}\rangle \to \text{(d1)} \\
+&\langle \overbrace{T^{\rm kSZ}_{\boldsymbol{\ell}_1} \overbrace{T^{\rm kSZ}_{\boldsymbol{\ell}_2} T'^{\rm kSZ}_{\boldsymbol{\ell}_3}}\, T'^{\rm kSZ}_{\boldsymbol{\ell}_4}}\rangle \to \text{(d2)} \\
+&\langle \overbrace{T^{\rm kSZ}_{\boldsymbol{\ell}_1} \overbrace{T^{\rm kSZ}_{\boldsymbol{\ell}_2} T'^{\rm kSZ}_{\boldsymbol{\ell}_3}}\, T'^{\rm kSZ}_{\boldsymbol{\ell}_4}}\rangle \to \text{(d3)} \\
+&\langle T^{\rm kSZ}_{\boldsymbol{\ell}_1} T^{\rm kSZ}_{\boldsymbol{\ell}_2} T'^{\rm kSZ}_{\boldsymbol{\ell}_3} T'^{\rm kSZ}_{\boldsymbol{\ell}_4}\rangle_{\rm c} \to \text{(d4)}
\end{aligned}
\tag{92}
$$

(b1), (c1), (d1), (d2), (d3) are disconnected terms of Eq. (84), which should be accounted for in the reconstruction Gaussian bias in Eq. (75). Since $T^{\rm kSZ,g}$ produces the same terms, these terms cancel in Eq. (81).

(a1) is a connected term of Eq. (84), which includes a $< T^{\rm kSZ} T^{\rm kSZ}\phi >$ bispectrum. (b2), (b3), (c2), (c3) are connected terms of Eq. (84), which include kSZ-lensing two-point coupling introduced in [81, 82]. All these connected terms arise from the kSZ-lensing correlation, and are only non-negligible for the case of late-time kSZ [7]. They do not cancel in Eq. (81) by $T^{\rm kSZ,g}$, and contribute to the bias.

(b4) and (c4) are connected terms of Eq. (84). They include the connected part of the 4-point function involving two kSZ and two lensing fields (denoted by the subscript c), which do not cancel in Eq. (81). These terms may arise from both the intrinsic non-Gaussianity of ϕ and $T^{\rm kSZ}$.

(d4) is a connected term of Eq. (84), which includes the connected part of kSZ trispectrum due to its non-Gaussianity. It does not cancel in Eq. (81), and exists for both late-time kSZ

and reionization kSZ. To estimate the contribution of this term, we can run CMB lensing reconstruction algorithm on $T^{\rm kSZ}$ as Eq. (82) shows.

5 Simulations and results

As explained in Section 3, we apply the CMB lensing reconstruction algorithm to a set of independent reionization kSZ realizations. These realizations are cut from a full-sky kSZ map provided by the WebSky[g] extragalactic CMB simulations [5].

The reionization kSZ temperature map is provided in blackbody thermodynamic temperature units, and is constructed from the free electron and velocity fields at $z > 5.5$. It is uncorrelated with the lensing map and the primary unlensed CMB map. The reionization kSZ simulation [80] uses 4096^3 elements in a periodic box of side length 8 Gpc/h. Three astrophysical reionization parameters define the simulation: $M_{\rm min}$, the minimum halo mass capable of hosting ionizing sources; $\lambda_{\rm abs}$, the comoving absorption system (Lyman-limit absorption systems) mean free path; and $\zeta_{\rm ion}$, the number of ionizing photons per atom escaping each halo [80]. These parameters are chosen as $M_{\rm min} = 10^9 M_\odot$, $\lambda_{\rm abs} = 50\,{\rm Mpc}/h$ and $\zeta_{\rm ion} = 50$, and yield a total Thomson scattering optical depth of $\tau = 0.059$ and a mean redshift of reionization of $z_{\rm re} = 7.93$ [h], consistent with current constraints from *Planck* [2].

We perform the following analysis on this simulation:

1. We get one full-sky reionization kSZ map $T^{\rm kSZ}(\hat{\boldsymbol{n}})$, where the direction vector $\hat{\boldsymbol{n}}$ indicates a full-sky map.
2. We generate 30 full-sky Gaussian reionization kSZ maps $T^{\rm kSZ,g}(\hat{\boldsymbol{n}})$ with the same average power spectrum as that of $T^{\rm kSZ}(\hat{\boldsymbol{n}})$ using `healpy`.[i] We use multiple Gaussian kSZ realizations to average down the statistical error.
3. We select regions spanning $\pm 45^\circ$ in declination and 360° in RA from $T^{\rm kSZ}(\hat{\boldsymbol{n}})$ and $T^{\rm kSZ,g}(\hat{\boldsymbol{n}})$ using `pixell`[j]. In the pixel space, the regions correspond to 21600 pixels in

[g] `https://lambda.gsfc.nasa.gov/simulation/tb_mocks_data.cfm`
[h] `https://www.cita.utoronto.ca/~malvarez/research/ksz-data/run_params.txt`
[i] `https://github.com/healpy/healpy`
[j] `https://github.com/simonsobs/pixell`

width and 5400 pixels in height in our simulation. We cut 36 non-overlapping patches with 1800 pixels both in width and in height from each of the regions. So we obtain a set of 36 reionization kSZ cutouts $T^{\rm kSZ}(\mathbf{x})$ and a set of 1080 Gaussian reionization kSZ cutouts $T^{\rm kSZ,g}(\mathbf{x})$, where the position vector $\mathbf{x}$ indicates we treat these cutouts under the flat-sky approximation. Because the cutouts are approximately independent regions, we consider them as independent realizations.

4. We run the `symlens`[k] flat-sky CMB lensing reconstruction algorithm on the sets of $T^{\rm kSZ}(\mathbf{x})$ cutouts and $T^{\rm kSZ,g}(\mathbf{x})$ cutouts, and get two sets of reconstructed convergence maps: $\hat{\kappa}_{\rm kSZ}(\mathbf{x})$ and $\hat{\kappa}_{\rm kSZ,g}(\mathbf{x})$. Their power spectra $C^{\hat{\kappa}\hat{\kappa}}_{L,\rm kSZ}$ and $C^{\hat{\kappa}\hat{\kappa}}_{L,\rm kSZ,g}$ are bandpowers binned in the two-dimensional reconstructed Fourier κ maps. We use a multipole bin width $\Delta L = 150$ for the analyses with $\ell_{\rm max} = 3000$ and $\Delta L = 200$ for $\ell_{\rm max} = 4000$, where $\ell_{\rm max}$ is the maximum temperature multipole for CMB lensing reconstruction.
5. Following [7], note that we do not include the contribution of detector noise $T^{\rm det}(\mathbf{x})$, making the results less noisy without being biased. The detector noise Fourier modes $T^{\rm det}(\boldsymbol{\ell})$ are only included in the denominator of the weight $g(\boldsymbol{\ell}, \mathbf{L})$ in Eq. (72).
6. The reionization kSZ-induced bias $(\Delta C^{\kappa\kappa}_L)_{\rm kSZ}$ is estimated by Eq. (82). Note that in Eq. (82), the angle brackets in the first term indicate the average bandpower of the set of 36 $C^{\hat{\kappa}\hat{\kappa}}_{L,\rm kSZ}$ and the second pair is the average bandpower of the set of 1080 $C^{\hat{\kappa}\hat{\kappa}}_{L,\rm kSZ,g}$ in our simulations.
7. The fractional bias is defined as $\frac{(\Delta C^{\kappa\kappa}_L)_{\rm kSZ}}{C^{\kappa\kappa}_L}$, where $C^{\kappa\kappa}_L$ is the power spectrum of the true CMB lensing convergence field. The error bar on $(\Delta C^{\kappa\kappa}_L)_{\rm kSZ}$ is estimated from the Gaussian kSZ realizations.
8. As a comparison, we apply Step 1 to Step 5 above to the late-time kSZ simulations from WebSky to estimate the bias to CMB lensing reconstruction from the late-time kSZ trispectrum using Eq. (82). The late-time kSZ full-sky map from WebSky is constructed from the free electron and velocity fields at $z < 4.5$.
9. We also estimate the full bias to CMB lensing reconstruction from the late-time kSZ field, i.e., including terms from the kSZ trispectrum and the kSZ-lensing correlation, by substituting $T^{\rm ksz}(\hat{\boldsymbol{n}})$ and $T^{\rm ksz,g}(\hat{\boldsymbol{n}})$ with $T^{\rm tot}(\hat{\boldsymbol{n}})$ and $T^{\rm tot,g}(\hat{\boldsymbol{n}})$ in Step 1, where $T^{\rm tot}(\hat{\boldsymbol{n}}) =$

[k] `https://github.com/simonsobs/symlens`

$\tilde{T}(\hat{\boldsymbol{n}}) + T^{\rm kSZ}(\hat{\boldsymbol{n}})$ and $T^{\rm tot,g}(\hat{\boldsymbol{n}}) = \tilde{T}(\hat{\boldsymbol{n}}) + T^{\rm kSZ,g}(\hat{\boldsymbol{n}})$. $\tilde{T}(\hat{\boldsymbol{n}})$ is a full-sky lensed CMB temperature map and $T^{\rm kSZ}(\hat{\boldsymbol{n}})$ refers to the late-time kSZ full-sky map from WebSky. The full bias from the late-time kSZ field is estimated using Eq. (81).

In Fig. 11, we show the fractional bias to the CMB lensing power spectrum induced by the reionization kSZ trispectrum, the late-time kSZ trispectrum, and the full late-time kSZ for Planck, CMB-S3-like, and CMB-S4-like experiments with $\ell_{\rm max} = 3000$ or $\ell_{\rm max} = 4000$, where $\ell_{\rm max}$ is the maximum temperature multipole used in the CMB lensing reconstruction. The experimental configurations are defined in Table 1; in order to facilitate comparison, we adopt the same settings as used in [7]. The curves showing the bias from the reionization kSZ trispectrum and the late-time kSZ trispectrum in Fig. 11 have been multiplied by a factor of 20 for visibility. We can see the fractional bias from the reionization kSZ trispectrum is positive and smaller than 0.25% at most scales, except for the largest scales when considering $\ell_{\rm max} = 4000$. The late-time kSZ trispectrum produces a comparable bias to that from the reionization kSZ trispectrum. The full bias from the late-time kSZ signal is at least one order of magnitude larger than the other two. For all three cases, the bias with $\ell_{\rm max} = 4000$ is larger than that with $\ell_{\rm max} = 3000$, as expected since more foreground-contaminated modes are used in the former case. Since the reionization kSZ field is only weakly correlated with the CMB lensing field, it is safe to use the bias from the reionization kSZ trispectrum to approximate the full bias from the reionization kSZ field. Thus the full reionization kSZ bias is much less significant than the full late-time kSZ bias to the reconstructed CMB lensing power spectrum.

In Fig. 12, we show the absolute bias from the reionization kSZ trispectrum to the reconstructed CMB lensing convergence power spectrum for different experiments along with the true power spectrum of CMB lensing convergence. Within this L range, the reionization kSZ-induced bias is at least two orders of magnitude lower than the lensing convergence power spectrum for CMB-S3-like and CMB-S4-like experiments using $\ell_{\rm max} = 4000$, three orders of magnitude lower for CMB-S3 and CMB-S4 with $\ell_{\rm max} = 3000$, and four orders of magnitude lower for Planck SMICA.

In Fig. 13, we show the full kSZ-induced fractional bias to the CMB lensing power spectrum computed using the WebSky simulation and using the Sehgal et al. simulation[6].

CMB Experiment	Noise Level Δ_T [μK arcmin]	Beam FWHM $\theta_{\rm FWHM}$ [arcmin]
Planck SMICA	45	5
CMB-S3-like	7	1.4
CMB-S4-like	1	3

Table 1: Experimental configurations. Note that the actual beam FWHM for the CMB-S4 reference design is 1.4 arcmin [50]. We use 3 arcmin in this work to facilitate comparison with [7].

The latter result is taken directly from [7]. The CMB multipole ranges and experimental configurations are the same as those in Fig. 12. For both sets of results, the full late-time kSZ-induced bias is smaller than the statistical error bars for Planck. For CMB-S3 and CMB-S4, the bias is negative and about several percent for $\ell_{\rm max} = 4000$, and about half that for $\ell_{\rm max} = 3000$. For CMB-S3 and CMB-S4 with $\ell_{\rm max} = 4000$, the bias from the WebSky simulation is about 1.5 to 2 times of that computed using the Sehgal et al. simulation. This is consistent with the result in Fig. 14, which shows that the bispectrum of $< T^{\rm kSZ} T^{\rm kSZ} \kappa >$ is larger in the WebSky simulation than in the Sehgal et al. simulation, where $T^{\rm kSZ}$ refers to the late-time kSZ signal and κ is the CMB lensing convergence. This bispectrum appears in Eq. (89) in Section. 4, which is the largest overall connected term of CMB trispectrum contributing to the late-time kSZ-induced bias. The difference in these predicted biases also reflects the current uncertainty in our understanding of the late-time kSZ field, and indicates that data-driven methods should be used to mitigate the kSZ bias, rather than methods assuming particular theoretical models.

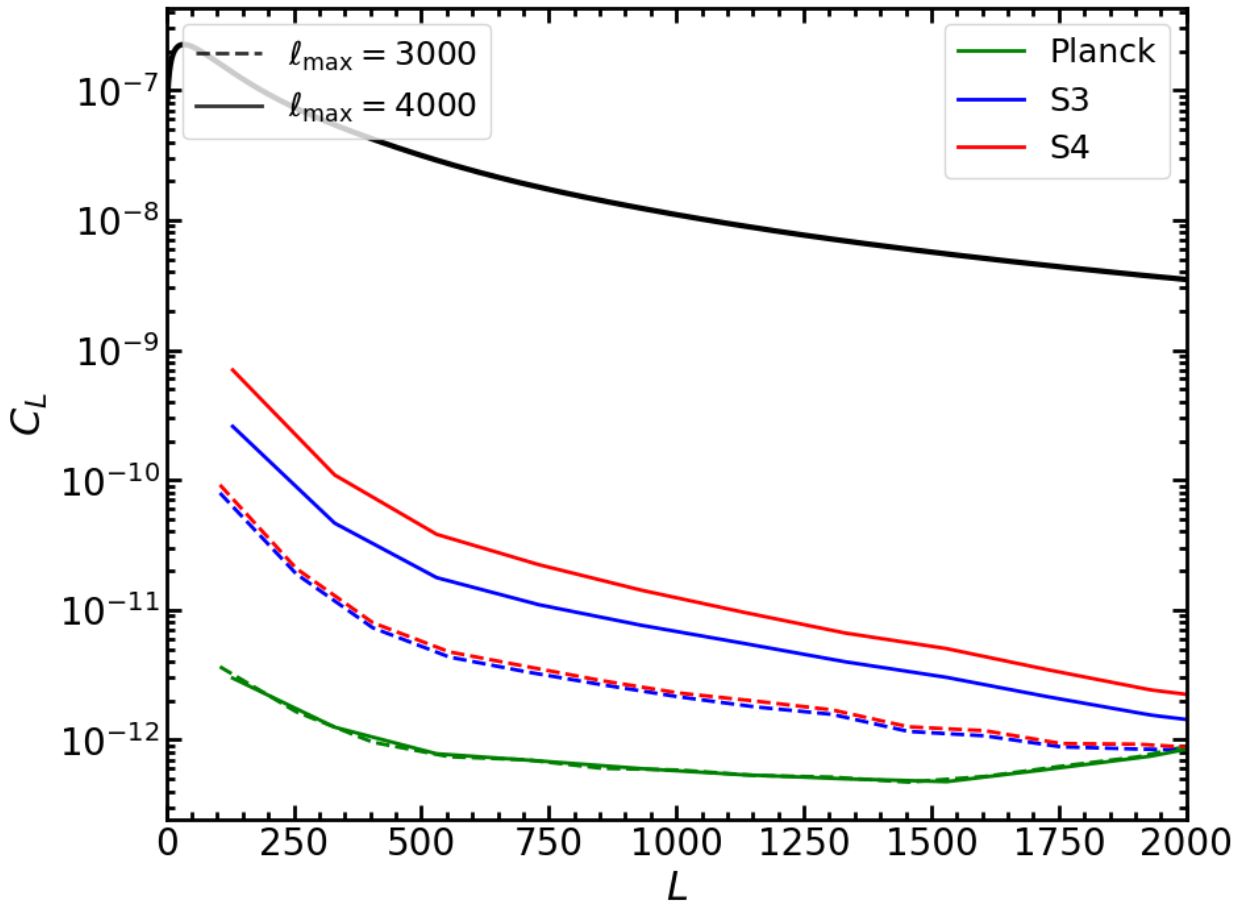

Figure 12: The bias to the reconstructed CMB lensing convergence power spectrum from reionization kSZ trispectrum using $\ell_{\rm max} = 3000$ (dashed lines) and $\ell_{\rm max} = 4000$ (solid lines) for Planck SMICA, CMB-S3-like, and CMB-S4-like experiments. The true power spectrum of the CMB lensing convergence is also shown (black solid line).

6 Discussion and conclusion

The kSZ effect is the largest blackbody contaminant to the CMB primary temperature anisotropies, and it cannot be removed by multifrequency component separation techniques. The kSZ signal has two contributions, the late-time contribution and the reionization con-

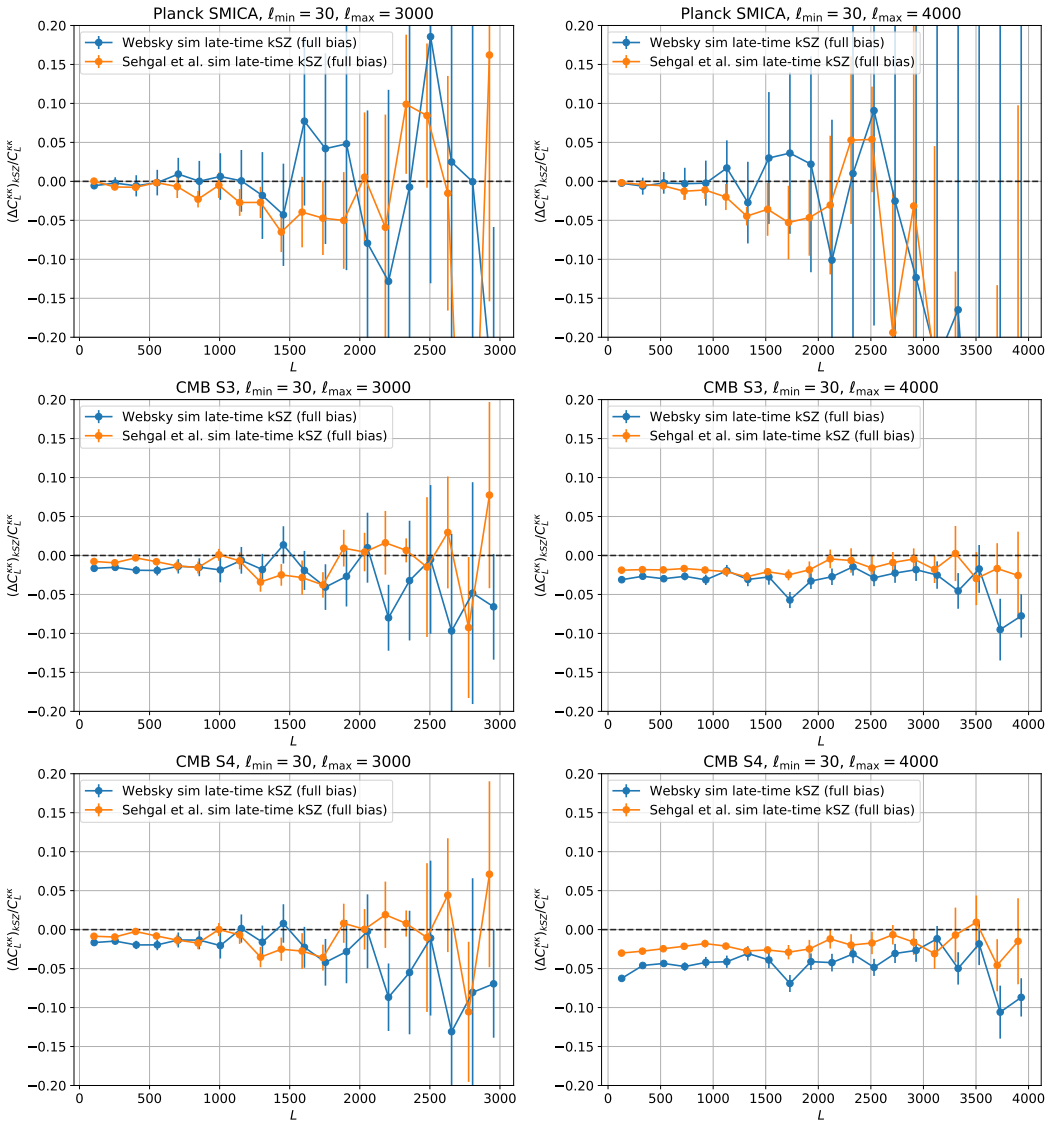

Figure 13: The full late-time-kSZ-induced fractional bias to the reconstructed CMB lensing convergence power spectrum computed using the WebSky simulation [5] (blue curves) and using the Sehgal et al. simulation [6] (orange curves, taken from [7]). The experimental settings and temperature multipole ranges used in the lensing reconstruction are identical to those in Fig. 11.

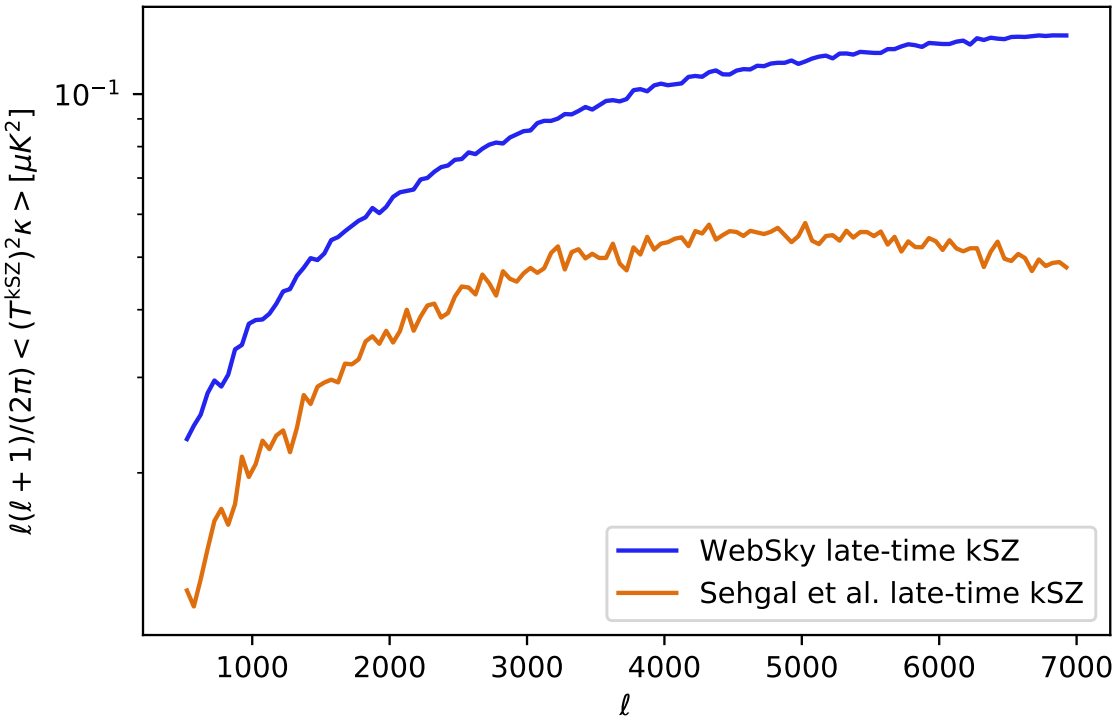

Figure 14: A projection of the $\left\langle T^{\rm kSZ}T^{\rm kSZ}\kappa\right\rangle$ bispectrum estimated from the cross-correlation of $T^2_{\rm kSZ}$ and κ, shown for each of the WebSky late-time kSZ (blue) and the Sehgal et al. late-time kSZ (orange) simulations. The curves have been binned with $\Delta\ell = 50$. Despite lower two-point power in the kSZ anisotropies for the WebSky simulation, the cross-bispectrum with CMB lensing is larger, which agrees with our observation that the bias to CMB lensing is larger in the WebSky simulation.

tribution. In this paper, we focus on the bias to the reconstructed CMB lensing convergence power spectrum induced by the reionization kSZ signal. Since the reionization kSZ field is only weakly correlated with the CMB lensing field, its trispectrum should be the dominant contribution to the bias to CMB lensing reconstruction. We estimate this bias by applying the flat-sky CMB lensing reconstruction algorithm to reionization kSZ simulations

and corresponding Gaussian realizations with the same power spectrum. We also apply the same method to estimate the bias to CMB lensing reconstruction from the late-time kSZ trispectrum alone, and the full late-time kSZ-induced bias.

Using the WebSky simulation, we find that the fractional bias from the reionization kSZ signal is positive and smaller than 0.25% at $L < 3000$ when using $\ell_{\rm max} = 4000$ for CMB-S3-like and CMB-S4-like experiments, and can be even smaller when using $\ell_{\rm max} = 3000$. The fractional bias computed using the WebSky late-time kSZ field is more than 10 times larger than that from the reionization kSZ field, which implies that the latter one is negligible for ongoing and upcoming experiments. These conclusions are based on the current numerical simulations of reionization from WebSky, and results may differ somewhat for other reionization models; however, the reionization-induced bias is very unlikely to be comparable to that from the late-time kSZ field for any reasonable reionization model.

As a comparison, we show that the bias induced by the late-time kSZ trispectrum is comparable to that induced by the reionization kSZ field, which are both much smaller than the full late-time kSZ bias. Thus, for the late-time kSZ, the kSZ-lensing correlation contributes much more than the kSZ trispectrum, as also found earlier in [7] (see their Fig. 6).

In addition, we compare the bias from the late-time kSZ field computed using the WebSky simulation to that computed using the Sehgal et al. simulation in [7]. For CMB-S3 and CMB-S4 with $\ell_{\rm max} = 4000$, we find that the absolute value of the former is about 1.5 to 2 times larger than the latter. Considering the statistical precision of CMB-S3 and CMB-S4, we confirm that the bias to CMB lensing reconstruction from the late-time kSZ effect is non-negligible and requires mitigation techniques, such as foreground-hardened estimators [62, 63, 64] or shear-only reconstruction [61]. The former technique effectively deprojects a point-source-like trispectrum from the lensing power spectrum measurement, which is expected to work well for the late-time kSZ signal. For the latter technique, since the lensing shear (local quadrupolar distortion) is less degenerate with the extragalactic foregrounds, the shear-only reconstruction is less sensitive to foregrounds. Applying the shear-only technique to mitigate the kSZ-induced bias was done for the Sehgal et al. kSZ bias in [61]; we leave similar analysis for the WebSky simulations to future work.

3.0 Computing Microwave Background Polarization Power Spectra from Cosmic Birefringence

The content of this chapter is based on the manuscript published in Physical Review D [8]. We present a new publicly available code, `class_rot`, which modifies `class` to enable fast non-perturbative calculation of cosmic microwave background polarization power spectra due to both isotropic and anisotropic polarization rotation from cosmic birefringence. Cosmic birefringence can arise from new parity-violating physics such as axion dark matter with a Chern-Simons coupling to photons or Faraday rotation due to a primordial magnetic field. Constraints on these effects can be obtained by comparing measurements to precise numerical calculations of the polarization power spectra. We describe the implementation of `class_rot` in terms of both mathematical formalism and coding architecture. We also provide usage examples and demonstrate the accuracy of the code by comparing with simulations.

1 Introduction

Parity-violating physics in the early universe may cause an effect known as cosmic birefringence, in which photons with different polarizations travel differently along their propagation paths, resulting in a net rotation on the polarization directions of cosmic microwave background (CMB) photons [83, 84, 85, 86]. Such an effect can arise from many types of beyond-the-Standard-Model physics, such as from the coupling between axion-like particles and photons through a Chern-Simons interaction (see, e.g., [87]), from pseudoscalar fields introduced in early dark energy models to resolve the Hubble tension [88], from quintessence as a candidate for dark energy [89], or from primordial magnetic fields through Faraday rotation (see, e.g., [90]).

Cosmic birefringence can cause both isotropic and anisotropic rotation of the microwave background polarization. Since the polarization field is dominated by an E-mode signal from primordial density perturbations, small rotations of polarization effectively turn E-mode into

B-mode polarization, leaving observable imprints in the polarization power spectra. Isotropic birefringence, in particular, leads to non-zero parity-odd power spectra in the CMB including TB and EB (see, e.g., [87, 91]). Various experiments have placed constraints on isotropic rotation angle, such as Planck [92], WMAP [93], and ACT [94]. The observational challenge in constraining isotropic birefringence is that its effect is highly degenerate to that of a calibration error in the orientation of polarized detectors (see, e.g., [95, 96]).

Anisotropic birefringence, on the other hand, leads only to parity-even spectra and contributes non-negligibly to the B-mode power spectrum. Anisotropic rotation also induces off-diagonal correlations in the microwave background multipoles, which allows reconstruction of the anisotropic rotation field using a quadratic estimator approach similar to lensing reconstruction of the deflection field (see, e.g., [97, 98, 99]). Such an effect has been used to derive observational constraints on anisotropic rotation; for examples, Planck [100], BICEP2 / Keck [101], ACT [15], and SPT [102] have all derived upper bounds on anisotropic rotation field with a scale-invariant power spectrum.

Despite the physical importance of a possible rotation field, to our knowledge no publicly available codes exist that compute CMB power spectra from cosmic birefringence. Here we present a modified version of `class` [103][a], named `class_rot`[b], which implements this calculation and allows for fast computation of the rotated EB, TB, EE, and BB power spectra due to both isotropic and anisotropic rotation from cosmic birefringence. In particular, we implement a non-perturbative calculation based on the angular correlation function of the rotation field [104]. Our code has an accuracy better than 1% at all multipoles from $l = 2$ to $l = 4000$, which we verify through comparison with power spectra of simulated sky maps including random rotation fields.

This paper is structured as follows. In Sec. 2, we describe the basics of cosmic birefringence. In Sec. 3 we show the non-perturbative calculation method that is implemented in `class_rot`, focusing on the effect of cosmic birefringence on the CMB power spectra. In Sec. 4, we present comparisons between the results from `class_rot` and numerical simulations. Sec. 6 provides a brief concluding discussion about the uses of this code in the context

[a] `https://github.com/lesgourg/class_public`
[b] `https://github.com/catketchup/class_rot`

of current and upcoming experiments. In addition, we discuss the code implementation and give usage examples in Sec. 5.

2 Cosmic rotation field

The rotation effect from cosmic birefringence can be effectively expressed as a rotation field $\alpha(\hat{\boldsymbol{n}})$, which can have both an isotropic part and an anisotropic part [91], given by

$$\alpha(\hat{\boldsymbol{n}}) = \bar{\alpha} + \delta\alpha(\hat{\boldsymbol{n}}), \tag{93}$$

with $\bar{\alpha}$ the isotropic part, and $\delta\alpha(\hat{\boldsymbol{n}})$ the anisotropic part with a zero mean,

$$\langle \delta\alpha(\hat{\boldsymbol{n}}) \rangle = 0. \tag{94}$$

As a result of rotation, Stokes parameter Q and U transform as

$$(\tilde{Q} \pm i\tilde{U})(\hat{\boldsymbol{n}}) = \exp(\pm i2\alpha(\hat{\boldsymbol{n}}))(Q \pm iU)(\hat{\boldsymbol{n}}), \tag{95}$$

where we have used tildes to denote rotated quantities.

To illustrate how such a rotation field can arise from parity-violating physics in the early universe, consider for example a Chern-Simons-type interaction of photons and axions with a Lagrangian given by

$$\mathcal{L}_{cs} = \frac{\beta\phi}{2M} F^{\mu\nu}\tilde{F}_{\mu\nu}, \tag{96}$$

where β is a dimensionless coupling constant, ϕ is the axion field, M is its mass scale, and $F^{\mu\nu}$ is the electromagnetic tensor with $\tilde{F}_{\mu\nu}$ being its dual. This term modifies the Euler-Lagrange equations for electromagnetic field and induces a rotation in the polarization direction of a photon if ϕ varies along its propagation path [105, 106, 107], with the rotation angle given by

$$\alpha = \frac{\beta}{M}\Delta\phi, \tag{97}$$

where $\Delta\phi$ is the change of ϕ along the photon path. In the case that the axion field ϕ is spatially homogeneous, Eq. (125) introduces an isotropic rotation field to the CMB; an inhomogeneous axion field gives an anisotropic rotation field in the CMB.

A convenient way to express an anisotropic rotation field, $\alpha(\hat{\boldsymbol{n}})$, is to expand it in the basis of spherical harmonics as

$$\delta\alpha(\hat{\boldsymbol{n}}) = \sum_{LM} \alpha_{LM} Y_{LM}(\hat{\boldsymbol{n}}). \tag{98}$$

We assume that $\alpha(\hat{\boldsymbol{n}})$ follows Gaussian random statistics, in which case the statistical information of the rotation field $\alpha(\hat{\boldsymbol{n}})$ can be completely specified by its power spectrum $C_L^{\alpha\alpha}$, given by

$$\langle a_{LM} a_{L'M'} \rangle = \delta_{LL'} \delta_{MM'} C_L^{\alpha\alpha}. \tag{99}$$

In this paper we only consider a scale-invariant power spectrum of the anisotropic rotation field, which is physically well-motivated [108], though the formalism presented here is broadly applicable to an arbitrary rotation field power spectrum. Following the convention in [50], we parametrize a scale-invariant power spectrum as

$$\frac{L(L+1)}{2\pi} C_L^{\alpha\alpha} = A_{CB}, \tag{100}$$

with A_{CB} the amplitude of the cosmic birefringence power spectrum[c].

3 Impacts on microwave background polarization power spectra

In this section, we briefly review the rotated CMB power spectra calculation implemented in `class_rot`. We consider a rotation field with both an isotropic contribution and an Gaussian random anisotropic contribution as described in Eq. (93). We adopt the non-perturbative method introduced in [104], which is similar to the calculation method of lensed CMB power spectra in [109]. Here we briefly review the non-perturbative calculations relevant to the implementation of `class_rot`; we refer interested readers to [104] for more calculation details.

[c]Note that A_{CB} defined in this paper is 10^{-4} times of that in [15] and 10^{-5} of that in [99].

In this method, the starting point is to connect the real-space correlation functions of rotated quantities, such as $\tilde{T}(\hat{\boldsymbol{n}})$, $\tilde{Q}(\hat{\boldsymbol{n}})$, and $\tilde{U}(\hat{\boldsymbol{n}})$, to the rotated power spectra, e.g., $\tilde{C}_{\ell'}^{EE}$, $\tilde{C}_{\ell'}^{BB}$, with

$$\begin{aligned}
\tilde{\xi}_+(\beta) &\equiv \left\langle (\tilde{Q}+i\tilde{U})^*(\hat{\boldsymbol{n}})(\tilde{Q}+i\tilde{U})\,(\hat{\boldsymbol{n}}')\right\rangle \\
&= \sum_{\ell'} \frac{2\ell'+1}{4\pi}\left(\tilde{C}_{\ell'}^{EE}+\tilde{C}_{\ell'}^{BB}\right) d_{22}^{\ell'}(\beta), \\
\tilde{\xi}_-(\beta) &\equiv \left\langle (\tilde{Q}+i\tilde{U})(\hat{\boldsymbol{n}})(\tilde{Q}+i\tilde{U})\,(\hat{\boldsymbol{n}}')\right\rangle \\
&= \sum_{\ell'} \frac{2\ell'+1}{4\pi}\left(\tilde{C}_{\ell'}^{EE}-\tilde{C}_{\ell'}^{BB}+2i\tilde{C}_{\ell'}^{EB}\right) d_{-22}^{\ell'}(\beta), \\
\tilde{\xi}_X(\beta) &\equiv \left\langle T(\hat{\boldsymbol{n}})(\tilde{Q}+i\tilde{U})\,(\hat{\boldsymbol{n}}')\right\rangle \\
&= -\sum_{\ell'} \frac{2\ell'+1}{4\pi}\left(\tilde{C}_{\ell'}^{TE}+i\tilde{C}_{\ell'}^{TB}\right) d_{02}^{\ell'}(\beta),
\end{aligned} \tag{101}$$

where $\hat{\boldsymbol{n}}$ and $\hat{\boldsymbol{n}}'$ are two directions in the spherical coordinate system, $\cos\beta = \hat{\boldsymbol{n}}\cdot\hat{\boldsymbol{n}}'$, and $d_{mm'}^{\ell}$ is the Wigner d-function. Taking advantages of the orthogonality relations of Wigner d-functions,

$$\int_{-1}^{1} d\cos\beta\, d_{mk}^{\ell}(\beta) d_{m'k'}^{\ell'}(\beta) = \frac{2}{2\ell+1}\delta_{mm'}\delta_{kk'}\delta_{\ell\ell'}, \tag{102}$$

one can invert Eq. (101) to express rotated power spectra in terms of correlation functions, such as

$$\tilde{C}_{\ell}^{EE}+\tilde{C}_{\ell}^{BB} = 2\pi\int_{-1}^{1} d\cos\beta\,\tilde{\xi}_+(\beta) d_{22}^{\ell}(\beta). \tag{103}$$

Applying Eq. (123), $\tilde{\xi}_+(\beta)$ can be expressed by un-rotated quantities as

$$\tilde{\xi}_+(\beta) = e^{-4C^{\alpha}(0)+4C^{\alpha}(\beta)}\sum_{\ell'}(2\ell'+1)(C_{\ell'}^{EE}+C_{\ell'}^{BB}) d_{22}^{\ell'}(\beta). \tag{104}$$

Here $C^{\alpha}(\beta)$ is the correlation function of rotation angles in the two directions separated by β and can be expressed as

$$\begin{aligned}
C^{\alpha}(\beta) = \langle \delta\alpha\,(\hat{\boldsymbol{n}}_1)\,\delta\alpha\,(\hat{\boldsymbol{n}}_2)\rangle &= \sum_{L}\frac{2L+1}{4\pi} C_L^{\alpha\alpha} P_L(\cos\beta) \\
&= \sum_{L}\frac{2L+1}{4\pi} C_L^{\alpha\alpha} d_{00}^{L}(\beta),
\end{aligned} \tag{105}$$

where $C_L^{\alpha\alpha}$ is a generic rotation field power spectrum introduced in Eq. (99), $P_L(\cos\beta)$ is the Legendre Polynomial, and we have applied $P_L(\cos\beta) = d_{00}^{L}(\beta)$. When $\beta = 0$, $C^{\alpha}(0) =$

$\langle \delta\alpha(\hat{\boldsymbol{n}})\delta\alpha(\hat{\boldsymbol{n}})\rangle$ is the variance of the rotation angles. For example, with $A_{CB} = 10^{-5}$ as we will choose throughout this paper, $C^\alpha(0) \approx 7.92 \times 10^{-5} \approx 0.26$ deg^2; this corresponds to a rotation field with a standard deviation around 0.5°.

Equipped with Eq. (104), Eq. (103) can be written as

$$\begin{aligned} \tilde{C}_\ell^{EE} + \tilde{C}_\ell^{BB} = \frac{1}{2} e^{-4C^\alpha(0)} \int d\cos\beta \, e^{4C^\alpha(\beta)} d^\ell_{22}(\beta) \\ \left[\sum_{\ell'} (2\ell'+1)(C_{\ell'}^{EE} + C_{\ell'}^{BB}) d^{\ell'}_{22}(\beta) \right]. \end{aligned} \tag{106}$$

Similarly, one can also obtain

$$\begin{aligned} \tilde{C}_\ell^{TE} &= C_\ell^{TE} \cos(2\bar{\alpha}) e^{-2C^\alpha(0)}, \\ \tilde{C}_\ell^{TB} &= C_\ell^{TE} \sin(2\bar{\alpha}) e^{-2C^\alpha(0)}, \\ \tilde{C}_\ell^{EE} - \tilde{C}_\ell^{BB} &= \frac{1}{2} e^{-4C^\alpha(0)} \cos 4\bar{\alpha} \int d\cos\beta \, e^{-4C^\alpha(\beta)} d^\ell_{-22}(\beta) \\ &\quad \left[\sum_{\ell'} (2\ell'+1)(C_{\ell'}^{EE} - C_{\ell'}^{BB}) d^{\ell'}_{-22}(\beta) \right], \\ \tilde{C}_\ell^{EB} &= \frac{1}{2} e^{-4C^\alpha(0)} \sin 4\bar{\alpha} \int d\cos\beta \, e^{-4C^\alpha(\beta)} d^\ell_{-22}(\beta) \\ &\quad \left[\sum_{\ell'} (2\ell'+1)(C_{\ell'}^{EE} - C_{\ell'}^{BB}) d^{\ell'}_{-22}(\beta) \right]. \end{aligned} \tag{107}$$

Note that the rotated CMB EE, BB and EB power spectra in Eq. (106) and Eq. (107) are given by real-space integrals, which avoids convolution in the ℓm space which is computationally expensive. A similar strategy that uses real-space integral instead of convolution in ℓm space can be found in delensing calculation [110] which significantly reduces computational cost. Also note that we have ignored the correlations between the rotation field and both CMB temperature and (unrotated) E-polarization fields, which may arise in certain axion-like models, such as models with nonzero potential under adiabatic initial conditions [108]. A similar calculation that takes account of these correlations can be found in [91].

We can see from Eq. (106) and Eq. (107) that both isotropic and anisotropic rotations contribute to BB power spectrum. In the upper panel of Fig. 15, we show the BB power spectrum contributed by an isotropic rotation field with $\bar{\alpha} = 0.1°$ and a scale-invariant

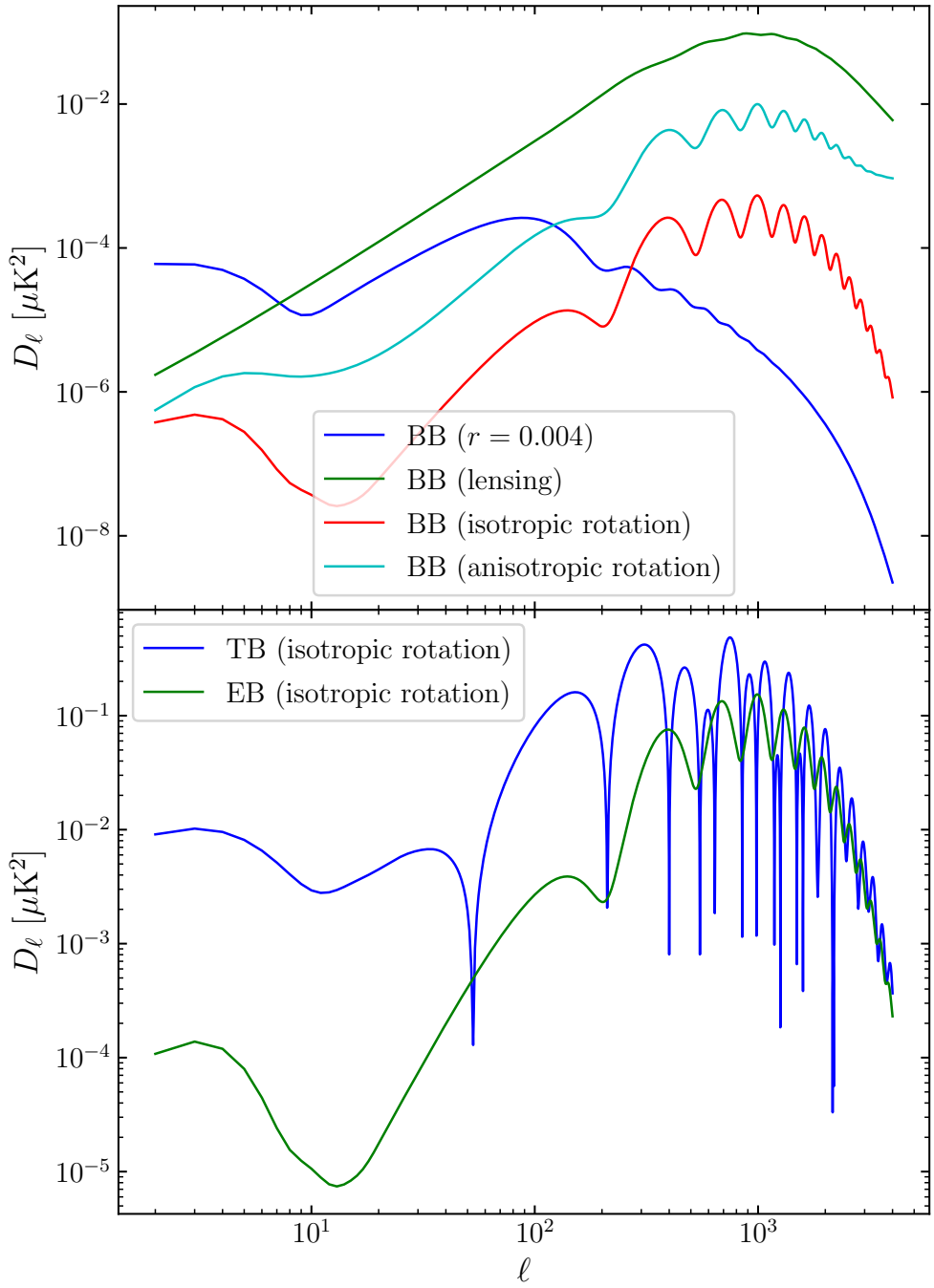

Figure 15: Microwave background polarization BB power spectrum contributions from a scale-invariant tensor mode ($r = 0.004$), gravitational lensing, isotropic rotation ($\bar{\alpha} = 0.1°$) and scale-invariant anisotropic rotation ($A_{CB} = 10^{-5}$) are given in the upper panel. The absolute TB and EB power spectra from isotropic rotation ($A_{CB} = 10^{-5}$) are shown in the lower panel.

anisotropic rotation field with $A_{CB} = 10^{-5}$, respectively. As a comparison, we also show the contributions from primordial tensor mode with $r = 0.004$ where r is the tensor-to-scalar ratio, and the contribution from CMB lensing. One can see that the B-mode signal from rotation fields can be larger than that from the primordial tensor mode at $\ell \gtrsim 150$, which suggests that, apart from searching for parity-violating physics, rotation field is also an important systematic when searching for primordial tensor mode. We also note that rotation field generally contributes less than CMB lensing to B-mode polarization; this suggests that the ability to "de-lens" the CMB will help tighten the constraints on cosmic birefringence. From Eq. (107) we can also see that both $\tilde{C}_\ell^{TB}$ and $\tilde{C}_\ell^{EB}$ become non-zero when $\bar{\alpha}$ is non-zero; this is consistent with the fact that an isotropic rotation field violates parity symmetry and induces odd-parity CMB power spectra (see the lower panel of Fig. 15 for example). In addition, when there is no anisotropic rotation (i.e., $C_L^{\alpha\alpha} = 0$), Eq. (107) reduces to the isotropic rotation formula as shown in, e.g., [84, 86].

4 Comparison with simulations:

To demonstrate the accuracy of `class_rot`, we compare the rotated CMB power spectra from `class_rot` with those from full-sky simulations. In particular, we first generate 100 realizations of un-rotated CMB maps in T, Q, and U based on a fiducial model given by the best-fit cosmology from Planck 2018 [111] with $l_{\rm max} = 6000$. Additionally we set a non-zero tensor-to-scalar ratio $r = 0.004$. Next we generate 100 realizations of a full-sky rotation map with $\bar{\alpha} = 0.1^\circ$ and $A_{CB} = 10^{-5}$, which are then used to rotate each realization of unrotated CMB maps. These full-sky simulations are generated using `pixell` [112] in rectangular pixelization and CAR projection with a resolution of 1 arcminute. We apply each rotation field to rotate one realization of simulated CMB maps in pixel space using Eq. (123) and then calculate its power spectra after the rotations. We repeat this procedure for each realization to get 100 sets of rotated CMB power spectra. In Fig. 16, we show the average of the 100 realizations of rotated power spectra in comparison to the corresponding theory spectrum obtained from `class_rot`. One can clearly see that the output of `class_rot` is in an

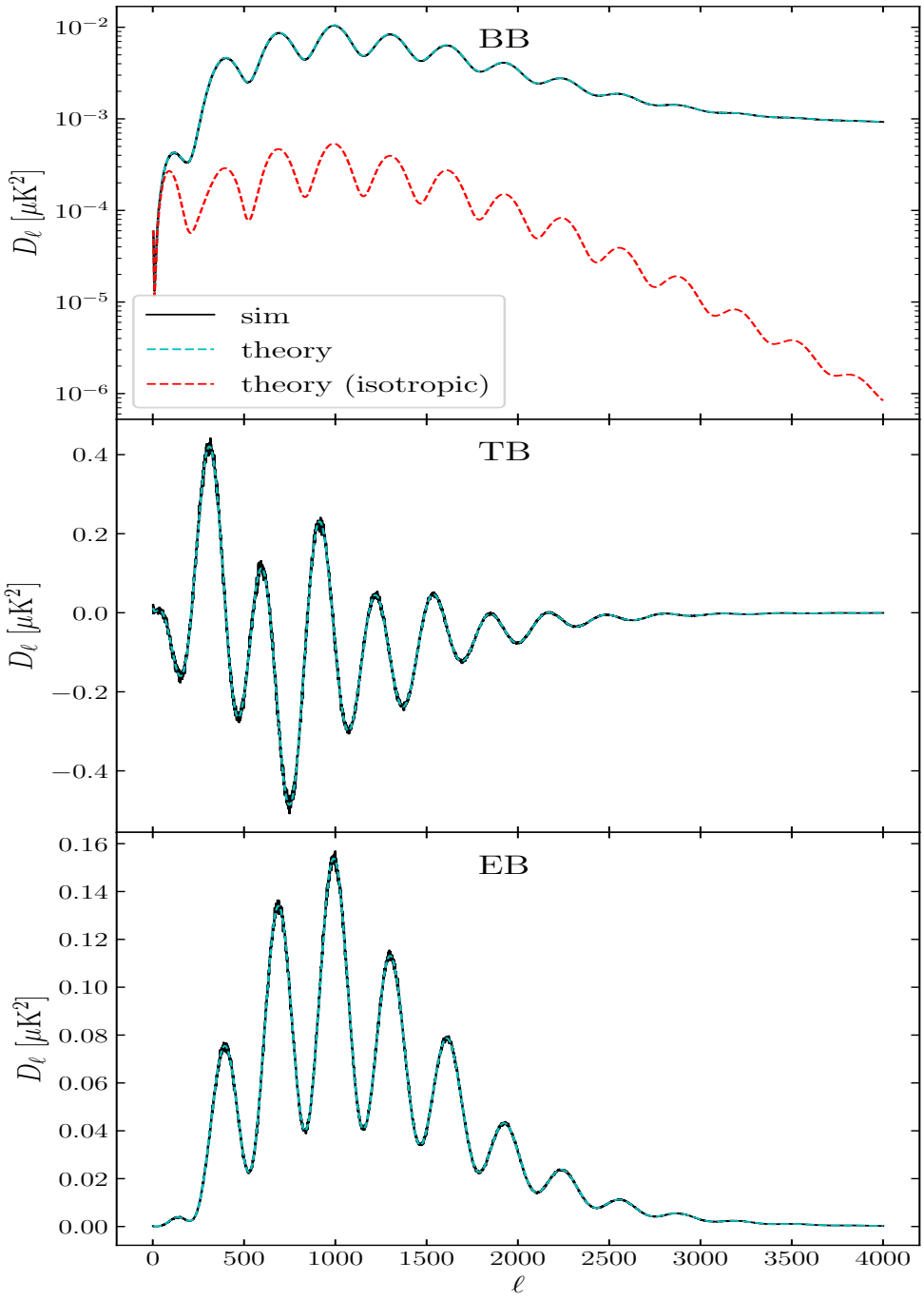

Figure 16: Comparisons of rotated CMB BB, TB, and EB power spectra between simulation and theory. The theory curves are calculated by `class_rot` and shown as cyan dashed lines; the power spectra from simulations are shown as black solid lines. The parameters are chosen as: $r = 0.004$, $\bar{\alpha} = 0.1°$, and $A_{CB} = 10^{-5}$. We also show the theory curve with only isotropic rotation in red dashed line. It only shows up in the upper panel (BB) because anisotropic rotation has no effect on TB and EB spectra.

excellent agreement with simulations. For C_ℓ^{BB} we estimate an error of $\lesssim 1\%$ at $\ell \lesssim 4000$; the accuracy noticeably degrades at larger ℓ likely due to a combination of pixel effect, numerical precision, and the smallness of the signal of interests. Both C_ℓ^{TE} and C_ℓ^{EB} from `class_rot` agree with the simulations within the expected cosmic variance of the averaged power spectra up to $\ell = 6000$, which is the highest multipole we have tested. Note that in the upper panel of Fig. 16, we also show the rotated CMB BB power spectrum with no anisotropic birefringence, which suggests that, with our chosen parameters, the contribution from anisotropic birefringence dominates the rotated BB power spectrum.

5 The software package

Here we describe briefly the implementation of `class_rot`, and give usage examples of its Python interface.

Code implementation: In `class_rot`, the calculations described in Sec. 3 are implemented as a new module to `class`, contained in `rotation.c` Internally, this `rotation` module takes the power spectra calculated from the `harmonic` module as inputs, by doing so we have implicitly neglected the effect of CMB lensing when calculating the rotated power spectrum. This assumption significantly simplifies our code implementation and will only lead to sub-percent to percent level error due to the smallness of C_ℓ^{BB} relative to C_ℓ^{EE}; to incorporate the effect of CMB lensing in the `rotation` module will be the subject of future work.

The `rotation` module can be turned on by specifying `rotation = yes` in the parameter file, and it can take two additional parameters that specify the rotation field, `alpha` and `A_cb`, which correspond to $\bar{\alpha}$, in unit of degrees, and A_{CB}, in radians as defined in Eq. (100), respectively. The rest of the parameters are identical to those in `class`. Note that by using A_{CB} we implicitly assume that the rotation field follows a scale-invariant power spectrum – a choice of preference rather than necessity; other rotation power spectrum can be implemented by changing the `rotation_cl_aa_at_l` function defined in `rotation.c` . We leave the support for taking in a generic rotational power spectrum as input to a future work.

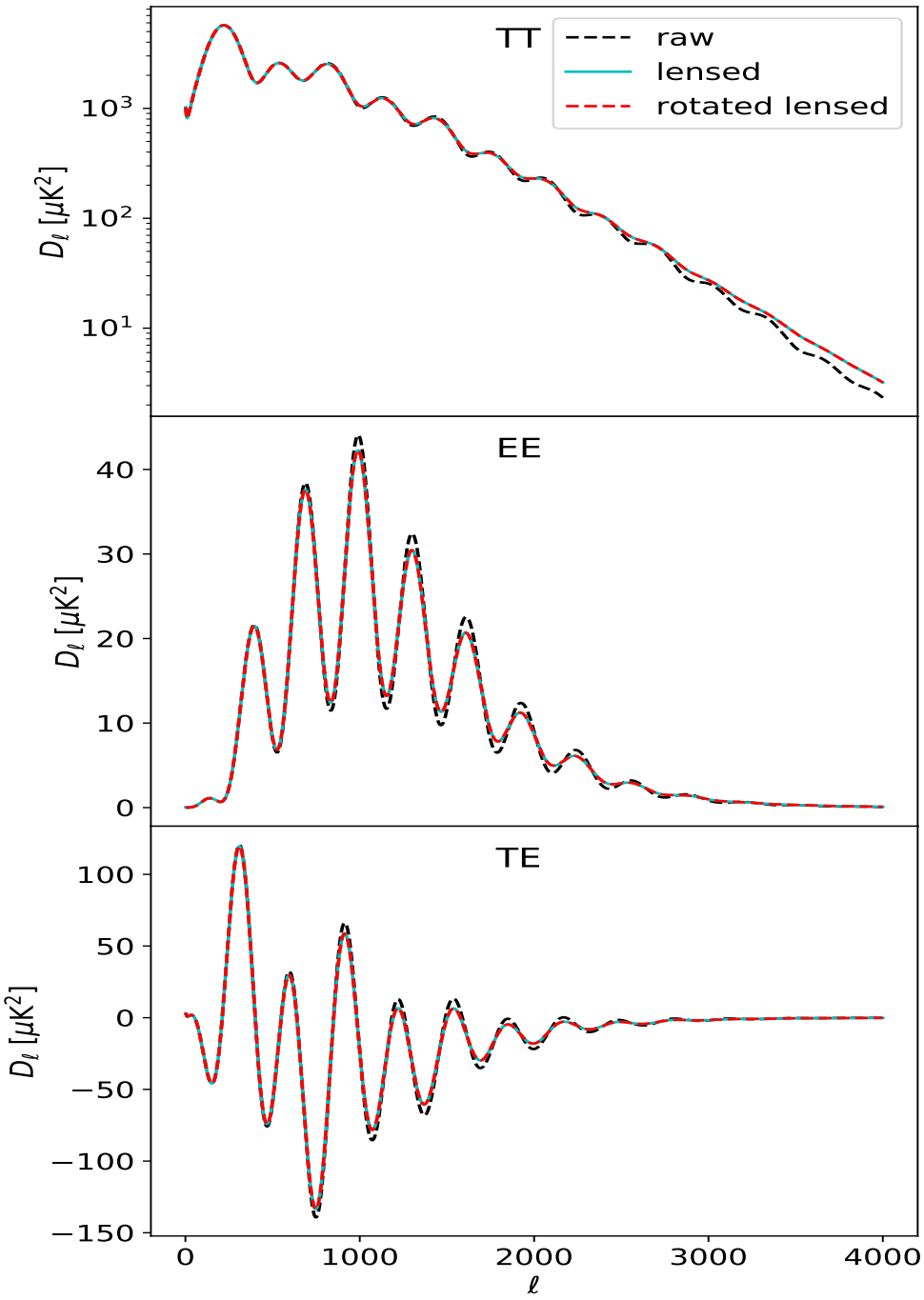

Figure 17: Rotated-lensed (red dashed lines), lensed (cyan solid lines) and raw (black dashed lines) CMB TT, EE and TE power spectra are shown. The parameters are chosen as: $r = 0$, $\bar{\alpha} = 0.1°$, and $A_{CB} = 10^{-5}$.

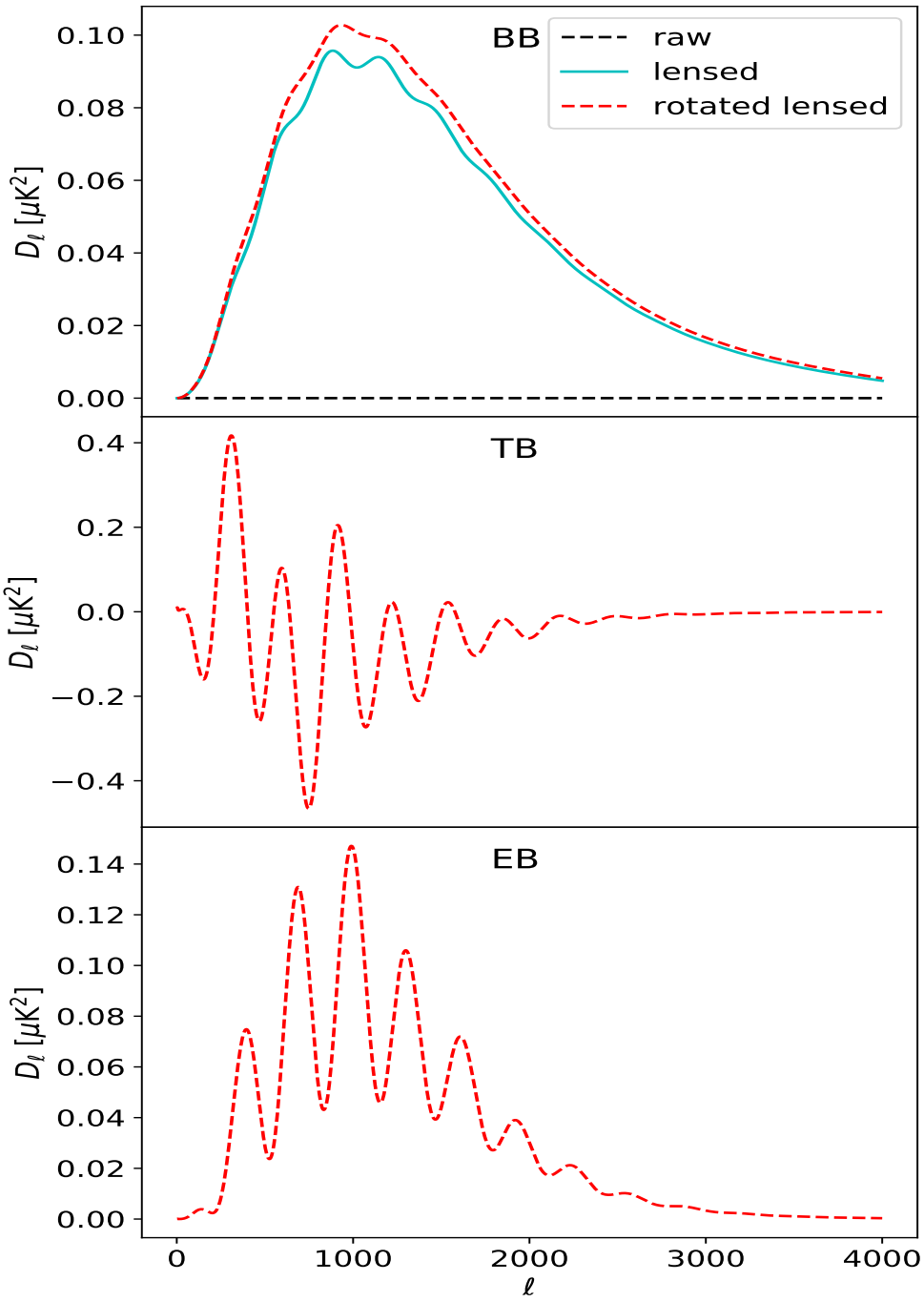

Figure 18: Rotated-lensed (red dashed lines), lensed (cyan solid lines) and raw (black dashed lines) CMB BB, TE and EB power spectra are shown. The parameters are chosen as: $r = 0$, $\bar{\alpha} = 0.1°$, and $A_{CB} = 10^{-5}$. In the first panel, the raw BB power spectrum is zero because there is no primordial B-mode. From the middle and bottom panels, we can see that the the parity-odd TB and EB power spectra are induced only by isotropic rotation.

The parameters can be specified in a parameter file and passed to the compiled `class` binary executable, in the same way as the original `class`. An example parameter file, `explanatory_ROT.ini` is also provided as part of `class_rot` to illustrate the use of parameters. Note that this parameter file is only needed when calling `class_rot` from the command-line interface using its compiled binary executable. We have also provided Python bindings to the functions in the rotation module allowing them to be called in the Python interface, and we show some usage example below.

Usage example: Here we give an example of how to calculate the rotated CMB power spectra using the Python interface of `class_rot`:

```
from classy import Class

params = {
  "output": "tCl,pCl,rCl",
  "l_max_scalars": 4000,
  "rotation": "yes",
  "alpha": 0.1,
  "A_cb": 1E-5,
}

cosmo = Class()
cosmo.set(params)
cosmo.compute(level=["rotation"])
cosmo.rotated_cl()
```

One can see that `class_rot` is meant to be used as a drop-in replacement to the original `class` as it is imported the same way and follows the same usage pattern. The parameters are specified in a Python dictionary, `param`, and passed to the `cosmo` object. Note that it is important to include `rCl` in the `output` option as it is required for computing the rotated power spectra. The option `rotation` turns on the rotation module when its value is `yes`; `alpha` and `A_cb` specify the rotation parameters as can be used in a parameter file. Also

note that when computing cosmological model with the function `cosmo.compute()`, one needs to include `level=["rotation"]` so that the rotation module and its dependencies are initialized properly. After running `cosmo.compute()`, the rotated power spectra can be obtained by the function call `cosmo.rotated_cl()`, in the form of a Python dictionary following the convention from `class`. This illustrates a basic usage of `class_rot`; we refer interested readers to the examples provided in the bundled Jupyter notebook in `class_rot` to find more detailed examples and explanations

Rotated-Lensed Power Spectra: Note that the power spectra in Fig. 16 do not include any lensing effect. `class` can also calculate the lensed-rotated CMB power spectra. Fig. 17 shows the rotated-lensed (red dashed lines), lensed (cyan solid lines) and raw (black dashed lines) CMB TT, EE and TE power spectra. Fig. 18 shows the rotated-lensed (red dashed lines), lensed (cyan solid lines) and raw (black dashed lines) CMB BB, TE and EB power spectra. The parameters are chosen as: $r = 0$, $\bar{\alpha} = 0.1°$, and $A_{CB} = 10^{-5}$. In the first panel, the raw BB power spectrum is zero because there is no primordial B-mode. From the middle and bottom panels, we can see that the the parity-odd TB and EB power spectra are induced only by isotropic rotation.

6 Discussion and conclusion

In this paper we present `class_rot`, a new publicly available modified `class` code, which calculates rotated CMB power spectra from cosmic birefringence using a non-perturbative method. `class_rot` supports both isotropic and anisotropic rotations, as can be specified by the isotropic rotation angle, $\bar{\alpha}$, and the amplitude of scale-invariant rotation power spectrum, A_{CB}, respectively. Hence, `class_rot` can be effectively used to search for cosmic birefringence signal that features a scale-invariant rotation power spectrum or an isotropic rotation in CMB polarization rotation, such as that from the coupling between axion-like particles and photons via Chern-Simons interaction. We leave the implementation of a more generic (i.e., not scale-invariant) rotation power spectrum in `class_rot` to a future work which will allow us to search for a broader range of rotation signal such as that caused by Faraday ro-

tation from primordial magnetic field, which, depending on its generation mechanism, may induce a rotation field that is not scale-invariant (see [113] for a review).

In this paper we have also briefly reviewed the non-perturbative calculation implemented in `class_rot`, which makes use of the angular correlation function of the rotation field and does not require the rotation to be perturbatively small. Hence the calculation in `class_rot` offers a broader range of applicability. We leave the implementation of a perturbative calculation as well as a detailed comparison between the non-perturbative and perturbative methods, in terms of both speed and accuracy, to a future work.

To demonstrate the accuracy of the code, we have compared the rotated CMB power spectra such as BB, TB, and EB obtained from `class_rot` to full-sky simulations and shown that they are in good agreements with $\lesssim 1\%$ error. The upcoming experiments are expected to constrain cosmic birefringence with much higher precision. For example, while the current best limits lie around $\mathcal{O}(10')$ for isotropic rotation [92, 94] and around $\mathcal{O}(10^{-6})$ for A_{CB} [15, 102], it has been forecasted that Simons Observatory [114] can improve the current limits by nearly an order of magnitude, achieving an uncertainty level of around $0.7'$ for isotropic rotation and around 10^{-7} for A_{CB} [33]. These limits will be further improved by the CMB-S4 experiment [115], reaching an uncertainty level of around $0.2'$ for isotropic rotation [50] and around 10^{-8} for A_{CB} [33]; this will allow for percent-level determinations of $\bar{\alpha}$ and A_{CB} should there be a cosmic birefringence signal at our current observational limit. In light of these future prospects, it is important to have a robust code that computes the effect of cosmic birefringence in power spectra with better than percent-level accuracy. Hence, `class_rot` can be a powerful tool for searches of cosmic birefringence signal in the future.

4.0 Impact of Anisotropic Birefringence on Measuring Cosmic Microwave Background Lensing

The content of this chapter is based on the manuscript published in Physical Review D [116]. The power spectrum of cosmic microwave background lensing is a powerful tool for constraining fundamental physics such as the sum of neutrino masses and the dark energy equation of state. Current lensing measurements primarily come from distortions to the microwave background temperature field, but the polarization lensing signal will dominate upcoming experiments with greater sensitivity. Cosmic birefringence refers to the rotation of the linear polarization direction of microwave photons propagating from the last scattering surface to us, which can be induced by parity-violating physics such as axion-like dark matter or primordial magnetic fields. We find that, for an upcoming CMB-S4-like experiment, if there exists the scale-invariant anisotropic birefringence with an amplitude corresponding to the current 95% upper bound, the measured lensing power spectrum could be biased by up to a factor of few at small scales, $L \gtrsim 1000$. We show that the bias scales linearly with the amplitude of the scale-invariant birefringence spectrum. The signal-to-noise of the contribution from anisotropic birefringence is larger than unity even if the birefringence amplitude decreases to $\sim 5\%$ of the current upper bound. Our results indicate that a measurement and characterization of the anisotropic birefringence is important for lensing analysis in future low-noise polarization experiments.

1 Introduction

CMB lensing refers to the effect that CMB photons get deflected by the matter distribution along their path from the last scattering surface to the observer. Such effect causes distortions in both temperature and polarization map of CMB acting as a displacement field. This displacement leads to the correlations across CMB temperature and polarization fluctuations on different angular scales. We therefore can use these correlations to reconstruct

the displacement field caused by lensing [19, 20]. Being able to measure the CMB lensing effect precisely allows one to understand the matter distribution of the universe, probe the evolution and geometry of the universe, and place constraints on cosmological parameters such as the amplitude of matter density fluctuations, σ_8, and the energy density of matter, ω_m, which CMB lensing is particularly sensitive to.

With improved sensitivity in measurements of the CMB temperature and polarization anisotropies, CMB lensing has been measured with increasing significance by various experiments including Planck [117, 118], ACT [119], BICEP [120], Polarbear [121, 122], and SPT [18, 123]. Although temperature-based reconstruction dominates the signal-to-noise in the current CMB lensing measurements, CMB polarization field is expected to provide higher signal-to-noise in upcoming surveys such as CMB-S4 [124].

Lensing reconstruction with CMB polarization is much less affected by various contaminants such as the thermal and kinematic Sunyaev–Zeldovich (tSZ, kSZ) effects, which may significantly bias the temperature-based lensing reconstruction [7, 38] at the arcminute scale. However, polarization-based lensing reconstruction can be biased by effects such as instrumental systematics [125, 126]. One effect paid less attention is a cosmic birefringence, which refers to a rotation of CMB linear polarization plane caused by some parity-violating physics such as the primordial magnetic fields or axion-like particles; in the latter case cosmic birefringence can be both isotropic and anisotropic. Several recent analyses of Planck polarization data find a tantalizing hint of the isotropic cosmic birefringence [127, 128, 129]. Cosmic birefringence therefore have gained growing interest in the context of cosmology (for review see e.g. [130]). Anticipating such a discovery, multiple works have explored the potential of future CMB experiments to, e.g., constrain the mass of axion-like particles [131, 132, 133, 134] and models which produce both isotropic and anisotropic cosmic birefringence [88, 135, 136, 137].

It has been previously noted that, up to the leading order, an anisotropic rotation field induced by cosmic birefringence does not bias the reconstructed lensing field, thanks to the orthogonality between the lensing and rotation response in the polarization field [138]. However, based on theoretical models of cosmic birefringence, we argue that the anisotropic rotation field which contributes to higher order statistics may potentially bias the recon-

structed lensing power spectrum, a pathway which has not been examined in details previously. Therefore, in this paper we aim to investigate whether such a bias may occur with a scale-invariant rotation field.

The paper is structured as follows. In Sec. 2 we review the basis of CMB lensing and cosmic birefringence. In Sec. 3 we review CMB lensing reconstruction on full-sky using EB estimator and explain the motivation of investigating the bias to reconstructed CMB lensing power spectrum. We show the simulation procedures and the results in Sec. 4. We discuss the results in Sec. 5 and conclude in Sec. 6.

2 Lensed and rotated CMB power spectra

Both CMB lensing and anisotropic cosmic birefringence affect CMB polarization field in a similar way. In this section we first give an overview of their effects on the CMB polarization field in 2.1, followed by brief reviews of CMB lensing and cosmic birefringence in 2.2 and 2.3, respectively. We then make some summary notes on in 2.4.

2.1 Overview

Linear polarization of CMB can be described by the Stokes parameters $Q(\hat{\boldsymbol{n}})$ and $U(\hat{\boldsymbol{n}})$, measured by a set of local orthogonal polarizers, with $\hat{\boldsymbol{n}}$ an angular coordinate on the sky. Q and U can be further decomposed using spin-weighted spherical harmonics [11] to obtain rotation-invariant quantities, E and B, as [12, 13]

$$E_{\ell m} \pm iB_{\ell m} = -\int d^2\hat{\boldsymbol{n}}\ {}_{\pm2}Y^*_{\ell m}(Q \pm iU)(\hat{\boldsymbol{n}}), \tag{108}$$

with $E_{\ell m}$ and $B_{\ell m}$ the multipole moments of E-mode and B-mode polarization, respectively. Their power spectra are defined as

$$\begin{aligned}
\langle E_{\ell m} E^*_{\ell' m'} \rangle &= \delta_{\ell\ell'}\delta_{mm'} C_\ell^{\mathrm{EE}} \\
\langle B_{\ell m} B^*_{\ell' m'} \rangle &= \delta_{\ell\ell'}\delta_{mm'} C_\ell^{\mathrm{BB}} \\
\langle E_{\ell m} B^*_{\ell' m'} \rangle &= \delta_{\ell\ell'}\delta_{mm'} C_\ell^{\mathrm{EB}},
\end{aligned} \tag{109}$$

where the $\langle ... \rangle$ is taken over different CMB realizations. One sees that the primary CMB polarization fields has no off-diagonal covariance.

The effects of both CMB lensing and cosmic birefringence can be interpreted as small perturbations added to the primary CMB field, effected by the lensing potential, $\phi(\hat{\boldsymbol{n}})$, for CMB lensing, and a rotation field, $\alpha(\hat{\boldsymbol{n}})$, for cosmic birefringence, respectively. In the presence of both CMB lensing and cosmic birefringence, the CMB polarization fields can be described as

$$\tilde{E}'_{\ell m} = E_{\ell m} + \delta\tilde{E}_{\ell m} + \delta E'_{\ell m} + \mathcal{O}(\phi^{n_1}\alpha^{n_2}), \tag{110}$$

$$\tilde{B}'_{\ell m} = \delta\tilde{B}_{\ell m} + \delta B'_{\ell m} + \mathcal{O}(\phi^{n_1}\alpha^{n_2}), \tag{111}$$

where $\delta\tilde{E}_{\ell m}$, $\delta\tilde{B}_{\ell m}$ denote the first order perturbation from CMB lensing, $\delta E'_{\ell m}$, $\delta B'_{\ell m}$ denote that from the rotation field[a], and $\mathcal{O}(\phi^{n_1}\alpha^{n_2})$, with $n_1 + n_2 > 1$, represents the high-order terms which mix the lensing and rotation effects. In the subsequent subsections we will discuss each of the terms in details.

2.2 CMB lensing

CMB lensing distortion occurs when photons travel across gravitational potentials and measures the integrated mass distribution along the trajectories of photons (for review see e.g. [16]). Lensing distortion results in an effective displacement field, $\boldsymbol{d}(\hat{\boldsymbol{n}})$, acting on the primary CMB fields,

$$\begin{aligned} \tilde{T}(\hat{\boldsymbol{n}}) &= T(\hat{\boldsymbol{n}} + \boldsymbol{d}(\hat{\boldsymbol{n}})), \\ (\tilde{Q} \pm i\tilde{U})(\hat{\boldsymbol{n}}) &= (Q \pm iU)(\hat{\boldsymbol{n}} + \boldsymbol{d}(\hat{\boldsymbol{n}})). \end{aligned} \tag{112}$$

Under Born's approximation and the assumption that all CMB photons come from the last scattering surface and that non-linear effect is negligible, the displacement field, $\boldsymbol{d}(\hat{\boldsymbol{n}})$, can be expressed as a pure gradient

$$\boldsymbol{d}(\hat{\boldsymbol{n}}) = \nabla\phi(\hat{\boldsymbol{n}}), \tag{113}$$

[a]Note that we will follow this notational convention, denoting rotation induced quantities with prime and lensing-induced quantities with a tilde, throughout this paper.

with $\phi(\hat{\boldsymbol{n}})$ the lensing potential field, given by

$$\phi(\hat{\boldsymbol{n}}) = -2\int_0^{\chi_*} d\chi \frac{\chi_* - \chi}{\chi_*\chi}\Psi(\chi\hat{\boldsymbol{n}}, \eta_0 - \chi) \tag{114}$$

in a flat universe under the same assumptions, with χ_* the conformal distance to the last scattering surface, η_0 the conformal time today, and Ψ the (Weyl) gravitational potential.

One can similarly decompose the lensing potential field with spherical harmonics as

$$\phi(\hat{\mathbf{n}}) = \sum_{LM} \phi_{LM} Y_{LM}(\hat{\mathbf{n}}), \tag{115}$$

with the multipole moments ϕ_{LM} related to its power spectrum as

$$\langle \phi_{LM}\phi^*_{L'M'}\rangle = \delta_{LL'}\delta_{MM'}C_L^{\phi\phi}. \tag{116}$$

Using Limber approximations, the power spectrum, $C_L^{\phi\phi}$, can be expressed analytically as

$$C_L^{\phi\phi} \approx \frac{8\pi^2}{L^3}\int_0^{\chi_*} \chi d\chi \left(\frac{\chi_* - \chi}{\chi_*\chi}\right)^2 P_\Psi\left(\frac{L}{\chi}; \eta_0 - \chi\right), \tag{117}$$

with $P_\Psi(k;\eta)$ the power spectrum of the gravitational potential, which is intimately connected to the matter power spectrum, $P_m(k;\eta)$, as

$$P_\Psi(k;\eta) = \frac{9\Omega_m^2(\eta)H^4(\eta)}{8\pi^2}\frac{P_m(k;\eta)}{k}, \tag{118}$$

with $\Omega_m(\eta)$ the fractional matter energy density, and $H(\eta)$ the Hubble parameters at conformal time η. Hence, CMB lensing encodes rich information of matter distribution, especially at late-time (as the integrand in Eq. (117) peaks at $z \sim 2$), and measurements of CMB lensing is therefore a powerful tool to constrain cosmological parameters such as the matter fluctuation amplitude σ_8, the matter density Ω_m, the spatial curvature of the universe Ω_k, the sum of neutrino masses $\sum m_\nu$, and the dark energy equation of state w, as previously demonstrated in, e.g., [17, 18].

A promising way to measure CMB lensing is through its effect on CMB polarization field [19, 20]. Following from Eq. (112), CMB lensing leads to perturbations in CMB E-mode and B-mode polarization fields, given by

$$\delta\tilde{E}_{\ell m} = \sum_{LM}\sum_{\ell' m'}(-1)^m \phi_{LM} \begin{pmatrix} \ell & L & \ell' \\ -m & M & m' \end{pmatrix}, \times {}_2F^{\phi}_{\ell L\ell'}\epsilon_{\ell L\ell'}E_{\ell' m'} \tag{119}$$

and

$$\delta\tilde{B}_{\ell m} = \sum_{LM}\sum_{\ell' m'}(-1)^m \phi_{LM} \begin{pmatrix} \ell & L & \ell' \\ -m & M & m' \end{pmatrix} \times {}_2F^{\phi}_{\ell L\ell'}\beta_{\ell L\ell'}E_{\ell' m'}, \tag{120}$$

in the leading order in ϕ, where $\epsilon_{\ell L\ell'}$ and $\beta_{\ell L\ell'}$ are parity terms defined as

$$\begin{aligned} \epsilon_{\ell L\ell'} &\equiv \frac{1+(-1)^{\ell+L+\ell'}}{2}, \\ \beta_{\ell L\ell'} &\equiv \frac{1-(-1)^{\ell+L+\ell'}}{2i}, \end{aligned} \tag{121}$$

and the function ${}_2F^{\phi}_{\ell L\ell'}$ defined as

$$\begin{aligned} {}_2F^{\phi}_{\ell L\ell'} \equiv & \left[-\ell\left(\ell+1\right)+L(L+1)+\ell'\left(\ell'+1\right)\right] \\ & \times\sqrt{\frac{\left(2\ell+1\right)\left(2L+1\right)\left(2\ell'+1\right)}{16\pi}} \begin{pmatrix} \ell & L & \ell' \\ 2 & 0 & -2 \end{pmatrix}. \end{aligned} \tag{122}$$

These perturbations to the CMB polarization fields introduces off-diagonal covariance in and between E-mode and B-mode polarization fields and therefore allows one to measure the lensing potential by optimally weighting quadratic combinations of the CMB polarization fields [20]. In the next part we will see that rotations to the CMB polarization field has similar effects.

2.3 Cosmic birefringence

In addition to lensing distortion, CMB polarization field may also undergo rotations as they propagate from the last scattering surface to us. This phenomenon is called cosmic birefringence. Cosmic birefringence can be caused by parity-violating physics in the early universe, such as axion-like particles coupling to photons through Chern-Simons interaction [23, 24, 25], more general Lorentz-violating physics beyond the Standard Model [26], and primordial magnetic fields through Faraday rotation which is frequency-dependent [27, 28, 139, 140, 141, 142].

Cosmic birefringence leads to a rotation of the linear polarization field of CMB, which can be expressed as

$$(Q' \pm iU')(\hat{\boldsymbol{n}}) = e^{\pm 2i\alpha(\hat{\boldsymbol{n}})}(Q \pm iU)(\hat{\boldsymbol{n}}), \tag{123}$$

with $\alpha(\hat{\boldsymbol{n}})$ a rotation field caused by cosmic birefringence. We use prime to represent the rotated quantities.

As a specific example, we can consider a scenario in which cosmic birefringence is induced by a Chern-Simons-type interaction of photons and axion-like particles in the early universe with a Lagrangian given by

$$\mathcal{L}_{cs} = \frac{g_{a\gamma} a}{4} F^{\mu\nu} \tilde{F}_{\mu\nu}, \tag{124}$$

where $g_{a\gamma}$ is a dimensionless coupling constant, a is the axion field, M is its mass scale, and $F^{\mu\nu}$ is the electromagnetic tensor with $\tilde{F}_{\mu\nu}$ being its dual. This term modifies the Euler-Lagrange equations for electromagnetic field and induces a rotation in the polarization direction of a photon if a varies along its propagation path [105, 106, 107], with the rotation angle given by

$$\alpha(\hat{\boldsymbol{n}}) = \frac{g_{a\gamma}}{2} \Delta a, \tag{125}$$

where Δa is the change of a along the photon path from the last scattering surface to us.

A generic rotation field can be separated into an isotropic and an anisotropic part as

$$\alpha(\hat{\boldsymbol{n}}) = \bar{\alpha} + \delta\alpha(\hat{\boldsymbol{n}}), \tag{126}$$

where $\bar{\alpha}$ is the isotropic part, and the $\delta\alpha(\hat{\boldsymbol{n}})$ is the anisotropic part with a zero mean

$$\langle \delta\alpha(\hat{\boldsymbol{n}}) \rangle = 0. \tag{127}$$

For example, some quintessence models predict both isotropic and anisotropic cosmic birefringence [29], while some massless scalar fields do not necessarily induce isotropic cosmic birefringence [97].

The isotropic cosmic birefringence violates parity symmetry and induces odd-parity CMB TB and EB power spectra, but the isotropic birefringence itself does not produce the correlations between CMB polarization fields at different angular scales.

In this paper we choose to focus the anisotropic cosmic birefringence, i.e., $\bar{\alpha} = 0$, as it features more similarity to CMB lensing as both are anisotropic. In what follows we will always assume that the rotation field, α, shown is purely anisotropic. Similar to Eq. (115), we can decompose the rotation field into multipole moments using spherical harmonics as

$$\alpha(\hat{\mathbf{n}}) = \sum_{LM} \alpha_{LM} Y_{LM}(\hat{\mathbf{n}}), \tag{128}$$

and the rotation field power spectrum is given by

$$\langle \alpha_{LM} \alpha^*_{L'M'} \rangle = \delta_{LL'} \delta_{MM'} C_L^{\alpha\alpha}. \tag{129}$$

Anisotropies in the rotation field can be a result of inhomogeneities in the axion field. If axion field is seeded during inflation, it leads to a Gaussian random rotation field with a nearly scale-invariant spectrum at large scales ($L \lesssim 100$), with an amplitude connected to the inflationary Hubble parameter $H_{\rm I}$,

$$\frac{L(L+1)C_L^{\alpha\alpha}}{2\pi} = \left(\frac{H_{\rm I} g_{a\gamma}}{4\pi}\right)^2 \equiv A_{\rm CB}, \tag{130}$$

where we defined a dimensionless parameter $A_{\rm CB}$ to denote the amplitude of the scale-invariant rotation power spectrum. The current constraint of the scale-invariant rotation power spectrum is given by ACTPol [15] and SPTPol [32] corresponding to the 2σ upper bound on the amplitude[b] $A_{\rm CB} \leq 10^{-5}$. The expected constraints of $A_{\rm CB}$ are at the level of 10^{-7} for the next-generation ground-based CMB experiments [143, 144, 34]. In this paper we focus only on scale-invariant rotation field for conceptual simplicity, but the methodology is generally applicable to rotation field with any power spectrum; we expect the conclusion

[b] Note that A_{CB} defined in this paper is 10^{-4} times of that in [15] and [32].

from other rotational power spectrum to be similar, but we leave a detailed analysis on such cases to a future work.

Similar to CMB lensing in Eq. (119), rotation field leads to perturbations in the CMB E-mode and B-mode polarization field, given by [138, 31]

$$\delta E'_{\ell m} = -2 \sum_{LM} \sum_{\ell' m'} (-1)^m \alpha_{LM} \begin{pmatrix} \ell & L & \ell' \\ -m & M & m' \end{pmatrix} \times {}_2F^{\alpha}_{\ell L \ell'} \beta_{\ell L \ell'} E_{\ell' m'}, \tag{131}$$

$$\delta B'_{\ell m} = 2 \sum_{LM} \sum_{\ell' m'} (-1)^m \alpha_{LM} \begin{pmatrix} \ell & L & \ell' \\ -m & M & m' \end{pmatrix} \times {}_2F^{\alpha}_{\ell L \ell'} \epsilon_{\ell L \ell'} E_{\ell' m'}, \tag{132}$$

to the leading order of α in a power series expansion of Eq. (123)[c], where $\beta_{\ell L \ell'}$ and $\epsilon_{\ell L \ell'}$ are defined in Eq. (121), and ${}_2F^{\alpha}_{\ell L \ell'}$ is defined as

$${}_2F^{\alpha}_{\ell L \ell'} = \sqrt{\frac{(2\ell+1)(2L+1)(2\ell'+1)}{4\pi}} \begin{pmatrix} \ell & L & \ell' \\ 2 & 0 & -2 \end{pmatrix}. \tag{133}$$

Note that the parity indicators in Eq. (131) and Eq. (132) are the opposite to the ones in Eq. (119) and Eq. (120), i.e., $\delta \tilde{E}$ and $\delta B'_{\ell m}$ are only non-zero when $\ell + L + \ell'$ is even and $\delta \tilde{B}$ and $\delta E'_{\ell m}$ are only non-zero when $\ell + L + \ell'$. In this sense, we say that CMB lensing and anisotropic cosmic birefringence are orthogonal at linear order [138].

[c] A non-perturbative treatment also exists; see [145] for an introduction.

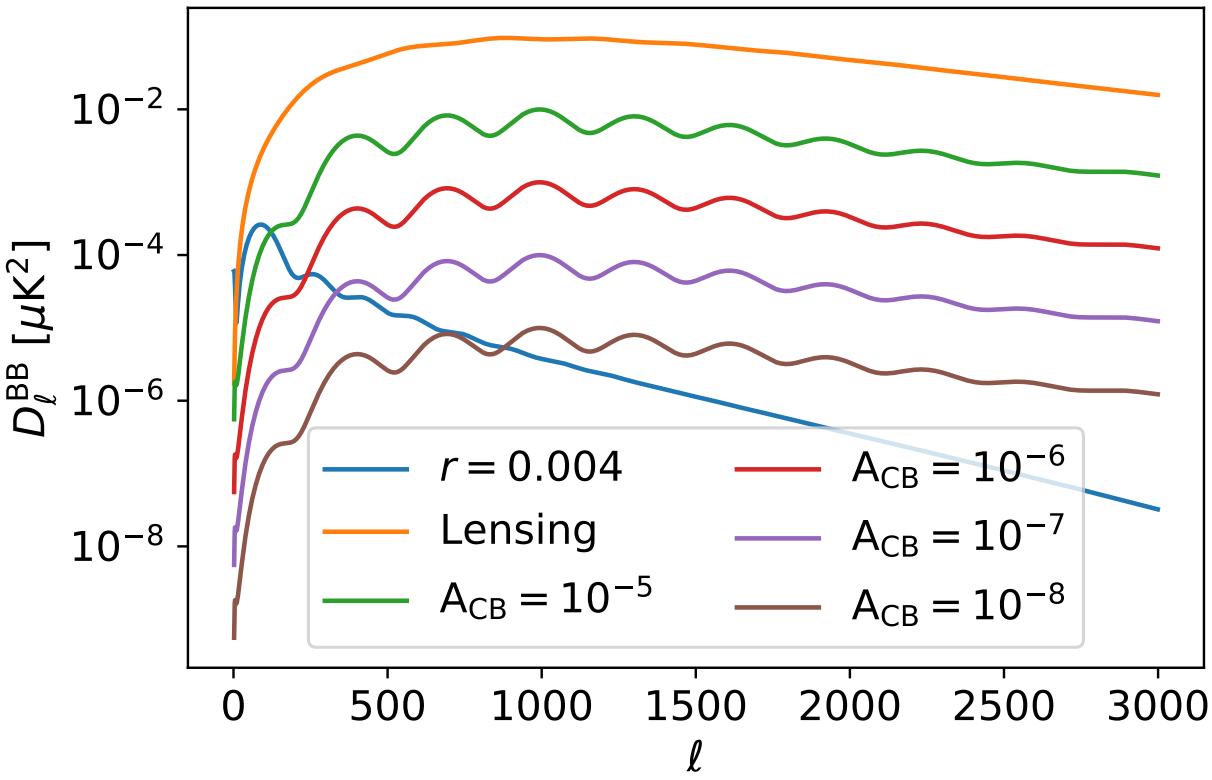

Figure 19: B-mode power spectrum contributions from a scale-invariant tensor mode ($r = 0.004$), gravitational lensing, and 1st-order scale-invariant anisotropic birefringence with different amplitudes ($A_{\mathrm{CB}} = 10^{-5}$, $A_{\mathrm{CB}} = 10^{-6}$, $A_{\mathrm{CB}} = 10^{-7}$ and $A_{\mathrm{CB}} = 10^{-8}$) are shown, where we define $D_\ell^{BB} \equiv \ell(\ell+1)C_\ell^{BB}/2\pi$. All the power spectra shown above are generated by `class_rot` [8].

2.4 Summary remarks

As we have seen, both CMB lensing and anisotropic cosmic birefringence lead to perturbations in the CMB E-mode and B-mode polarization field. To understand their relative contributions, one can measure the resulting B-mode power spectrum. In Fig. 19, we compare the B-mode power spectra from a scale-invariant primordial tensor mode with $r = 0.004$, gravitational lensing, and scale-invariant anisotropic rotation fields with different amplitudes ($A_{\rm CB} = 10^{-5}$, $A_{\rm CB} = 10^{-6}$, $A_{\rm CB} = 10^{-7}$, and $A_{\rm CB} = 10^{-8}$). One can see, similar to CMB lensing, anisotropic rotation contributes dominantly to small scale anisotropies in B-mode polarization, with a power spectrum generally orders of magnitude below the CMB lensing signal.

In addition to contributing to CMB polarization power spectra, both CMB lensing and rotation lead to off-diagonal covariance between E-mode and B-mode polarization fields [31],

$$\begin{aligned}\langle E_{\ell m}\delta\tilde{B}_{\ell' m'}\rangle_{\rm CMB} &= \sum_{LM}\begin{pmatrix}\ell & \ell' & L\\ m & m' & M\end{pmatrix} f^{\phi}_{\ell L\ell'}\phi^{*}_{LM},\\ \langle E_{\ell m}\delta B'_{\ell' m'}\rangle_{\rm CMB} &= \sum_{LM}\begin{pmatrix}\ell & \ell' & L\\ m & m' & M\end{pmatrix} f^{\alpha}_{\ell L\ell'}\alpha^{*}_{LM},\end{aligned} \tag{134}$$

for $\ell \neq \ell'$ and $m \neq -m'$. $f^{\phi}_{\ell L\ell'}$ and $f^{\alpha}_{\ell L\ell'}$ are weight functions for ϕ and α, given by

$$\begin{aligned} f^{\phi}_{\ell L\ell'} &= -\beta_{\ell L\ell'}\ {}_2F^{\phi}_{\ell L\ell'}C^{\rm EE}_{\ell},\\ f^{\alpha}_{\ell L\ell'} &= -2\epsilon_{\ell L\ell'}\ {}_2F^{\alpha}_{\ell L\ell'}C^{\rm EE}_{\ell}.\end{aligned} \tag{135}$$

We have defined $\langle ...\rangle_{\rm CMB}$ to be an ensemble average over different realisations of primary CMB, with a fixed realization of both ϕ and α. It then follows that

$$\begin{aligned}\langle \tilde{E}'_{\ell m}\tilde{B}'_{\ell' m'}\rangle_{\rm CMB} =& \sum_{LM}\begin{pmatrix}\ell & \ell' & L\\ m & m' & M\end{pmatrix} f^{\phi}_{\ell L\ell'}\phi^{*}_{LM}\\ &+\sum_{LM}\begin{pmatrix}\ell & \ell' & L\\ m & m' & M\end{pmatrix} f^{\alpha}_{\ell L\ell'}\alpha^{*}_{LM},\end{aligned} \tag{136}$$

for $\ell \neq \ell'$ and $m \neq -m'$. Eq. (136) shows that the off-diagonal covariance between E-mode and B-mode polarization is contributed by a summation of lensing and rotation contributions, to the leading order[d].

3 CMB lensing reconstruction bias due to rotation field

In this section, we introduce the CMB lensing reconstruction pipeline considered in this work. In particular, we focus on the EB estimator, as it is expected to be a dominant mode for lensing reconstruction in the upcoming experiments [20]. We then discuss the motivation and our methodology to estimate the bias to reconstructed lensing power spectrum through simulations.

3.1 Lensing reconstruction

Based on the off-diagonal covariance generated by CMB lensing in Eq. (136), the lensing potential can be reconstructed using a quadratic estimator approach, with the estimator for lensed E and B maps given by [20]

$$\hat{\phi}_{LM} = A_L \sum_{\ell m} \sum_{\ell' m'} (-1)^M \begin{pmatrix} \ell & \ell' & L \\ m & m' & -M \end{pmatrix} \times (f^{\phi}_{\ell L \ell'})^* \frac{\tilde{E}_{\ell m}}{\hat{C}^{\rm EE}_{\ell}} \frac{\tilde{B}_{\ell' m'}}{\hat{C}^{\rm BB}_{\ell'}}, \tag{137}$$

where A_L is a normalization factor ensuring $\hat{\phi}_{LM}$ is unbiased, given by

$$A_L = \left(\frac{1}{2L+1} \sum_{\ell \ell'} \frac{|f^{\phi}_{\ell L \ell'}|^2}{\hat{C}^{\rm EE}_{\ell} \hat{C}^{\rm BB}_{\ell'}} \right)^{-1}, \tag{138}$$

and $\hat{C}^{\rm EE}_{\ell}$ and $\hat{C}^{\rm BB}_{\ell}$ are the total observed EE and BB power spectra with noise power spectrum included. The quadratic estimator $\hat{\phi}_{LM}$ collects all the off-diagonal correlations of a CMB map realization and average them by a weight function $f^{\phi}_{\ell L \ell'}$.

[d] Note that Eq. (136) does not contradict with the fact that lensing and anisotropic rotation do not induce parity-odd power spectra, because the average is taken with fixed ϕ and α realizations; if, however, we also average over ϕ and α in Eq. (136), the resulting EB power spectrum will be zero.

Based on the reconstructed lensing potential, one can estimate its power spectrum which is directly relevant for cosmological parameter constraints. It can be estimated as [17]

$$\hat{C}_L^{\phi\phi} = C_L^{\hat{\phi}\hat{\phi}} - {}^{(\mathrm{RD})}N_L^{(0)} - N_L^{(1)} - N_L^{(\mathrm{MC})} - N_L^{(\mathrm{FG})}, \tag{139}$$

with $C_L^{\hat{\phi}\hat{\phi}}$ given by

$$C_L^{\hat{\phi}\hat{\phi}} = \frac{1}{2L+1}\sum_{M=-L}^{L}\left|\hat{\phi}_{LM}\right|^2. \tag{140}$$

The remaining terms in Eq. (140) are noise biases that need to be subtracted: ${}^{(\mathrm{RD})}N_L^{(0)}$ is the realization-dependent Gaussian noise (RDN0) [62] (the motivation to use this instead of the standard Gaussian noise, N_0, will be made clear later), $N_L^{(1)}$ represents the bias from those connected terms in CMB four-point function which contain the first-order lensing potential $C_L^{\phi\phi}$. $N_L^{(\mathrm{MC})}$ is the "Monte-Carlo"(MC) noise encapsulating biases not accounted for otherwise, such as higher-order reconstruction noise, estimated from MC simulations, and $N_L^{(\mathrm{FG})}$ is the modeled foreground bias from extragalactic and galactic foregrounds like galactic dust, galaxy clusters and cosmic infrared background.

3.2 Bias to $C_L^{\phi\phi}$ from rotation

Now consider a scenario in which we perform the aforementioned lensing reconstruction on a set of polarization maps which have been *unknowingly* rotated, how will this affect our estimated $C_L^{\phi\phi}$? To understand this, we can define an effective estimator,

$$\begin{aligned}\hat{\phi}'_{LM} = A_L \sum_{\ell m}\sum_{\ell' m'}(-1)^M \begin{pmatrix} \ell & \ell' & L \\ m & m' & -M \end{pmatrix} \\ \times (f^{\phi}_{\ell L \ell'})^* \frac{\tilde{E}'_{\ell m}}{\hat{C}_\ell^{\mathrm{EE}}}\frac{\tilde{B}'_{\ell' m'}}{\hat{C}_{\ell'}^{\mathrm{BB}}},\end{aligned} \tag{141}$$

which represents that we are *incorrectly* using the rotated-lensed quantities, $\tilde{E}'_{\ell m}$, $\tilde{B}'_{\ell m}$, in place of the lensed-only ones.

We first note that this effective estimator, $\hat{\phi}'_{LM}$, does not bias the reconstructed lensing potential, up to the leading order of ϕ and α (also see Appendix. B of [31] for a similar

discussion). This can be demonstrated by taking the ensemble average of $\hat{\phi}'$ over different CMB realizations,

$$\begin{aligned}\langle\hat{\phi}'_{LM}\rangle_{\rm CMB} =& A_L \sum_{\ell m}\sum_{\ell' m'}\sum_{L'M'}(-1)^M \\ &\times \begin{pmatrix} \ell & \ell' & L \\ m & m' & -M \end{pmatrix}\begin{pmatrix} \ell & \ell' & L' \\ m & m' & M' \end{pmatrix} \\ &\times \left((f^{\phi}_{\ell L\ell'})^* f^{\phi}_{\ell L'\ell'}\phi^*_{L'M'} + (f^{\phi}_{\ell L\ell'})^* f^{\alpha}_{\ell L'\ell'}\alpha^*_{L'M'}\right).\end{aligned} \tag{142}$$

Applying the orthogonality relation of wigner 3j symbols,

$$\sum_{mm'}\begin{pmatrix} \ell & \ell' & L \\ m & m' & -M \end{pmatrix}\begin{pmatrix} \ell & \ell' & L' \\ m & m' & M' \end{pmatrix} = \frac{1}{2L+1}\delta_{LL'}\delta_{M,-M'}, \tag{143}$$

and the orthogonality of the parity indicators

$$\epsilon_{\ell L\ell'}\beta_{\ell L\ell'} = 0, \tag{144}$$

we can see that the leading-order rotation contribution disappears due to parity, and we get

$$\begin{aligned}\langle\hat{\phi}'_{LM}\rangle_{\rm CMB} &= A_L \sum_{\ell\ell'}\frac{1}{2L+1}\frac{|f^{\phi}_{\ell L\ell'}|^2}{\hat{C}^{\rm EE}_{\ell}\hat{C}^{\rm BB}_{\ell'}}\phi_{LM} \\ &= \phi_{LM},\end{aligned} \tag{145}$$

which shows that our estimator for lensing potential, ϕ, remains unbiased.

However, we should emphasize that an unbiased ϕ does not necessarily imply an unbiased $C_L^{\phi\phi}$. Similar to the fact that $\langle x\rangle = 0$ does not imply $\langle x^2\rangle = 0$, the estimator, $C_L^{\hat{\phi}\hat{\phi}}$, contains quadratic terms in $\hat{\phi}$ and thus is not guaranteed to be unbiased. In addition, higher-order terms in Eq. (131) and Eq. (132) may also break the orthogonality between CMB lensing and anisotropic rotation and induce bias to $\hat{C}_L^{\phi\phi}$.

Based on Eq. (139), we define the bias from rotation to reconstructed CMB lensing power spectrum in average as

$$\Delta(\hat{C}_L^{\phi\phi})_{\rm rot} \equiv \langle\hat{C'}_L^{\phi\phi}\rangle - \langle\hat{C}_L^{\phi\phi}\rangle \tag{146}$$

where the subscript 'rot' denotes the bias is induced by rotation, $\langle ... \rangle$ represents the average over the reconstructed lensing power spectra, and $\hat{C'}_L^{\phi\phi}$ refers to applying the power spectrum estimator given in Eq. (139) to rotated-lensed CMB maps. Among the noise biases in Eq. (139), we assume that anisotropic rotation does not affect $N_L^{(1)}$, $N_L^{(\mathrm{MC})}$ and $N_L^{(\mathrm{FG})}$ on full-sky. RDN0, on the other hand, is calculated based on the observed CMB power spectrum and therefore will be affected by rotation as it changes the CMB polarization power spectra (as shown in Fig. 19). RDN0 is calculated based on both "data" and MC simulation, encapsulating all the disconnected terms in the CMB four-point correlation [62, 69]; consequently, when compared with a standard MC $\mathrm{N}_L^{(0)}$, RDN0 automatically mitigates the biases from small changes to the CMB covariance[e], such as that arising from rotation in the context of this paper.

We can then write Eq. (146) as

$$\begin{aligned}\Delta(\hat{C}_L^{\phi\phi})_{\mathrm{rot}} =& \langle C_L^{\hat{\phi}'\hat{\phi}'} \rangle - \langle C_L^{\hat{\phi}\hat{\phi}} \rangle \\ &-(\langle {}^{(\mathrm{RD})}\mathrm{N}_L^{\prime(0)} \rangle - \langle {}^{(\mathrm{RD})}\mathrm{N}_L^{(0)} \rangle),\end{aligned} \tag{147}$$

where $\langle \hat{C}_L^{\prime\phi\phi} \rangle$ and $\langle \hat{C}_L^{\phi\phi} \rangle$ represent the average over the two sets of reconstructed lensing potential power spectrum using rotated lensed and unrotated lensed CMB maps respectively, and $\langle {}^{(\mathrm{RD})}\mathrm{N}_L^{\prime(0)} \rangle$ and $\langle {}^{(\mathrm{RD})}\mathrm{N}_L^{(0)} \rangle$ represent the corresponding average RDN0. We will show the simulation of RDN0 in Sec. 4.

4 Simulation and results

In this section, we show our simulation steps and present our results. As discussed in Sec. 3, to estimate the bias $\Delta(\hat{C}_L^{\phi\phi})_{\mathrm{rot}}$ in Eq. (147), we need two sets of simulated CMB polarization maps: one set with both CMB lensing and rotation, and another set with CMB lensing only. The first set of simulations (including both lensing and rotation) is generated by rotating the lensed simulations in pixel space with a random realization of rotation field.

[e] The difference between ${}^{(\mathrm{RD})}\mathrm{N}_L^{(0)}$ and $\mathrm{N}_L^{(0)}$ has been introduced in [125].

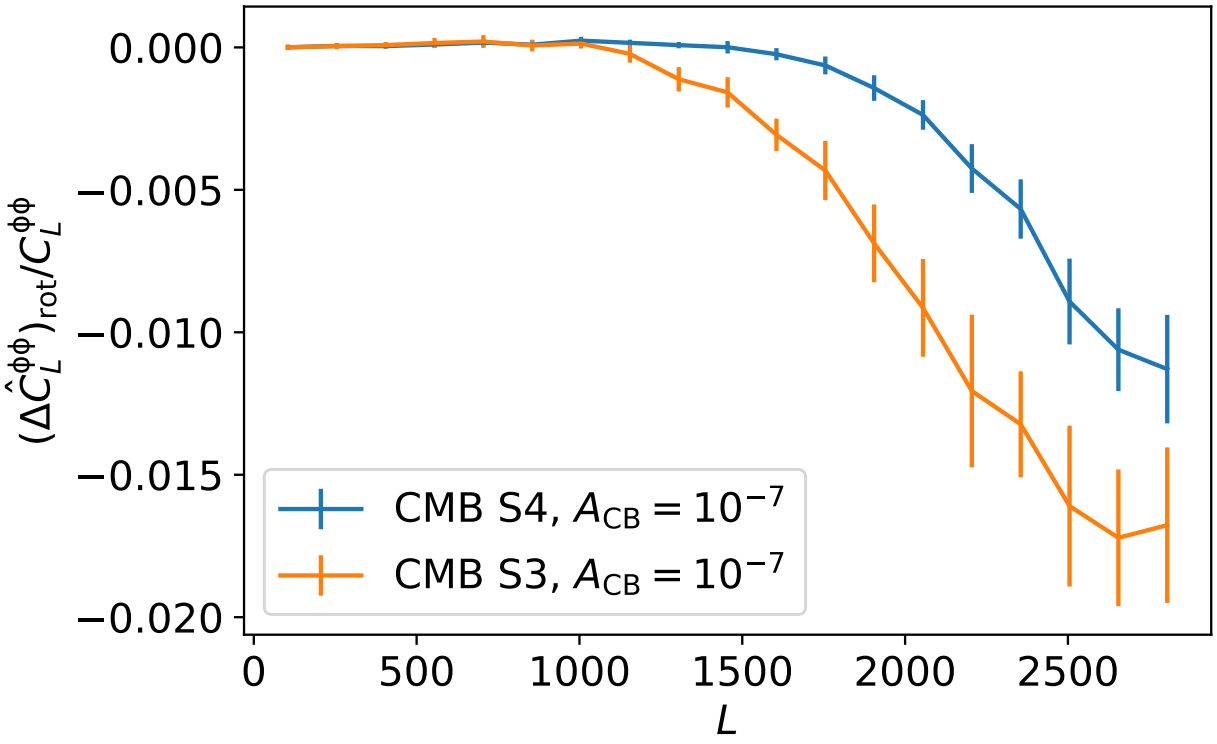

Figure 20: Comparing biases from different $A_{\rm CB}$ in a CMB-S4-like experiment. For visualization we have scaled both data and error bar by a factor of 10 and 0.1 for $A_{\rm CB} = 10^{-8}$ and 10^{-6}, respectively. Similarly the horizontal displacements between the three data series are for visualization purpose only.

All simulations in this work are generated in CAR pixelization on the full sky using `pixell`[f] [112]. We then use `cmblensplus`[g] to perform the CMB lensing reconstruction on the full sky which avoids unnecessary complications due to partial sky coverage[h]. Below we summarize the details of our simulation steps:

1. We generate 10 realizations of lensed CMB polarization maps, $\{\tilde{X}(\hat{\boldsymbol{n}})\}$ ($X \in \{E, B\}$), based on fiducial power spectrum, $C_l^{XX}|_{\rm fid}$, given by the best-fit cosmology from Planck 2018 [111] where no polarization rotation is present.
2. We generate 10 Gaussian realizations of anisotropic rotation field, $\{\alpha(\hat{\boldsymbol{n}})\}$, assuming a scale-invariant power spectrum with $A_{\rm CB} = 10^{-7}$ as defined in Eq. (130).
3. We perform a pixel-wise polarization rotation on each $\tilde{X}(\hat{\boldsymbol{n}})$ with the rotation field, $\alpha(\hat{\boldsymbol{n}})$, and get a set of 10 rotated-lensed CMB polarization maps, denoted as $\{\tilde{X}'(\hat{\boldsymbol{n}})\}$.
4. We perform full-sky CMB lensing reconstruction using `cmblensplus` [146] on both sets of simulations, $\{\tilde{X}(\hat{\boldsymbol{n}})\}$ and $\{\tilde{X}'(\hat{\boldsymbol{n}})\}$, and obtain an average lensing power spectrum for each set of simulations, denoted as $\langle C_L^{\hat{\phi}\hat{\phi}}\rangle$ and $\langle C_L^{\hat{\phi}'\hat{\phi}'}\rangle$. In particular, we have restricted to multipoles between $\ell_{\rm min} = 30$ to $\ell_{\rm max} = 3000$ for lensing reconstruction, and for the total power spectra, $\hat{C}_\ell^{XX}$, we have also used the Knox formula [147]

$$\hat{C}_\ell^{XX} = C_\ell^{XX}|_{\rm fid} + N_\ell, \tag{148}$$

with the homogeneous detector noise power spectrum for polarization given by

$$N_\ell = \Delta_{\rm P}^2 e^{\ell(\ell+1)\theta^2_{\rm FWHM}/(8ln2)}, \tag{149}$$

where $\Delta_{\rm P}$ is the polarization noise level of the experiment and $\theta^2_{\rm FWHM}/(8\ln 2)$ is the full-width at half maximum (FWHM) of the beam in radians. Note that although experimental noises are modeled in the power spectrum level in $\hat{C}_l^{XX}$, Gaussian noises in the map do not affect the estimation of lensing bias but introduce additional scatter in the result, so we choose to not include it in our simulated maps.

[f] `https://github.com/simonsobs/pixell`
[g] `https://github.com/toshiyan/cmblensplus`
[h] There can be extra mean-field bias for cut-sky CMB lensing reconstruction [62].

5. Following [62, 69], we calculate RDN0 for each map in $\{\tilde{X}\}$ and $\{\tilde{X}'\}$ by making two additional set of lensed CMB simulations, $\{\tilde{X}^{S_1}\}$ and $\{\tilde{X}_i^{S_2}\}$, each containing 50 simulations. For a given map, $\tilde{X}(\hat{\boldsymbol{n}})$, we calculate its RDN0 as

$$\begin{aligned}{}^{(\mathrm{RD})}\mathrm{N}_L^{(0)} =&\langle C_L^{\hat{\phi}\hat{\phi}}[\tilde{E}\tilde{B}^{S_1}, \tilde{E}\tilde{B}^{S_1}] + C_L^{\hat{\phi}\hat{\phi}}[\tilde{E}^{S_1}\tilde{B}, \tilde{E}\tilde{B}^{S_1}] \\ &+ C_L^{\hat{\phi}\hat{\phi}}[\tilde{E}^{S_1}\tilde{B}, \tilde{E}^{S_1}\tilde{B}] + C_L^{\hat{\phi}\hat{\phi}}[\tilde{E}\tilde{B}^{S_1}, \tilde{E}^{S_1}\tilde{B}] \\ &- C_L^{\hat{\phi}\hat{\phi}}[\tilde{E}^{S_1}\tilde{B}^{S_2}, \tilde{E}^{S_1}\tilde{B}^{S_2}] \\ &- C_L^{\hat{\phi}\hat{\phi}}[\tilde{E}^{S_1}\tilde{B}^{S_2}, \tilde{E}^{S_2}\tilde{B}^{S_1}]\rangle_{S_1,S_2},\end{aligned} \tag{150}$$

and similarly we calculate RDN0 for a given rotated-lensed map $\tilde{X}'$ as

$$\begin{aligned}{}^{(\mathrm{RD})}\mathrm{N}_L^{\prime(0)} =&\langle C_L^{\hat{\phi}\hat{\phi}}[\tilde{E}'\tilde{B}^{S_1}, \tilde{E}'\tilde{B}^{S_1}] + C_L^{\hat{\phi}\hat{\phi}}[\tilde{E}^{S_1}\tilde{B}', \tilde{E}'\tilde{B}^{S_1}] \\ &+ C_L^{\hat{\phi}\hat{\phi}}[\tilde{E}^{S_1}\tilde{B}', \tilde{E}^{S_1}\tilde{B}'] + C_L^{\hat{\phi}\hat{\phi}}[\tilde{E}'\tilde{B}^{S_1}, \tilde{E}^{S_1}\tilde{B}'] \\ &- C_L^{\hat{\phi}\hat{\phi}}[\tilde{E}^{S_1}\tilde{B}^{S_2}, \tilde{E}^{S_1}\tilde{B}^{S_2}] \\ &- C_L^{\hat{\phi}\hat{\phi}}[\tilde{E}^{S_1}\tilde{B}^{S_2}, \tilde{E}^{S_2}\tilde{B}^{S_1}]\rangle_{S_1,S_2},\end{aligned} \tag{151}$$

where the combinations in [...] represent the input maps for lensing reconstruction, and $\langle ... \rangle_{S_1,S_2}$ refers to an average over the two sets of MC simulations (S_1, S_2) [i]. Using Eq. (150) and (151), we calculate RDN0 for each simulation in $\{\tilde{X}(\hat{\boldsymbol{n}})\}$ and $\{\tilde{X}'(\hat{\boldsymbol{n}})\}$ and calculate the average within each set of simulations, respectively, denoted as $\langle {}^{(\mathrm{RD})}\mathrm{N}_L^{(0)}\rangle$ and $\langle {}^{(\mathrm{RD})}\mathrm{N}_L^{\prime(0)}\rangle$.

6. We then estimate the lensing bias, $\Delta(\hat{C}_L^{\phi\phi})_{\mathrm{rot}}$ using Eq. (147), and calculate fractional bias defined as $\Delta(\hat{C}_L^{\phi\phi})_{\mathrm{rot}}/C_L^{\phi\phi}$, with $C_L^{\phi\phi}$ the power spectrum of the CMB lensing potential from the fiducial model.

7. We repeat the above procedures for two sets of experimental configurations: CMB-S3-like and CMB-S4-like. The experimental configurations including the noise level and beam size are list in Table 2.

[i] In practice, due to memory constraint, we split the set, S_1, further into two subsets, S_{11} and S_{12}, evenly; Similarly S_2 is split into S_{21} and S_{22}. The average over S_1 and S_2 is calculated by averaging over the combinations of $\{S_{11}, S_{21}\}$, $\{S_{11}, S_{22}\}$, $\{S_{12}, S_{21}\}$, and $\{S_{12}, S_{22}\}$.

Expt	Δ_T [μK$'$]	$\theta_{\rm FWHM}[']$
CMB-S3-like	7	1.4
CMB-S4-like	1	1.4

Table 2: Experiments configurations considered in this study.

In Fig. 20, we show the fractional bias, $\Delta(\hat{C}_L^{\phi\phi})_{\rm rot}/C_L^{\phi\phi}$, obtained from the pipeline described above for both CMB-S3-like and CMB-S4-like experiments, respectively. We find that a rotation field with $A_{\rm CB} = 10^{-7}$, which is well-below the current experimental constraint, is capable of introducing a percent-level bias to the reconstructed lensing power spectrum. The bias is most evident at small scales ($L \gtrsim 1000$), reaching up to 1.5% for CMB-S3-like experiments and slightly lower for CMB-S4-like experiments.

5 Discussion

To understand the observed bias, we compare the four-point correlation function contained in $C_L^{\hat{\phi}'\hat{\phi}'}$,

$$\langle \tilde{E}'_{\ell_1 m_1} \tilde{B}'_{\ell_2 m_2} \tilde{E}'_{\ell_3 m_3} \tilde{B}'_{\ell_4 m_4} \rangle, \tag{152}$$

to the four-point correlation function in $C_L^{\hat{\phi}\hat{\phi}}$,

$$\langle \tilde{E}_{\ell_1 m_1} \tilde{B}_{\ell_2 m_2} \tilde{E}_{\ell_3 m_3} \tilde{B}_{\ell_4 m_4} \rangle. \tag{153}$$

To the leading order, one of the dominant contributions to their difference is given by

$$\begin{aligned} &\langle E_{\ell_1 m_1} \delta B'_{\ell_2 m_2} E_{\ell_3 m_3} \delta B'_{\ell_4 m_4} \rangle \\ &\propto \langle E_{\ell_1 m_1} (E_{\ell'_2 m'_2} \alpha_{LM}) E_{\ell_3 m_3} (E_{\ell'_4 m'_4} \alpha_{L'M'}) \rangle, \end{aligned} \tag{154}$$

where we have applied Eq. (132) and used parentheses to indicate groupings of terms which will be useful later on. As we have assumed α to be a Gaussian random field, Eq. (154) can

be simplified using Wick theorem into products of two-point correlation functions that can be broadly classified into two classes: disconnected terms and connected terms.

An example of disconnected term can be expressed as

$$\langle E_{\ell_1 m_1}(E_{\ell'_2 m'_2}\alpha_{LM})E_{\ell_3 m_3}(E_{\ell'_4 m'_4}\alpha_{L'M'})\rangle, \tag{155}$$

where we have used Wick contraction notation to denote products of two-point correlation functions. This term is classified as a disconnected term of CMB four-point correlation function, because fields within the same "group", e.g., $E_{\ell'_2 m'_2}$ and α_{LM} (as indicated by the parentheses), follow the same contraction behaviour, i.e., contracting with a common group, $E_{\ell'_4 m'_4}$ and $\alpha_{L'M'}$. If, on the other hand, contraction behavior of fields in the same group is different, we classify the term as connected. For example, this term,

$$\langle E_{\ell_1 m_1}(E_{\ell'_2 m'_2}\alpha_{LM})E_{\ell_3 m_3}(E_{\ell'_4 m'_4}\alpha_{L'M'})\rangle, \tag{156}$$

is a connected term, and so is the term,

$$\langle E_{\ell_1 m_1}(E_{\ell'_2 m'_2}\alpha_{LM})E_{\ell_3 m_3}(E_{\ell'_4 m'_4}\alpha_{L'M'})\rangle. \tag{157}$$

In both cases $E_{\ell'_2 m'_2}$ and α_{LM} do not contract with a common group. The distinction of disconnected and connected terms is important because the RDN0 technique that we apply mitigates the leading-order biases in the disconnected terms of the four-point correlation, such as that in Eq. (155), but cannot mitigate biases in the connected terms. Hence we expect that a dominant contribution to the observed bias in Sec. 4 comes from the accumulated effect of all connected terms, such as Eq. (156) and (157).

Note that in the discussion above we have neglected the effect of higher-order terms, which mix lensing and rotation. Higher-order terms, on one hand, break the orthogonality between lensing and rotation, leading to bias in $\hat{\phi}$; they also contribute additional connected terms to $\hat{C}_l^{\phi\phi}$. In Fig. 21 we show the contributions from leading- and higher-order terms in power spectrum level, calculated using `class_rot`[j]. We find that higher-order terms (with $A_{\rm CB} = 10^{-7}$) generally contribute at a few percents level of that from the leading

[j] Higher-order contribution is estimated by subtracting leading-order lensing and rotation contributions from a non-perturbative calculation with both lensing and rotation, implemented in `class_rot`.

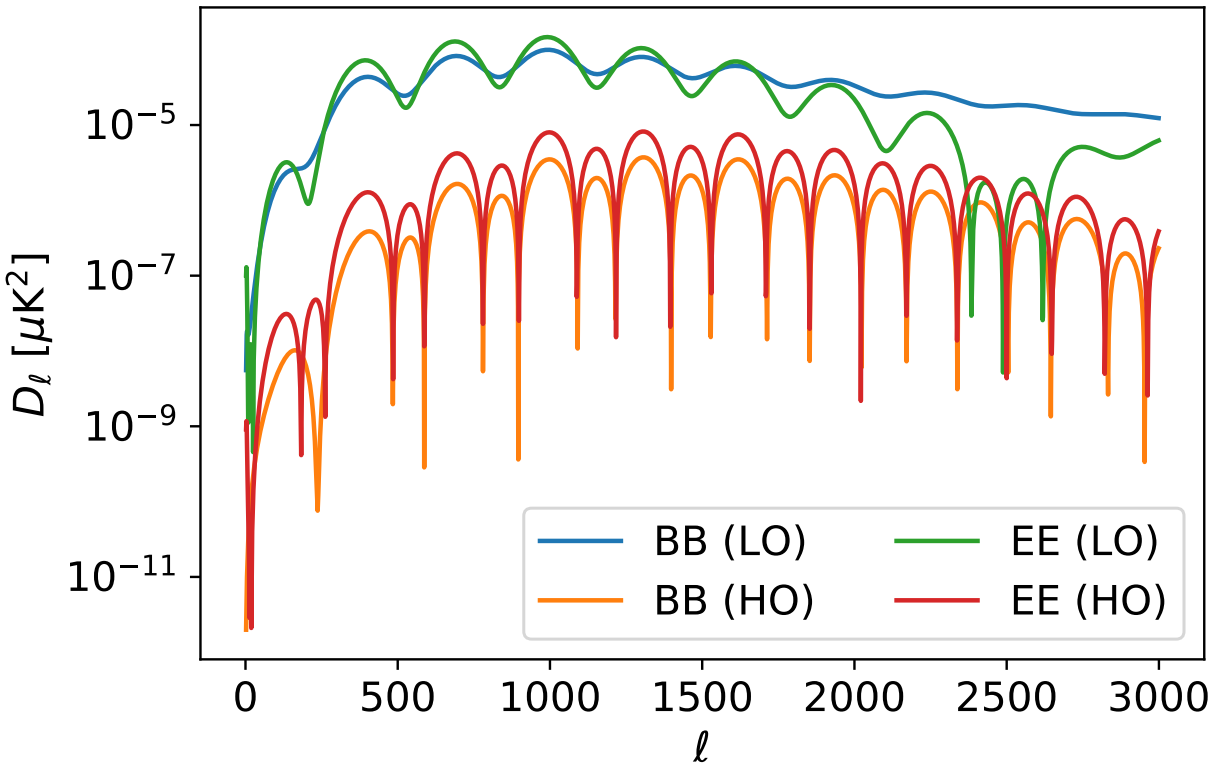

Figure 21: B-mode power spectrum contributions from the leading-order (LO) contribution and higher-order (HO) contribution of scale-invariant anisotropic cosmic birefringence with an amplitude of $A_{\rm CB} = 10^{-7}$. The former is about two order of magnitude larger than the latter. The power spectra shown here are generated by `class_rot` [8].

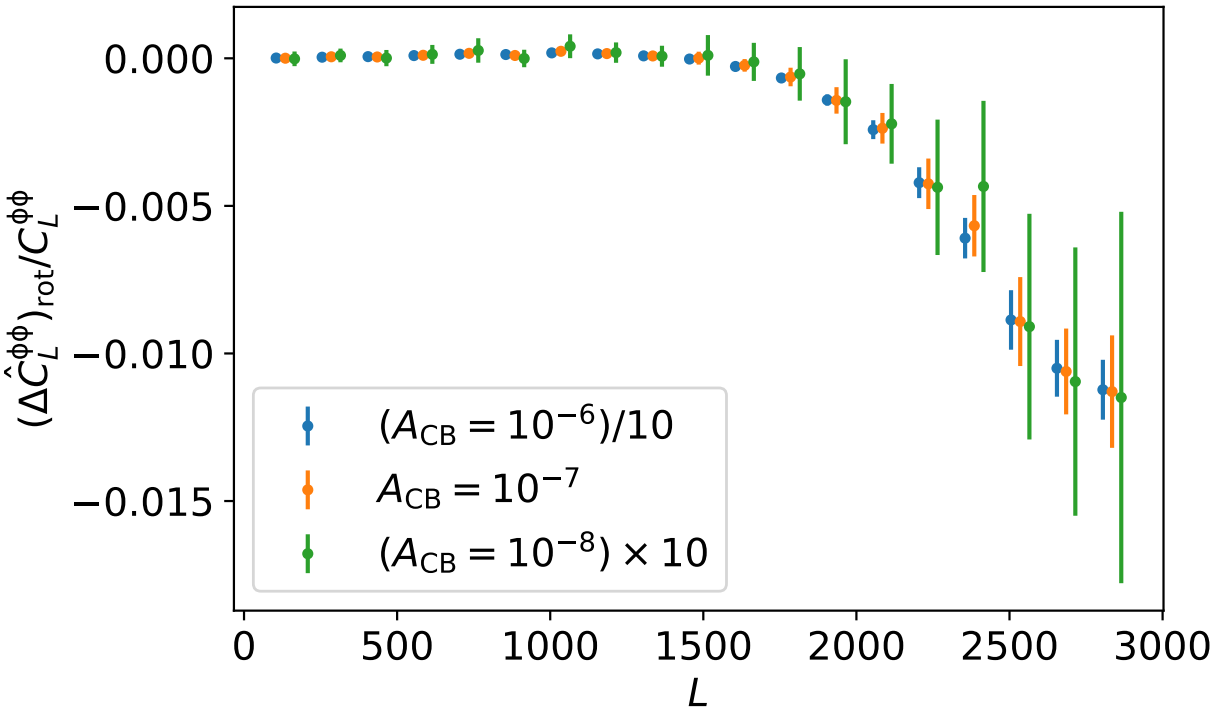

Figure 22: Compare biases from different $A_{\rm CB}$ in context of a CMB-S4-like experiment. For visualization we have scaled both data and error bar by a factor of 10 and 0.1 for $A_{\rm CB} = 10^{-8}$ and 10^{-6}, respectively. Similarly the horizontal displacements between the three data series are for visualization purpose only.

order. Therefore we expect higher-order terms to contribute at about 10% level of that from leading order in the map space and thus is a subdominant contribution to the observed bias.

If the contributions from connected terms, such as Eq. (156) and (157), are dominant and the higher-order terms are subdominant, we expect the size of the observed bias to scale linearly with $C_L^{\alpha\alpha}$ and thus linearly with $A_{\rm CB}$. To verify this, we repeat the steps in Sec. 4 for $A_{\rm CB} = 10^{-6}$ and 10^{-8}, respectively, and compare the resulting biases in Fig. 22. From the result it is evident that the observed bias scales linearly with $A_{\rm CB}$, as expected. This also suggests that, if a rotation field with $A_{\rm CB} = 10^{-6}$, which is well below the current observational constraint, were present but not accounted for in CMB lensing reconstruction, our estimated $C_L^{\phi\phi}$ may be biased low by $\gtrsim 10\%$ at the small scales, and as shown in Fig. 20, the bias gets marginally worse at higher noise levels.

We also find that the bias, $\Delta(\hat{C}_L^{\phi\phi})_{\rm rot}/C_L^{\phi\phi}$, has a shape that roughly follows that of the term, $-N_L^{(0)}/C_L^{\phi\phi}$, as shown in Fig. 23. Terms in Eq. (156) and (157) are quadratic in α which are similar to the $N_L^{(1)}$ bias in CMB lensing, and the $N_L^{(1)}$ bias (quadratic in ϕ) is in general not linear to $N_L^{(0)}$ in the context of CMB lensing (see, e.g., [148, 149]). The apparent linearity between the observed bias and $N_L^{(0)}$ seen in Fig. 23 is therefore surprising and may be a consequence of the scale-invariance of the rotation field in consideration or coincidental. We leave a detailed investigation of the shape of the bias to a future work.

Bias to the CMB lensing power spectrum may lead to bias in the cosmological parameters extracted from it. For example, the sum of neutrino masses can be constrained using CMB lensing power spectrum as massive neutrino can suppress CMB lensing power spectrum by several percents due to its suppression effect on the matter power spectrum below the neutrino free-streaming scale [150, 151]; it has also been shown in [152] that bias in the high-L may lead to bias in $\sigma_8\Omega_{\rm m}^{0.25}$ at 1σ level. Therefore, the bias from rotation field needs to be carefully accounted for when constraining cosmological parameters using CMB lensing power spectrum.

Note that we have only considered the EB estimator for lensing reconstruction, but we expect a similar effect to be present with other polarization-based quadratic estimators, such as the EE estimators. As we expect polarization-based estimators to contribute substantial statistical power in CMB lensing reconstruction in a CMB-S3-like experiment and dominates

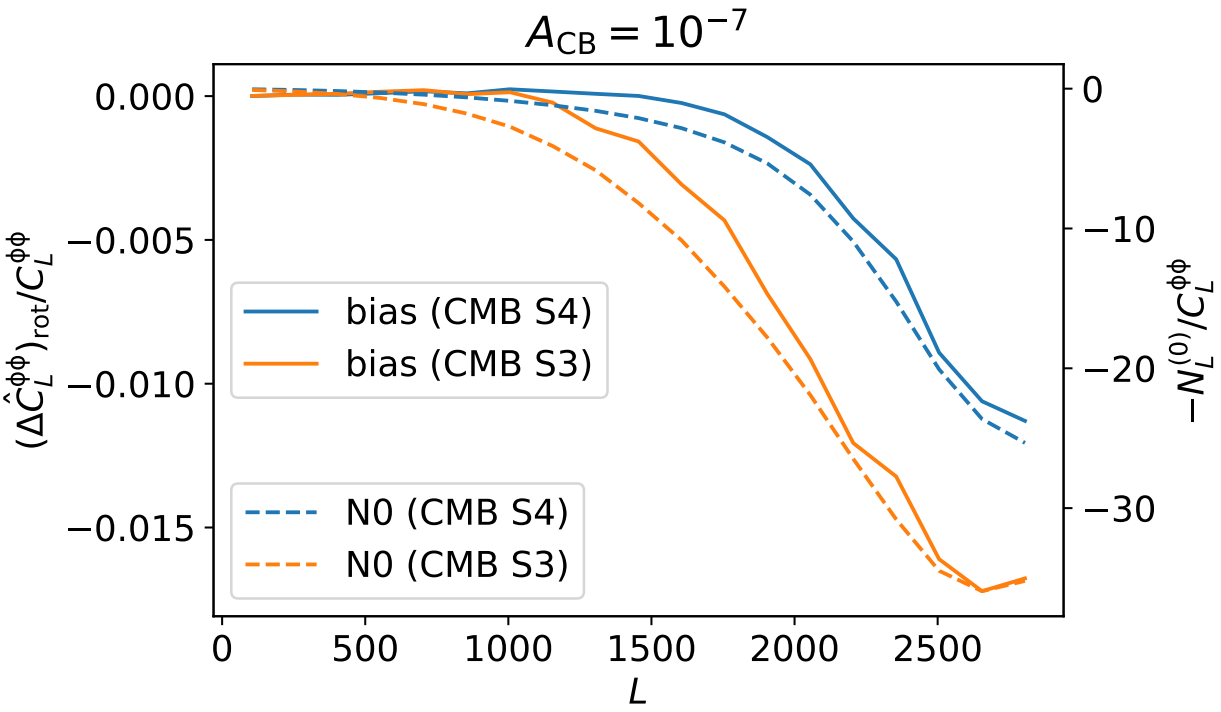

Figure 23: Over-plotting the observed bias (solid lines) with $-N_L^{(0)}/C_L^{\phi\phi}$ (dashed lines), where $N_L^{(0)}$ is obtained by averaging the ${}^{(\rm RD)}N^{(0)}$ from the lensed simulations (without rotation). The minus sign in front of $N_L^{(0)}$ is added to aid visual comparison.

the statistical power in a CMB-S4-like experiment [115], rotation-induced bias is thus an important factor to account for. On the other hand, lensing reconstruction with TT estimator should remain unaffected by rotation because it only affects CMB polarization fields; this suggests that an easy diagnostic of the rotation-induced bias is to compare the reconstructed lensing power spectrum obtained from TT and EB estimators and look for a reduction of power in the latter.

Multiple methods for mitigating biases in a CMB lensing measurement have been proposed. For example, the bias-hardening approach [62, 153, 63, 64] has been used to mitigate the mean-field bias in the reconstructed lensing map. In our case, however, this approach does not apply since the leading-order rotation fields do not produce mean-field bias in the reconstructed lensing map (see Eq. (145)). A simple approach to mitigate the rotation-induced bias arising from the connected four-point correlation is to first reconstruct the rotation fields using the quadratic estimator similar to the lensing reconstruction [31, 30] and then to de-rotate polarization maps using the reconstructed rotation fields as originally proposed by [138]. We leave a detailed analysis on the effectiveness of this approach to a future work.

6 Conclusion

CMB lensing encodes a wealth of information of late-time matter fluctuations over a broad range of redshifts, and the measurement of CMB lensing is becoming one of the most powerful cosmological probes for ongoing and upcoming experiments. The CMB lensing power spectrum probes the projected mass distribution, and hence is sensitive to both the growth of structure and the geometry of the universe. It can be used to constrain the cosmological parameters like the sum of neutrino masses, the linear-theory matter fluctuation amplitude, the curvature of the universe and the dark energy equation of state.

However, the reconstructed CMB lensing power spectrum can be biased by many secondary effects. In this paper we investigated the bias from anisotropic polarization rotation to the reconstructed CMB lensing power spectrum using EB estimator. This bias has often

been investigated in the context of instrumental systematics [125, 126], without reference to theoretical models. In this work we focused instead on a particular class of physically motivated models that produce anisotropic cosmic birefringence, such as axion-like particles coupling to photons through Chern-Simons interaction or primordial magnetic field, both of which have not been well-constrained by the current experiments. In addition, we aimed to identify the dominant terms responsible for the rotation-induced bias to CMB lensing which have not been clarified in previous works.

Our results have shown that anisotropic cosmic birefringence with $A_{\rm CB} = 10^{-7}$ can induce a percent-level bias to reconstructed CMB lensing power spectrum at small scales ($L > 1000$) for both CMB-S3-like and CMB-S4-like experiments, and the bias scales linearly with $A_{\rm CB}$. This suggests that if a rotation field with $A_{\rm CB} = 10^{-6}$ is present which is well-below our current observational constraint, the reconstructed lensing power spectrum can be biased low by $\gtrsim 10\%$. We also found that the observed bias likely arises from the the connected terms in the CMB four-point correlation function induced by the leading-order perturbation from rotation; this explains the linear scaling of the bias with $A_{\rm CB}$.

Polarization-based lensing reconstruction is expected to dominate or contribute substantially to the statistical power in CMB lensing reconstruction in the next generation CMB experiments. Rotation-induced bias to the CMB lensing power spectrum, therefore, may lead to non-negligible bias in the constraints of cosmological parameters such as the sum of neutrino masses and σ_8 and poses a significant challenge to achieving the science goals in future CMB lensing analysis. Thus, rotation field is an important factor to account for and mitigate during lensing reconstruction. We argued that the bias-hardened estimator approach to mitigate bias does not work for rotation-induced bias, because of the orthogonality between rotation and CMB lensing. A promising mitigation method is to first reconstruct the anisotropic rotation field and then de-rotate the CMB polarization field with the reconstructed rotation field before proceeding to lensing reconstruction, but its effectiveness in the presence of galactic foreground and partial sky coverage remains to be seen.

As we have demonstrated in this paper, the reconstructed lensing power spectrum is highly sensitive to the level of anisotropic cosmic birefringence. Besides posing a challenge to CMB lensing science, it may also provide a promising way to tightly constrain cosmic bire-

fringence, which is physically interesting in itself. This can be done by, e.g., comparing the reconstructed lensing power spectrum from TT and EB estimators. We leave an application of this effect to constrain cosmic birefringence to a follow-up work.

5.0 Conclusion

The first focus of this thesis is CMB lensing, which is a powerful tool of mapping the mass distribution and probing physics between the last scattering surface to us. CMB lensing imprints statistical signatures on CMB maps, and it can be measured statistically by quadratic estimators. However, the CMB lensing measurement can be biased by secondary effects. With the increasing sensitivity of CMB measurements, it is necessary to study carefully these bias sources at smaller scales. In this thesis, I introduced the bias to CMB lensing reconstruction from kinematic Sunyaev–Zel'dovich (SZ) kSZ effect and the potential bias from cosmic birefringence respectively, and showed how much we need to worry about them for the ongoing and upcoming CMB experiments. It is shown that understanding and mitigating these biases will be crucial for accurate measurement of CMB lensing and for extracting meaningful cosmological information from the data like the sum of neutrino masses.

The other focus of this thesis is cosmic birefringence which is an important scientific goal of modern cosmology and has important implications for our understanding of the early universe, as well as for the study of cosmic microwave background radiation and large-scale structure formation. On one hand, I introduced my work on `class_rot` which is a new publicly available code for calculating rotated CMB power spectra due to cosmic birefringence numerically. On the other hand, I introduced the potential bias to CMB lensing power spectrum measurement from cosmic birefringence. The effect of cosmic birefringence on the CMB polarization pattern is similar to that of CMB lensing, which both cause small distortions in the polarization pattern. The study of both CMB lensing and cosmic birefringence is an active area of research in cosmology and astrophysics. Together, they provide important insights into the structure and evolution of the universe, as well as into the fundamental physics that governs its behavior.

6.0 Appendix

Here we review the realization-dependent Gaussian noise (RDN0) applied in Eq. (150) and (151). RND0 is introduced in [62, 154] as a robust way to evaluate the reconstruction noise to CMB lensing power spectrum sourced by the disconnected terms of CMB four-point function (Gaussian noise). It has been applied in the CMB lensing power spectrum measurements of different experiments including [118, 119, 120]). In this section, we revisit the derivation of RDN0. We will adopt the flat-sky approximation in [62], but the result applies to both flat-sky and full-sky analyses.

We start by defining the Gaussian probability distribution function (PDF) of the unlensed CMB multipoles as

$$P_{\rm g} = \frac{1}{\sqrt{(2\pi)^N \det C}} \exp\left(-\frac{1}{2}\sum_{ab}\sum_{\boldsymbol{\ell}\boldsymbol{\ell}'} a_{\boldsymbol{\ell}} \left(\mathrm{C}^{-1}\right)^{a_{\boldsymbol{\ell}}, b_{\boldsymbol{\ell}'}} b_{\boldsymbol{\ell}'}\right), \tag{158}$$

where C is the covariance matrix between CMB multipoles, $a_{\boldsymbol{\ell}}, b_{\boldsymbol{\ell}'}$ represent the CMB multipoles, and $a, b \in \{T, E, B\}$.

When CMB fields are distorted by weak lensing, CMB multipoles become weakly non-Gaussian. The PDF of the lensed CMB multipoles can then be approximated using the Edgeworth expansion as [155, 156]

$$P \approx \left[1 + \sum_{abcd}\sum_{\{\boldsymbol{\ell}_i\}} \langle a_{\boldsymbol{\ell}_1} b_{\boldsymbol{\ell}_2} c_{\boldsymbol{\ell}_3} d_{\boldsymbol{\ell}_4}\rangle_c \frac{\partial}{\partial a_{\boldsymbol{\ell}_1}} \frac{\partial}{\partial b_{\boldsymbol{\ell}_2}} \frac{\partial}{\partial c_{\boldsymbol{\ell}_3}} \frac{\partial}{\partial d_{\boldsymbol{\ell}_4}}\right] P_{\rm g}, \tag{159}$$

where $\langle a_{\boldsymbol{\ell}_1} b_{\boldsymbol{\ell}_2} c_{\boldsymbol{\ell}_3} d_{\boldsymbol{\ell}_4}\rangle_c$ represents the connected terms (also known as cumulants or trispectrum) contributed by CMB lensing, given by [154]

$$\begin{aligned}\langle a_{\boldsymbol{\ell}_1} b_{\boldsymbol{\ell}_2} c_{\boldsymbol{\ell}_3} d_{\boldsymbol{\ell}_4}\rangle_{\rm c} \approx\ & f^{ab}_{\boldsymbol{\ell}_{12},\boldsymbol{\ell}_1} f^{cd}_{-\boldsymbol{\ell}_{12},\boldsymbol{\ell}_3} C^{\phi\phi}_{|\boldsymbol{\ell}_{12}|} \delta_{\boldsymbol{\ell}_{12},-\boldsymbol{\ell}_{34}} \\ &+ f^{ac}_{\boldsymbol{\ell}_{13},\boldsymbol{\ell}_1} f^{bd}_{-\boldsymbol{\ell}_{13},\boldsymbol{\ell}_2} C^{\phi\phi}_{|\boldsymbol{\ell}_{13}|} \delta_{\boldsymbol{\ell}_{13},-\boldsymbol{\ell}_{24}} \\ &+ f^{ad}_{\boldsymbol{\ell}_{14},\boldsymbol{\ell}_1} f^{bc}_{-\boldsymbol{\ell}_{14},\boldsymbol{\ell}_2} C^{\phi\phi}_{|\boldsymbol{\ell}_{14}|} \delta_{\boldsymbol{\ell}_{14},-\boldsymbol{\ell}_{23}},\end{aligned} \tag{160}$$

to the leading order of $C_L^{\phi\phi}$, where $\boldsymbol{\ell}_{ij} \equiv \boldsymbol{\ell}_i + \boldsymbol{\ell}_j$, and $f^{ab}_{\boldsymbol{\ell},\boldsymbol{\ell}'}$ represents the weight functions for lensing potential as in [154].

We can then obtain an optimal estimator, $\widehat{C}_L^{\phi\phi}$, by maximizing the log-likelihood, $\mathcal{L} \equiv \ln P$, with

$$\frac{\partial \mathcal{L}}{\partial C_L^{\phi\phi}} \left(\widehat{C}_L^{\phi\phi} \right) = 0, \tag{161}$$

and get [154]

$$\widehat{C}_L^{\phi\phi} \propto \sum_{abcd} \sum_{|\boldsymbol{L}|=L} P_g^{-1} \left(\widehat{f}_{\boldsymbol{L}}^{ab} \widehat{f}_{-\boldsymbol{L}}^{cd} + \widehat{f}_{\boldsymbol{L}}^{ac} \widehat{f}_{-\boldsymbol{L}}^{bd} + \widehat{f}_{\boldsymbol{L}}^{ad} \widehat{f}_{-\boldsymbol{L}}^{bc} \right) P_{\rm g}, \tag{162}$$

where we have defined

$$\widehat{f}_{\boldsymbol{L}}^{ab} \equiv \sum_{\boldsymbol{\ell}'} f_{\boldsymbol{L},\boldsymbol{\ell}'}^{ab} \frac{\partial}{\partial a_{\boldsymbol{L}}} \frac{\partial}{\partial b_{\boldsymbol{L}-\boldsymbol{\ell}'}}, \tag{163}$$

and have omitted the normalization. One can further show that

$$\widehat{f}_{\boldsymbol{L}}^{ab} P_{\rm g} = \left(\bar{x}_{\boldsymbol{L}}^{ab} - \left\langle \bar{x}_{\boldsymbol{L}}^{ab} \right\rangle \right) P_{\rm g}, \tag{164}$$

where

$$\bar{x}_{\boldsymbol{L}}^{ab} \equiv \sum_{\boldsymbol{\ell}} f_{\boldsymbol{L},\boldsymbol{\ell}}^{ab} \bar{a}_{\boldsymbol{\ell}} \bar{b}_{\boldsymbol{L}-\boldsymbol{\ell}}, \tag{165}$$

in which $\bar{a}_{\boldsymbol{\ell}} = \sum_{a',\boldsymbol{\ell}'} C^{-1}_{a_{\boldsymbol{\ell}} a'_{\boldsymbol{\ell}'}} a'_{\boldsymbol{\ell}'}$ represents the inverse-variance filtered CMB multipoles. Note that $\bar{x}_{\boldsymbol{L}}^{ab}$ resembles the unnormalized quadratic estimator for CMB lensing, and $\left\langle \bar{x}_{\boldsymbol{L}}^{ab} \right\rangle$ the mean-field bias[a].

One can further show that

$$P_g^{-1} \widehat{f}_{\boldsymbol{L}}^{ab} \widehat{f}_{-\boldsymbol{L}}^{cd} P_{\rm g} \propto \left[\left(\bar{x}_{\boldsymbol{L}}^{ab} - \left\langle \bar{x}_{\boldsymbol{L}}^{ab} \right\rangle \right) \left(\bar{x}_{-\boldsymbol{L}}^{cd} - \left\langle \bar{x}_{-\boldsymbol{L}}^{cd} \right\rangle \right) - n_{\boldsymbol{L}}^{ab,cd} \right], \tag{166}$$

with

$$\begin{aligned} n_{\boldsymbol{L}}^{ab,cd} \equiv & \sum_{\boldsymbol{\ell}_1,\boldsymbol{\ell}_2} f_{\boldsymbol{L},\boldsymbol{\ell}_1}^{ab} f_{-\boldsymbol{L},\boldsymbol{\ell}_2}^{cd} \times \\ & (\bar{b}_{\boldsymbol{L}-\boldsymbol{\ell}_1} \bar{d}_{-\boldsymbol{L}-\boldsymbol{\ell}_1} C^{-1}_{a_{\boldsymbol{\ell}_1},c_{\boldsymbol{\ell}_2}} + \bar{b}_{\boldsymbol{L}-\boldsymbol{\ell}_1} \bar{c}_{-\boldsymbol{L}-\boldsymbol{\ell}_1} C^{-1}_{a_{\boldsymbol{\ell}_1},d_{\boldsymbol{\ell}_2}} \\ & + \bar{a}_{\boldsymbol{L}-\boldsymbol{\ell}_1} \bar{d}_{-\boldsymbol{L}-\boldsymbol{\ell}_1} C^{-1}_{b_{\boldsymbol{\ell}_1},c_{\boldsymbol{\ell}_2}} + \bar{a}_{\boldsymbol{L}-\boldsymbol{\ell}_1} \bar{c}_{-\boldsymbol{L}-\boldsymbol{\ell}_1} C^{-1}_{b_{\boldsymbol{\ell}_1},d_{\boldsymbol{\ell}_2}}) \\ & - \frac{1}{2} \sum_{\boldsymbol{\ell}_1,\boldsymbol{\ell}_2} f_{\boldsymbol{L},\boldsymbol{\ell}_1}^{ab} f_{-\boldsymbol{L},\boldsymbol{\ell}_2}^{cd} \times \\ & (C^{-1}_{a_{\boldsymbol{\ell}_1},c_{\boldsymbol{\ell}_2}} C^{-1}_{b_{\boldsymbol{L}-\boldsymbol{\ell}_1},d_{-\boldsymbol{L}-\boldsymbol{\ell}_2}} + C^{-1}_{a_{\boldsymbol{\ell}_1},d_{\boldsymbol{\ell}_2}} C^{-1}_{b_{\boldsymbol{L}-\boldsymbol{\ell}_1},c_{-\boldsymbol{L}-\boldsymbol{\ell}_2}} \\ & + C^{-1}_{b_{\boldsymbol{\ell}_1},c_{\boldsymbol{\ell}_2}} C^{-1}_{a_{\boldsymbol{L}-\boldsymbol{\ell}_1},d_{-\boldsymbol{L}-\boldsymbol{\ell}_2}} + C^{-1}_{b_{\boldsymbol{\ell}_1},d_{\boldsymbol{\ell}_2}} C^{-1}_{a_{\boldsymbol{L}-\boldsymbol{\ell}_1},c_{-\boldsymbol{L}-\boldsymbol{\ell}_2}}), \end{aligned} \tag{167}$$

[a] In the real experiments, the mean-field bias is estimated by averaging the reconstructed maps using simulated CMB realizations based on the fiducial model. The mean-field bias does not affect the result in this paper.

where we have used

$$C^{-1}_{a_{\boldsymbol{\ell}} a'_{\boldsymbol{\ell}'}} = \langle \bar{a}_{\boldsymbol{\ell}} \bar{a}'_{\boldsymbol{\ell}'} \rangle. \tag{168}$$

With Eq. (166), the optimal estimator for CMB lensing potential in Eq. (162) becomes

$$\begin{aligned} \widehat{C}_L^{\phi\phi} \propto & \sum_{abcd} \sum_{|\boldsymbol{L}|=L} \Bigg(\left[\left(\bar{x}^{ab}_{\boldsymbol{L}} - \left\langle \bar{x}^{ab}_{\boldsymbol{L}} \right\rangle \right) \left(\bar{x}^{cd}_{-\boldsymbol{L}} - \left\langle \bar{x}^{cd}_{-\boldsymbol{L}} \right\rangle \right) - n^{ab,cd}_{\boldsymbol{L}} \right] \\ & + [b \leftrightarrow c] + [b \leftrightarrow d] \Bigg). \end{aligned} \tag{169}$$

Note that $\bar{a}, \bar{b}, \bar{c}, \bar{d}$ in Eq. (167) correspond to filtered CMB multipoles from *data*, whereas the covariance matrices, e.g., $C_{a_{\boldsymbol{\ell}_1}, c_{\boldsymbol{\ell}_2}}$, are to be estimated from *simulations*. In particular, we apply two sets of Monte-Carlo CMB realizations based on the same fiducial cosmological model to estimate the covariance matrix, denoted as S_1 and S_2. Specifically, S_1 is used to estimate the covariance matrices in the first parentheses of Eq. (167); each product of covariance matrices in the second parenthesis of Eq. (167) is estimated using S1 and S2 respectively (i.e., $C^{-1}_{S1} C^{-1}_{S2}$). This way of estimating the covariance matrix is less sensitive to errors in the covariance matrix from statistical uncertainties as well as mis-modeling. To see that, we can express the estimated covariance matrix as $\hat{C} = \bar{C} + \Delta C$, with $\bar{C}$ the true covariance matrix and ΔC the error. It is then easy to check that, when averaging over different CMB realizations, the error in covariance matrix, ΔC, does not contribute to $\langle n^{ab,cd}_{\boldsymbol{L}} \rangle$ in the leading order. Since S_1 and S_2 are assumed to be independent, statistical uncertainties in $\hat{C}$ will also be eliminated up to $O((\Delta C)^2)$.

Incorporating the estimation of covariance matrices using S_1 and S_2, Eq. (167) can be expressed more succinctly as

$$\begin{aligned} n^{ab,cd}_{\boldsymbol{L}} = & \left\langle \left(\bar{x}^{a^{S_1} b}_{\boldsymbol{L}} + \bar{x}^{a b^{S_1}}_{\boldsymbol{L}} \right) \left(\bar{x}^{c^{S_1} d}_{-\boldsymbol{L}} + \bar{x}^{c d^{S_1}}_{-\boldsymbol{L}} \right) \right\rangle_{S_1} - \\ & \frac{1}{2} \left\langle \left(\bar{x}^{a^{S_1} b^{S_2}}_{\boldsymbol{L}} + \bar{x}^{a^{S_2} b^{S_1}}_{\boldsymbol{L}} \right) \left(\bar{x}^{c^{S_1} d^{S_2}}_{-\boldsymbol{L}} + \bar{x}^{c^{S_2} d^{S_1}}_{-\boldsymbol{L}} \right) \right\rangle_{S_1, S_2}, \end{aligned} \tag{170}$$

where the superscripts S_i denote the CMB simulation provided by the set of S_i, and $\langle ... \rangle_{S_i}$ represents the average over the realizations of S_i. Adding back the omitted normalization

in Eq. (170), and the omitted normalization, we obtain the realization-dependent Gaussian noise (RDN0) with a given set of $\{ab, cd\}$ as

$$\begin{aligned}
{}^{(\mathrm{RD})}\mathrm{N}_L^{(0)ab,cd} &\propto \sum_{|\boldsymbol{L}|=L} n_{\boldsymbol{L}}^{ab,cd} \\
&= \langle C_L^{\hat{\phi}\hat{\phi}}[ab^{S_1}, cd^{S_1}] + C_L^{\hat{\phi}\hat{\phi}}[a^{S_1}b, ab^{S_1}] \\
&\quad + C_L^{\hat{\phi}\hat{\phi}}[a^{S_1}b, c^{S_1}d] + C_L^{\hat{\phi}\hat{\phi}}[ab^{S_1}, c^{S_1}d] \\
&\quad - C_L^{\hat{\phi}\hat{\phi}}[a^{S_1}b^{S_2}, c^{S_1}d^{S_2}] \\
&\quad - C_L^{\hat{\phi}\hat{\phi}}[a^{S_1}b^{S_2}, c^{S_2}d^{S_1}]\rangle_{S_1,S_2}.
\end{aligned} \tag{171}$$

In the context of this paper, we set $a = c = E$, $b = d = B$. S_1 and S_2 are two sets of independent lensed CMB realizations based on the fiducial cosmological model which does not include the cosmic birefringence effect. As a result, for the lensed-only *data* maps, the RDN0 is given by Eq. (150); for the rotated-lensed *data* maps, the RDN0 is given by Eq. (151).

Note that by averaging ${}^{(\mathrm{RD})}\mathrm{N}_L^{(0)}$ over many CMB realisations, we reproduce the naive Gaussian reconstruction noise $\mathrm{N}_L^{(0)}$. However, one can see that ${}^{(\mathrm{RD})}\mathrm{N}_L^{(0)}$ is more optimal because it preserves the critical realisation-dependent information which is lost in $\mathrm{N}_L^{(0)}$ after averaging. In addition, as previously discussed, RDN0 is also less sensitive to the errors in the covariance matrix such as the statistical uncertainties from the limited set of simulations used to calculate the covariance matrix and errors in the underlying fiducial model used to generate the simulations. It has been demonstrated in [69] that such an error in covariance matrix may lead to a catastrophic error (see Fig. 2 of [69]) in the estimated lensing power spectrum if the naive $N_L^{(0)}$ is used, and it is significantly reduced with RDN0.

Bibliography

[1] N. Aghanim et al. Planck 2018 results. I. Overview and the cosmological legacy of Planck. *Astron. Astrophys.*, 641:A1, 2020.

[2] N. Aghanim et al. Planck 2018 results. VI. Cosmological parameters. *Astron. Astrophys.*, 641:A6, 2020. [Erratum: Astron.Astrophys. 652, C4 (2021)].

[3] Diego Blas, Julien Lesgourgues, and Thomas Tram. The Cosmic Linear Anisotropy Solving System (CLASS). Part II: Approximation schemes. J. Cosmology Astropart. Phys., 2011(7):034, July 2011.

[4] Lawrence Krauss, Scott Dodelson, and Stephan Meyer. Primordial Gravitational Waves and Cosmology. *Science*, 328:989–992, 2010.

[5] George Stein, Marcelo A. Alvarez, J. Richard Bond, Alexander van Engelen, and Nicholas Battaglia. The websky extragalactic cmb simulations. *Journal of Cosmology and Astroparticle Physics*, 2020(10):012–012, Oct 2020.

[6] Neelima Sehgal, Paul Bode, Sudeep Das, Carlos Hernandez-Monteagudo, Kevin Huffenberger, Yen-Ting Lin, Jeremiah P. Ostriker, and Hy Trac. Simulations of the microwave sky. *The Astrophysical Journal*, 709(2):920–936, Jan 2010.

[7] Simone Ferraro and J. Colin Hill. Bias to cmb lensing reconstruction from temperature anisotropies due to large-scale galaxy motions. *Physical Review D*, 97(2):023512, 2018.

[8] Hongbo Cai and Yilun Guan. Computing microwave background polarization power spectra from cosmic birefringence. *Phys. Rev. D*, 105(6):063536, 2022.

[9] Adam G. Riess, Alexei V. Filippenko, Peter Challis, Alejandro Clocchiatti, Alan Diercks, Peter M. Garnavich, Ron L. Gilliland, Craig J. Hogan, Saurabh Jha, Robert P. Kirshner, B. Leibundgut, M. M. Phillips, David Reiss, Brian P. Schmidt, Robert A. Schommer, R. Chris Smith, J. Spyromilio, Christopher Stubbs, Nicholas B. Suntzeff, and John Tonry. Observational Evidence from Supernovae for an Accelerating Universe and a Cosmological Constant. AJ, 116(3):1009–1038, September 1998.

[10] S. Perlmutter, G. Aldering, G. Goldhaber, R. A. Knop, P. Nugent, P. G. Castro, S. Deustua, S. Fabbro, A. Goobar, D. E. Groom, I. M. Hook, A. G. Kim, M. Y. Kim, J. C. Lee, N. J. Nunes, R. Pain, C. R. Pennypacker, R. Quimby, C. Lidman, R. S. Ellis, M. Irwin, R. G. McMahon, P. Ruiz-Lapuente, N. Walton, B. Schaefer, B. J. Boyle, A. V. Filippenko, T. Matheson, A. S. Fruchter, N. Panagia, H. J. M. Newberg, W. J. Couch, and The Supernova Cosmology Project. Measurements of Ω and Λ from 42 High-Redshift Supernovae. ApJ, 517(2):565–586, June 1999.

[11] J. N. Goldberg, A. J. Macfarlane, E. T. Newman, F. Rohrlich, and E. C.G. Sudarshan. Spin-s spherical harmonics and O. *Journal of Mathematical Physics*, 8(11):2155–2161, nov 1967.

[12] Marc Kamionkowski, Arthur Kosowsky, and Albert Stebbins. A Probe of primordial gravity waves and vorticity. *Phys. Rev. Lett.*, 78:2058–2061, 1997.

[13] Matias Zaldarriaga and Uroš Seljak. All-sky analysis of polarization in the microwave background. Phys. Rev. D, 55(4):1830–1840, February 1997.

[14] Lloyd Knox and Michael S. Turner. Detectability of tensor perturbations through anisotropy of the cosmic background radiation. *Phys. Rev. Lett.*, 73:3347–3350, Dec 1994.

[15] Toshiya Namikawa, Yilun Guan, Omar Darwish, Blake D. Sherwin, Simone Aiola, Nicholas Battaglia, James A. Beall, Daniel T. Becker, J. Richard Bond, Erminia Calabrese, Grace E. Chesmore, Steve K. Choi, Mark J. Devlin, Joanna Dunkley, Rolando Dünner, Anna E. Fox, Patricio A. Gallardo, Vera Gluscevic, Dongwon Han, Matthew Hasselfield, Gene C. Hilton, Adam D. Hincks, Renée Hložek, Johannes Hubmayr, Kevin Huffenberger, John P. Hughes, Brian J. Koopman, Arthur Kosowsky, Thibaut Louis, Marius Lungu, Amanda MacInnis, Mathew S. Madhavacheril, Maya Mallaby-Kay, Loïc Maurin, Jeffrey McMahon, Kavilan Moodley, Sigurd Naess, Federico Nati, Laura B. Newburgh, John P. Nibarger, Michael D. Niemack, Lyman A. Page, Frank J. Qu, Naomi Robertson, Alessandro Schillaci, Neelima Sehgal, Cristóbal Sifón, Sara M. Simon, David N. Spergel, Suzanne T. Staggs, Emilie R. Storer, Alexander van Engelen, Jeff van Lanen, and Edward J. Wollack. Atacama Cosmology Telescope: Constraints on cosmic birefringence. Phys. Rev. D, 101(8):083527, April 2020.

[16] Antony Lewis and Anthony Challinor. Weak gravitational lensing of the CMB. *Phys. Rept.*, 429:1–65, 2006.

[17] Blake D. Sherwin, Alexander van Engelen, Neelima Sehgal, Mathew Madhavacheril, Graeme E. Addison, Simone Aiola, Rupert Allison, Nicholas Battaglia, Daniel T. Becker, James A. Beall, J. Richard Bond, Erminia Calabrese, Rahul Datta, Mark J. Devlin, Rolando Dünner, Joanna Dunkley, Anna E. Fox, Patricio Gallardo, Mark Halpern, Matthew Hasselfield, Shawn Henderson, J. Colin Hill, Gene C. Hilton, Johannes Hubmayr, John P. Hughes, Adam D. Hincks, Renée Hlozek, Kevin M. Huffenberger, Brian Koopman, Arthur Kosowsky, Thibaut Louis, Loïc Maurin, Jeff McMahon, Kavilan Moodley, Sigurd Naess, Federico Nati, Laura Newburgh, Michael D. Niemack, Lyman A. Page, Jonathan Sievers, David N. Spergel, Suzanne T. Staggs, Robert J. Thornton, Jeff Van Lanen, Eve Vavagiakis, and Edward J. Wollack. Two-season Atacama Cosmology Telescope polarimeter lensing power spectrum. Phys. Rev. D, 95(12):123529, June 2017.

[18] A. van Engelen, R. Keisler, O. Zahn, K. A. Aird, B. A. Benson, L. E. Bleem, J. E. Carlstrom, C. L. Chang, H. M. Cho, T. M. Crawford, A. T. Crites, T. de Haan, M. A.

Dobbs, J. Dudley, E. M. George, N. W. Halverson, G. P. Holder, W. L. Holzapfel, S. Hoover, Z. Hou, J. D. Hrubes, M. Joy, L. Knox, A. T. Lee, E. M. Leitch, M. Lueker, D. Luong-Van, J. J. McMahon, J. Mehl, S. S. Meyer, M. Millea, J. J. Mohr, T. E. Montroy, T. Natoli, S. Padin, T. Plagge, C. Pryke, C. L. Reichardt, J. E. Ruhl, J. T. Sayre, K. K. Schaffer, L. Shaw, E. Shirokoff, H. G. Spieler, Z. Staniszewski, A. A. Stark, K. Story, K. Vanderlinde, J. D. Vieira, and R. Williamson. A Measurement of Gravitational Lensing of the Microwave Background Using South Pole Telescope Data. ApJ, 756(2):142, September 2012.

[19] Wayne Hu and Takemi Okamoto. Mass Reconstruction with Cosmic Microwave Background Polarization. ApJ, 574(2):566–574, August 2002.

[20] Takemi Okamoto and Wayne Hu. Cosmic microwave background lensing reconstruction on the full sky. Phys. Rev. D, 67(8):083002, April 2003.

[21] N. Aghanim et al. Planck 2018 results. VIII. Gravitational lensing. *Astron. Astrophys.*, 641:A8, 2020.

[22] P. A. R. Ade et al. Planck 2015 results. XIII. Cosmological parameters. *Astron. Astrophys.*, 594:A13, 2016.

[23] Sean M. Carroll. Quintessence and the Rest of the World: Suppressing Long-Range Interactions. Phys. Rev. Lett., 81(15):3067–3070, October 1998.

[24] Mingzhe Li and Xinmin Zhang. Cosmological CPT violating effect on CMB polarization. *Phys. Rev. D*, 78:103516, 2008.

[25] David J. E. Marsh. Axion Cosmology. *Phys. Rept.*, 643:1–79, 2016.

[26] David Leon, Jonathan Kaufman, Brian Keating, and Matthew Mewes. The cosmic microwave background and pseudo-Nambu–Goldstone bosons: Searching for Lorentz violations in the cosmos. *Mod. Phys. Lett. A*, 32(02):1730002, 2016.

[27] Arthur Kosowsky and Abraham Loeb. Faraday rotation of microwave background polarization by a primordial magnetic field. *Astrophys. J.*, 469:1–6, 1996.

[28] Diego D. Harari, Justin D. Hayward, and Matias Zaldarriaga. Depolarization of the cosmic microwave background by a primordial magnetic field and its effect upon temperature anisotropy. *Phys. Rev. D*, 55:1841–1850, 1997.

[29] Robert R. Caldwell, Vera Gluscevic, and Marc Kamionkowski. Cross-correlation of cosmological birefringence with CMB temperature. Phys. Rev. D, 84(4):043504, August 2011.

[30] Amit P. S. Yadav, Meng Su, and Matias Zaldarriaga. Primordial B-mode diagnostics and self-calibrating the CMB polarization. Phys. Rev. D, 81(6):063512, March 2010.

[31] Vera Gluscevic, Marc Kamionkowski, and Asantha Cooray. Derotation of the cosmic microwave background polarization: Full-sky formalism. *Physical Review D*, 80(2), jul 2009.

[32] F. Bianchini et al. Searching for Anisotropic Cosmic Birefringence with Polarization Data from SPTpol. *Phys. Rev. D*, 102(8):083504, 2020.

[33] Levon Pogosian, Meir Shimon, Matthew Mewes, and Brian Keating. Future CMB constraints on cosmic birefringence and implications for fundamental physics. Phys. Rev. D, 100(2):023507, July 2019.

[34] Sayan Mandal, Neelima Sehgal, and Toshiya Namikawa. Finding evidence for inflation and the origin of galactic magnetic fields with CMB surveys. *Phys. Rev. D*, 105(6):063537, 2022.

[35] R. J. Bouwens, G. D. Illingworth, P. A. Oesch, M. Trenti, I. Labbé, L. Bradley, M. Carollo, P. G. van Dokkum, V. Gonzalez, B. Holwerda, M. Franx, L. Spitler, R. Smit, and D. Magee. UV Luminosity Functions at Redshifts z $\sim$ 4 to z $\sim$ 10: 10,000 Galaxies from HST Legacy Fields. ApJ, 803(1):34, April 2015.

[36] William R. Coulton, Atsuhisa Ota, and Alexander van Engelen. Cosmology with the Thermal-Kinetic Sunyaev-Zel'dovich Effect. *Phys. Rev. Lett.*, 125(11):111301, 2020.

[37] C. L. Reichardt, L. Shaw, O. Zahn, K. A. Aird, B. A. Benson, L. E. Bleem, J. E. Carlstrom, C. L. Chang, H. M. Cho, T. M. Crawford, A. T. Crites, T. de Haan, M. A. Dobbs, J. Dudley, E. M. George, N. W. Halverson, G. P. Holder, W. L. Holzapfel, S. Hoover, Z. Hou, J. D. Hrubes, M. Joy, R. Keisler, L. Knox, A. T. Lee, E. M. Leitch, M. Lueker, D. Luong-Van, J. J. McMahon, J. Mehl, S. S. Meyer, M. Millea, J. J. Mohr, T. E. Montroy, T. Natoli, S. Padin, T. Plagge, C. Pryke, J. E. Ruhl, K. K. Schaffer, E. Shirokoff, H. G. Spieler, Z. Staniszewski, A. A. Stark, K. Story, A. van Engelen, K. Vanderlinde, J. D. Vieira, and R. Williamson. A MEASUREMENT OF SECONDARY COSMIC MICROWAVE BACKGROUND ANISOTROPIES WITH TWO YEARS OF SOUTH POLE TELESCOPE OBSERVATIONS. *The Astrophysical Journal*, 755(1):70, jul 2012.

[38] Hongbo Cai, Mathew S. Madhavacheril, J. Colin Hill, and Arthur Kosowsky. Bias to cosmic microwave background lensing reconstruction from the kinematic Sunyaev-Zel'dovich effect at reionization. *Phys. Rev. D*, 105(4):043516, 2022.

[39] A Lewis and A Challinor. Weak gravitational lensing of the cmb. *Physics Reports*, 429(1):1–65, 2006.

[40] Duncan Hanson, Anthony Challinor, George Efstathiou, and Pawel Bielewicz. Cmb temperature lensing power reconstruction. *Physical Review D*, 83(4):043005, 2011.

[41] Jia Liu and J. Colin Hill. Cross-correlation of planck cmb lensing and cfhtlens galaxy weak lensing maps. *Phys. Rev. D*, 92:063517, Sep 2015.

[42] F. Bianchini et al. Constraints on Cosmological Parameters from the 500 deg^2 SPTpol Lensing Power Spectrum. *Astrophys. J.*, 888:119, 2020.

[43] Larissa Santos, Paolo Cabella, Amedeo Balbi, and Nicola Vittorio. Neutrinos and dark energy constraints from future galaxy surveys and CMB lensing information. *Phys. Rev. D*, 88(4):043505, 2013.

[44] R. Allison, P. Caucal, E. Calabrese, J. Dunkley, and T. Louis. Towards a cosmological neutrino mass detection. Phys. Rev. D, 92(12):123535, December 2015.

[45] Wayne Hu and Takemi Okamoto. Mass reconstruction with cmb polarization. *Astrophys. J.*, 574:566–574, 2002.

[46] Abhishek S. Maniyar, Yacine Ali-Haïmoud, Julien Carron, Antony Lewis, and Mathew S. Madhavacheril. Quadratic estimators for CMB weak lensing. Phys. Rev. D, 103(8):083524, April 2021.

[47] S. W. Henderson et al. Advanced ACTPol Cryogenic Detector Arrays and Readout. *J. Low Temp. Phys.*, 184(3-4):772–779, 2016.

[48] B. A. Benson et al. SPT-3G: A Next-Generation Cosmic Microwave Background Polarization Experiment on the South Pole Telescope. *Proc. SPIE Int. Soc. Opt. Eng.*, 9153:91531P, 2014.

[49] Peter Ade et al. The Simons Observatory: Science goals and forecasts. *JCAP*, 02:056, 2019.

[50] Kevork Abazajian et al. CMB-S4 Science Case, Reference Design, and Project Plan. 7 2019.

[51] Neelima Sehgal et al. CMB-HD: An Ultra-Deep, High-Resolution Millimeter-Wave Survey Over Half the Sky. 6 2019.

[52] C. Bennett et al. First year Wilkinson Microwave Anisotropy Probe (WMAP) observations: Foreground emission. *Astrophys. J. Suppl.*, 148:97, 2003.

[53] Mathew S. Madhavacheril et al. Atacama Cosmology Telescope: Component-separated maps of CMB temperature and the thermal Sunyaev-Zel'dovich effect. *Phys. Rev. D*, 102(2):023534, 2020.

[54] Y. Sultan Abylkairov, Omar Darwish, J. Colin Hill, and Blake D. Sherwin. Partially constrained internal linear combination: A method for low-noise CMB foreground mitigation. Phys. Rev. D, 103(10):103510, May 2021.

[55] L. E. Bleem, T. M. Crawford, B. Ansarinejad, B. A. Benson, S. Bocquet, J. E. Carlstrom, C. L. Chang, R. Chown, A. T. Crites, T. de Haan, M. A. Dobbs, W. B. Everett, E. M. George, R. Gualtieri, N. W. Halverson, G. P. Holder, W. L. Holzapfel, J. D. Hrubes, L. Knox, A. T. Lee, D. Luong-Van, D. P. Marrone, J. J. McMahon,

S. S. Meyer, M. Millea, L. M. Mocanu, J. J. Mohr, T. Natoli, Y. Omori, S. Padin, C. Pryke, S. Raghunathan, C. L. Reichardt, J. E. Ruhl, K. K. Schaffer, E. Shirokoff, Z. Staniszewski, A. A. Stark, J. D. Vieira, and R. Williamson. CMB/kSZ and Compton-y Maps from 2500 square degrees of SPT-SZ and Planck Survey Data. *arXiv e-prints*, page arXiv:2102.05033, February 2021.

[56] S. Y. Sazonov and R. A. Sunyaev. Cmb radiation in the direction of a moving cluster of galaxies with hot gas: Relativistic corrections. *Astrophys. J.*, 508:1–5, 1998.

[57] A. D. Dolgov, S. H. Hansen, S. Pastor, and D. V. Semikoz. Spectral distortion of cosmic background radiation by scattering on hot electrons. Exact calculations. *Astrophys. J.*, 554:74–84, 2001.

[58] Mathew S. Madhavacheril and J. Colin Hill. Mitigating foreground biases in CMB lensing reconstruction using cleaned gradients. Phys. Rev. D, 98(2):023534, July 2018.

[59] Noah Sailer, Emmanuel Schaan, Simone Ferraro, Omar Darwish, and Blake Sherwin. Optimal multifrequency weighting for CMB lensing. *Phys. Rev. D*, 104(12):123514, 2021.

[60] Omar Darwish, Blake D. Sherwin, Noah Sailer, Emmanuel Schaan, and Simone Ferraro. Optimizing foreground mitigation for CMB lensing with combined multifrequency and geometric methods. 10 2021.

[61] Emmanuel Schaan and Simone Ferraro. Foreground-Immune Cosmic Microwave Background Lensing with Shear-Only Reconstruction. *Phys. Rev. Lett.*, 122(18):181301, 2019.

[62] Toshiya Namikawa, Duncan Hanson, and Ryuichi Takahashi. Bias-hardened cmb lensing. *Monthly Notices of the Royal Astronomical Society*, 431(1):609–620, Feb 2013.

[63] Stephen J. Osborne, Duncan Hanson, and Olivier Doré. Extragalactic Foreground Contamination in Temperature-based CMB Lens Reconstruction. *JCAP*, 03:024, 2014.

[64] Noah Sailer, Emmanuel Schaan, and Simone Ferraro. Lower bias, lower noise CMB lensing with foreground-hardened estimators. *Phys. Rev. D*, 102(6):063517, 2020.

[65] Nishant Mishra and Emmanuel Schaan. Bias to CMB lensing from lensed foregrounds. *Phys. Rev. D*, 100(12):123504, 2019.

[66] P. A. R. Ade et al. Planck 2015 results. XIII. Cosmological parameters. *Astron. Astrophys.*, 594:A13, 2016.

[67] Wayne Hu and Takemi Okamoto. Mass reconstruction with cosmic microwave background polarization. *The Astrophysical Journal*, 574(2):566–574, Aug 2002.

[68] Michael H. Kesden, Asantha Cooray, and Marc Kamionkowski. Lensing reconstruction with CMB temperature and polarization. *Phys. Rev. D*, 67:123507, 2003.

[69] Mathew S. Madhavacheril, Kendrick M. Smith, Blake D. Sherwin, and Sigurd Naess. CMB lensing power spectrum estimation without instrument noise bias. 11 2020.

[70] Vanessa Böhm, Marcel Schmittfull, and Blake D. Sherwin. Bias to CMB lensing measurements from the bispectrum of large-scale structure. *Phys. Rev. D*, 94(4):043519, 2016.

[71] Vanessa Böhm, Blake D. Sherwin, Jia Liu, J. Colin Hill, Marcel Schmittfull, and Toshiya Namikawa. Effect of non-Gaussian lensing deflections on CMB lensing measurements. *Phys. Rev. D*, 98(12):123510, 2018.

[72] Giulio Fabbian, Matteo Calabrese, and Carmelita Carbone. CMB weak-lensing beyond the Born approximation: a numerical approach. J. Cosmology Astropart. Phys., 2018(2):050, February 2018.

[73] R. A. Sunyaev and Ya. B. Zeldovich. The velocity of clusters of galaxies relative to the microwave background. The possibility of its measurement. *Monthly Notices of the Royal Astronomical Society*, 190(3):413–420, 03 1980.

[74] Hyunbae Park, Paul R. Shapiro, Eiichiro Komatsu, Ilian T. Iliev, Kyungjin Ahn, and Garrelt Mellema. The Kinetic Sunyaev-Zel'dovich effect as a probe of the physics of cosmic reionization: the effect of self-regulated reionization. *Astrophys. J.*, 769:93, 2013.

[75] Nickolay Y. Gnedin and Andrew H. Jaffe. Secondary cosmic microwave background anisotropies from cosmological reionization. *The Astrophysical Journal*, 551(1):3–14, apr 2001.

[76] Lloyd Knox, Román Scoccimarro, and Scott Dodelson. Impact of inhomogeneous reionization on cosmic microwave background anisotropy. *Phys. Rev. Lett.*, 81:2004–2007, Sep 1998.

[77] N. Battaglia, H. Trac, R. Cen, and A. Loeb. Reionization on large scales. i. a parametric model constructed from radiation-hydrodynamic simulations. *The Astrophysical Journal*, 776(2):81, 2013.

[78] Pengjie Zhang, Ue-Li Pen, and Hy Trac. Precision era of the kinetic Sunyaev–Zel'dovich effect: simulations, analytical models and observations and the power to constrain reionization. *Monthly Notices of the Royal Astronomical Society*, 347(4):1224–1233, 02 2004.

[79] Matthew McQuinn, Steven R. Furlanetto, Lars Hernquist, Oliver Zahn, and Matias Zaldarriaga. The kinetic sunyaev-zel'dovich effect from reionization. *The Astrophysical Journal*, 630(2):643–656, Sep 2005.

[80] Marcelo A. Alvarez. The Kinetic Sunyaev–Zel'dovich Effect From Reionization: Simulated Full-sky Maps at Arcminute Resolution. *Astrophys. J.*, 824(2):118, 2016.

[81] Asantha Cooray and Michael Kesden. Weak lensing of the cmb: Extraction of lensing information from the trispectrum. *New Astronomy*, 8(3):231–253, 2003.

[82] Michael H. Kesden, Asantha Cooray, and Marc Kamionkowski. Weak lensing of the CMB: Cumulants of the probability distribution function. *Phys. Rev. D*, 66:083007, 2002.

[83] Sean M. Carroll, George B. Field, and Roman Jackiw. Limits on a lorentz- and parity-violating modification of electrodynamics. *Phys. Rev. D*, 41:1231–1240, Feb 1990.

[84] Arthur Lue, Limin Wang, and Marc Kamionkowski. Cosmological signature of new parity-violating interactions. *Phys. Rev. Lett.*, 83:1506–1509, Aug 1999.

[85] Maxim Pospelov, Adam Ritz, and Constantinos Skordis. Pseudoscalar perturbations and polarization of the cosmic microwave background. *Phys. Rev. Lett.*, 103:051302, Jul 2009.

[86] Fabio Finelli and Matteo Galaverni. Rotation of linear polarization plane and circular polarization from cosmological pseudoscalar fields. Phys. Rev. D, 79(6):063002, March 2009.

[87] Mingzhe Li and Xinmin Zhang. Cosmological CPT violating effect on CMB polarization. Phys. Rev. D, 78(10):103516, November 2008.

[88] Ludovico M. Capparelli, Robert R. Caldwell, and Alessandro Melchiorri. Cosmic birefringence test of the Hubble tension. Phys. Rev. D, 101(12):123529, June 2020.

[89] Sean M. Carroll. Quintessence and the rest of the world: Suppressing long-range interactions. *Phys. Rev. Lett.*, 81:3067–3070, Oct 1998.

[90] Arthur Kosowsky and Abraham Loeb. Faraday Rotation of Microwave Background Polarization by a Primordial Magnetic Field. *The Astrophysical Journal*, 469:1, 1996.

[91] Hua Zhai, Si-Yu Li, Mingzhe Li, Hong Li, and Xinmin Zhang. The effects on CMB power spectra and bispectra from the polarization rotation and its correlations with temperature and E-polarization. J. Cosmology Astropart. Phys., 2020(12):051, December 2020.

[92] N. Aghanim et al. Planck intermediate results. XLIX. Parity-violation constraints from polarization data. *Astron. Astrophys.*, 596:A110, 2016.

[93] E. Komatsu, K. M. Smith, J. Dunkley, C. L. Bennett, B. Gold, G. Hinshaw, N. Jarosik, D. Larson, M. R. Nolta, L. Page, and et al. Seven-year wilkinson microwave anisotropy

probe (wmap) observations: Cosmological interpretation. *The Astrophysical Journal Supplement Series*, 192(2):18, Jan 2011.

[94] Steve K. Choi et al. The Atacama Cosmology Telescope: a measurement of the Cosmic Microwave Background power spectra at 98 and 150 GHz. *JCAP*, 12:045, 2020.

[95] Brian G. Keating, Meir Shimon, and Amit P. S. Yadav. Self-calibration of Cosmic Microwave Background Polarization Experiments. ApJ, 762(2):L23, January 2013.

[96] J. P. Kaufman, N. J. Miller, M. Shimon, D. Barkats, C. Bischoff, I. Buder, B. G. Keating, J. M. Kovac, P. A. R. Ade, R. Aikin, J. O. Battle, E. M. Bierman, J. J. Bock, H. C. Chiang, C. D. Dowell, L. Duband, J. Filippini, E. F. Hivon, W. L. Holzapfel, V. V. Hristov, W. C. Jones, S. S. Kernasovskiy, C. L. Kuo, E. M. Leitch, P. V. Mason, T. Matsumura, H. T. Nguyen, N. Ponthieu, C. Pryke, S. Richter, G. Rocha, C. Sheehy, M. Su, Y. D. Takahashi, J. E. Tolan, and K. W. Yoon. Self-calibration of BICEP1 three-year data and constraints on astrophysical polarization rotation. Phys. Rev. D, 89(6):062006, March 2014.

[97] Vera Gluscevic, Marc Kamionkowski, and Asantha Cooray. Derotation of the cosmic microwave background polarization: Full-sky formalism. Phys. Rev. D, 80(2):023510, July 2009.

[98] Amit Yadav, Levon Pogosian, and Tanmay Vachaspati. Probing primordial magnetism with off-diagonal correlators of CMB polarization. Phys. Rev. D, 86(12):123009, December 2012.

[99] Toshiya Namikawa. Testing parity-violating physics from cosmic rotation power reconstruction. Phys. Rev. D, 95(4):043523, February 2017.

[100] Planck Collaboration, N. Aghanim, M. Ashdown, J. Aumont, C. Baccigalupi, M. Ballardini, A. J. Banday, R. B. Barreiro, N. Bartolo, S. Basak, K. Benabed, J. P. Bernard, M. Bersanelli, P. Bielewicz, L. Bonavera, J. R. Bond, J. Borrill, F. R. Bouchet, C. Burigana, E. Calabrese, J. F. Cardoso, J. Carron, H. C. Chiang, L. P. L. Colombo, B. Comis, D. Contreras, F. Couchot, A. Coulais, B. P. Crill, A. Curto, F. Cuttaia, P. de Bernardis, A. de Rosa, G. de Zotti, J. Delabrouille, F. X. Désert, E. Di Valentino, C. Dickinson, J. M. Diego, O. Doré, A. Ducout, X. Dupac, S. Dusini, F. Elsner, T. A. Enßlin, H. K. Eriksen, Y. Fantaye, F. Finelli, F. Forastieri, M. Frailis, E. Franceschi, A. Frolov, S. Galeotta, S. Galli, K. Ganga, R. T. Génova-Santos, M. Gerbino, Y. Giraud-Héraud, J. González-Nuevo, K. M. Górski, A. Gruppuso, J. E. Gudmundsson, F. K. Hansen, S. Henrot-Versillé, D. Herranz, E. Hivon, Z. Huang, A. H. Jaffe, W. C. Jones, E. Keihänen, R. Keskitalo, K. Kiiveri, N. Krachmalnicoff, M. Kunz, H. Kurki-Suonio, J. M. Lamarre, M. Langer, A. Lasenby, M. Lattanzi, C. R. Lawrence, M. Le Jeune, J. P. Leahy, F. Levrier, M. Liguori, P. B. Lilje, V. Lindholm, M. López-Caniego, Y. Z. Ma, J. F. Macías-Pérez, G. Maggio, D. Maino, N. Mandolesi, M. Maris, P. G. Martin, E. Martínez-González, S. Matarrese, N. Mauri, J. D. McEwen, P. R. Meinhold, A. Melchiorri, A. Mennella, M. Migliaccio,

M. A. Miville-Deschênes, D. Molinari, A. Moneti, G. Morgante, A. Moss, P. Natoli, L. Pagano, D. Paoletti, G. Patanchon, L. Patrizii, L. Perotto, V. Pettorino, F. Piacentini, L. Polastri, G. Polenta, J. P. Rachen, B. Racine, M. Reinecke, M. Remazeilles, A. Renzi, G. Rocha, C. Rosset, M. Rossetti, G. Roudier, J. A. Rubiño-Martín, B. Ruiz-Granados, M. Sandri, M. Savelainen, D. Scott, C. Sirignano, G. Sirri, L. D. Spencer, A. S. Suur-Uski, J. A. Tauber, D. Tavagnacco, M. Tenti, L. Toffolatti, M. Tomasi, M. Tristram, T. Trombetti, J. Valiviita, F. Van Tent, P. Vielva, F. Villa, N. Vittorio, B. D. Wandelt, I. K. Wehus, A. Zacchei, and A. Zonca. Planck intermediate results. XLIX. Parity-violation constraints from polarization data. A&A, 596:A110, December 2016.

[101] BICEP2 Collaboration, Keck Array Collaboration, P. A. R. Ade, Z. Ahmed, R. W. Aikin, K. D. Alexander, D. Barkats, S. J. Benton, C. A. Bischoff, J. J. Bock, R. Bowens-Rubin, J. A. Brevik, I. Buder, E. Bullock, V. Buza, J. Connors, B. P. Crill, L. Duband, C. Dvorkin, J. P. Filippini, S. Fliescher, T. St. Germaine, T. Ghosh, J. Grayson, S. Harrison, S. R. Hildebrandt, G. C. Hilton, H. Hui, K. D. Irwin, J. Kang, K. S. Karkare, E. Karpel, J. P. Kaufman, B. G. Keating, S. Kefeli, S. A. Kernasovskiy, J. M. Kovac, C. L. Kuo, N. Larson, E. M. Leitch, K. G. Megerian, L. Moncelsi, T. Namikawa, C. B. Netterfield, H. T. Nguyen, R. O'Brient, R. W. Ogburn, C. Pryke, S. Richter, A. Schillaci, R. Schwarz, C. D. Sheehy, Z. K. Staniszewski, B. Steinbach, R. V. Sudiwala, G. P. Teply, K. L. Thompson, J. E. Tolan, C. Tucker, A. D. Turner, A. G. Vieregg, A. C. Weber, D. V. Wiebe, J. Willmert, C. L. Wong, W. L. K. Wu, and K. W. Yoon. BICEP2 / Keck Array IX: New bounds on anisotropies of CMB polarization rotation and implications for axionlike particles and primordial magnetic fields. Phys. Rev. D, 96(10):102003, November 2017.

[102] F. Bianchini, W. L. K. Wu, P. A. R. Ade, A. J. Anderson, J. E. Austermann, J. S. Avva, L. Balkenhol, E. Baxter, J. A. Beall, A. N. Bender, B. A. Benson, L. E. Bleem, J. E. Carlstrom, C. L. Chang, P. Chaubal, H. C. Chiang, T. L. Chou, R. Citron, C. Corbett Moran, T. M. Crawford, A. T. Crites, T. de Haan, M. A. Dobbs, W. Everett, J. Gallicchio, E. M. George, A. Gilbert, N. Gupta, N. W. Halverson, J. W. Henning, G. C. Hilton, G. P. Holder, W. L. Holzapfel, J. D. Hrubes, N. Huang, J. Hubmayr, K. D. Irwin, L. Knox, A. T. Lee, D. Li, A. Lowitz, A. Manzotti, J. J. McMahon, S. S. Meyer, M. Millea, L. M. Mocanu, J. Montgomery, A. Nadolski, T. Natoli, J. P. Nibarger, G. Noble, V. Novosad, Y. Omori, S. Padin, S. Patil, C. Pryke, C. L. Reichardt, J. E. Ruhl, B. R. Saliwanchik, K. K. Schaffer, C. Sievers, G. Simard, G. Smecher, A. A. Stark, K. T. Story, C. Tucker, K. Vanderlinde, T. Veach, J. D. Vieira, G. Wang, N. Whitehorn, and V. Yefremenko. Searching for anisotropic cosmic birefringence with polarization data from SPTpol. Phys. Rev. D, 102(8):083504, October 2020.

[103] Julien Lesgourgues. The Cosmic Linear Anisotropy Solving System (CLASS) I: Overview. 2011.

[104] Mingzhe Li and Bo Yu. New constraints on anisotropic rotation of CMB polarization. J. Cosmology Astropart. Phys., 2013(6):016, June 2013.

[105] Don Colladay and V. Alan Kostelecký. CPT violation and the standard model. Phys. Rev. D, 55(11):6760–6774, June 1997.

[106] D. Colladay and V. Alan Kostelecký. Lorentz-violating extension of the standard model. Phys. Rev. D, 58(11):116002, December 1998.

[107] David Leon, Jonathan Kaufman, Brian Keating, and Matthew Mewes. The cosmic microwave background and pseudo-Nambu-Goldstone bosons: Searching for Lorentz violations in the cosmos. *Modern Physics Letters A*, 32(2):1730002, January 2017.

[108] Robert R. Caldwell, Vera Gluscevic, and Marc Kamionkowski. Cross-correlation of cosmological birefringence with CMB temperature. Phys. Rev. D, 84(4):043504, August 2011.

[109] Anthony Challinor and Antony Lewis. Lensed CMB power spectra from all-sky correlation functions. Phys. Rev. D, 71(10):103010, May 2005.

[110] Kendrick M. Smith, Duncan Hanson, Marilena LoVerde, Christopher M. Hirata, and Oliver Zahn. Delensing CMB polarization with external datasets. J. Cosmology Astropart. Phys., 2012(6):014, June 2012.

[111] Planck Collaboration, N. Aghanim, Y. Akrami, M. Ashdown, J. Aumont, et al. Planck 2018 results. VI. Cosmological parameters. 2018.

[112] Sigurd Naess, Mathew Madhavacheril, and Matthew Hasselfield. Pixell: Rectangular pixel map manipulation and harmonic analysis library, February 2021.

[113] Ruth Durrer and Andrii Neronov. Cosmological magnetic fields: their generation, evolution and observation. A&A Rev., 21:62, June 2013.

[114] Peter Ade, James Aguirre, Zeeshan Ahmed, Simone Aiola, Aamir Ali, et al. The Simons Observatory: Science goals and forecasts. *Journal of Cosmology and Astroparticle Physics*, 2019(2), 2019.

[115] Kevork N. Abazajian, Peter Adshead, Zeeshan Ahmed, Steven W. Allen, David Alonso, et al. CMB-S4 Science Book, First Edition. oct 2016.

[116] Hongbo Cai, Yilun Guan, Toshiya Namikawa, and Arthur Kosowsky. Impact of anisotropic birefringence on measuring cosmic microwave background lensing. *Phys. Rev. D*, 107(4):043513, 2023.

[117] Planck Collaboration, N. Aghanim, Y. Akrami, M. Ashdown, J. Aumont, C. Baccigalupi, M. Ballardini, A. J. Banday, R. B. Barreiro, N. Bartolo, S. Basak, K. Benabed, J. P. Bernard, M. Bersanelli, P. Bielewicz, J. J. Bock, J. R. Bond, J. Borrill, F. R. Bouchet, F. Boulanger, M. Bucher, C. Burigana, E. Calabrese, J. F. Cardoso, J. Carron, A. Challinor, H. C. Chiang, L. P. L. Colombo, C. Combet, B. P. Crill, F. Cuttaia, P. de Bernardis, G. de Zotti, J. Delabrouille, E. Di Valentino, J. M. Diego, O. Doré,

M. Douspis, A. Ducout, X. Dupac, G. Efstathiou, F. Elsner, T. A. Enßlin, H. K. Eriksen, Y. Fantaye, R. Fernandez-Cobos, F. Finelli, F. Forastieri, M. Frailis, A. A. Fraisse, E. Franceschi, A. Frolov, S. Galeotta, S. Galli, K. Ganga, R. T. Génova-Santos, M. Gerbino, T. Ghosh, J. González-Nuevo, K. M. Górski, S. Gratton, A. Gruppuso, J. E. Gudmundsson, J. Hamann, W. Handley, F. K. Hansen, D. Herranz, E. Hivon, Z. Huang, A. H. Jaffe, W. C. Jones, A. Karakci, E. Keihänen, R. Keskitalo, K. Kiiveri, J. Kim, L. Knox, N. Krachmalnicoff, M. Kunz, H. Kurki-Suonio, G. Lagache, J. M. Lamarre, A. Lasenby, M. Lattanzi, C. R. Lawrence, M. Le Jeune, F. Levrier, A. Lewis, M. Liguori, P. B. Lilje, V. Lindholm, M. López-Caniego, P. M. Lubin, Y. Z. Ma, J. F. Macías-Pérez, G. Maggio, D. Maino, N. Mandolesi, A. Mangilli, A. Marcos-Caballero, M. Maris, P. G. Martin, E. Martínez-González, S. Matarrese, N. Mauri, J. D. McEwen, A. Melchiorri, A. Mennella, M. Migliaccio, M. A. Miville-Deschênes, D. Molinari, A. Moneti, L. Montier, G. Morgante, A. Moss, P. Natoli, L. Pagano, D. Paoletti, B. Partridge, G. Patanchon, F. Perrotta, V. Pettorino, F. Piacentini, L. Polastri, G. Polenta, J. L. Puget, J. P. Rachen, M. Reinecke, M. Remazeilles, A. Renzi, G. Rocha, C. Rosset, G. Roudier, J. A. Rubiño-Martín, B. Ruiz-Granados, L. Salvati, M. Sandri, M. Savelainen, D. Scott, C. Sirignano, R. Sunyaev, A. S. Suur-Uski, J. A. Tauber, D. Tavagnacco, M. Tenti, L. Toffolatti, M. Tomasi, T. Trombetti, J. Valiviita, B. Van Tent, P. Vielva, F. Villa, N. Vittorio, B. D. Wandelt, I. K. Wehus, M. White, S. D. M. White, A. Zacchei, and A. Zonca. Planck 2018 results. VIII. Gravitational lensing. A&A, 641:A8, September 2020.

[118] Planck Collaboration, P. A. R. Ade, N. Aghanim, C. Armitage-Caplan, M. Arnaud, M. Ashdown, F. Atrio-Barandela, J. Aumont, C. Baccigalupi, A. J. Banday, and et al. Planck 2013 results. XVII. Gravitational lensing by large-scale structure. A&A, 571:A17, November 2014.

[119] Alexander van Engelen, Blake D. Sherwin, Neelima Sehgal, Graeme E. Addison, Rupert Allison, Nick Battaglia, Francesco de Bernardis, J. Richard Bond, Erminia Calabrese, Kevin Coughlin, Devin Crichton, Rahul Datta, Mark J. Devlin, Joanna Dunkley, Rolando Dünner, Patricio Gallardo, Emily Grace, Megan Gralla, Amir Hajian, Matthew Hasselfield, Shawn Henderson, J. Colin Hill, Matt Hilton, Adam D. Hincks, Renée Hlozek, Kevin M. Huffenberger, John P. Hughes, Brian Koopman, Arthur Kosowsky, Thibaut Louis, Marius Lungu, Mathew Madhavacheril, Loïc Maurin, Jeff McMahon, Kavilan Moodley, Charles Munson, Sigurd Naess, Federico Nati, Laura Newburgh, Michael D. Niemack, Michael R. Nolta, Lyman A. Page, Christine Pappas, Bruce Partridge, Benjamin L. Schmitt, Jonathan L. Sievers, Sara Simon, David N. Spergel, Suzanne T. Staggs, Eric R. Switzer, Jonathan T. Ward, and Edward J. Wollack. The Atacama Cosmology Telescope: Lensing of CMB Temperature and Polarization Derived from Cosmic Infrared Background Cross-correlation. ApJ, 808(1):7, July 2015.

[120] BICEP2 Collaboration, Keck Array Collaboration, P. A. R. Ade, Z. Ahmed, R. W. Aikin, K. D. Alexander, D. Barkats, S. J. Benton, C. A. Bischoff, J. J. Bock, R. Bowens-Rubin, J. A. Brevik, I. Buder, E. Bullock, V. Buza, J. Connors, B. P. Crill,

L. Duband, C. Dvorkin, J. P. Filippini, S. Fliescher, J. Grayson, M. Halpern, S. Harrison, S. R. Hildebrandt, G. C. Hilton, H. Hui, K. D. Irwin, J. Kang, K. S. Karkare, E. Karpel, J. P. Kaufman, B. G. Keating, S. Kefeli, S. A. Kernasovskiy, J. M. Kovac, C. L. Kuo, E. M. Leitch, M. Lueker, K. G. Megerian, T. Namikawa, C. B. Netterfield, H. T. Nguyen, R. O'Brient, IV Ogburn, R. W., A. Orlando, C. Pryke, S. Richter, R. Schwarz, C. D. Sheehy, Z. K. Staniszewski, B. Steinbach, R. V. Sudiwala, G. P. Teply, K. L. Thompson, J. E. Tolan, C. Tucker, A. D. Turner, A. G. Vieregg, A. C. Weber, D. V. Wiebe, J. Willmert, C. L. Wong, W. L. K. Wu, and K. W. Yoon. BICEP2/Keck Array VIII: Measurement of Gravitational Lensing from Large-scale B-mode Polarization. ApJ, 833(2):228, December 2016.

[121] Polarbear Collaboration, P. A. R. Ade, Y. Akiba, A. E. Anthony, K. Arnold, M. Atlas, D. Barron, D. Boettger, J. Borrill, S. Chapman, Y. Chinone, M. Dobbs, T. Elleflot, J. Errard, G. Fabbian, C. Feng, D. Flanigan, A. Gilbert, W. Grainger, N. W. Halverson, M. Hasegawa, K. Hattori, M. Hazumi, W. L. Holzapfel, Y. Hori, J. Howard, P. Hyland, Y. Inoue, G. C. Jaehnig, A. H. Jaffe, B. Keating, Z. Kermish, R. Keskitalo, T. Kisner, M. Le Jeune, A. T. Lee, E. M. Leitch, E. Linder, M. Lungu, F. Matsuda, T. Matsumura, X. Meng, N. J. Miller, H. Morii, S. Moyerman, M. J. Myers, M. Navaroli, H. Nishino, A. Orlando, H. Paar, J. Peloton, D. Poletti, E. Quealy, G. Rebeiz, C. L. Reichardt, P. L. Richards, C. Ross, I. Schanning, D. E. Schenck, B. D. Sherwin, A. Shimizu, C. Shimmin, M. Shimon, P. Siritanasak, G. Smecher, H. Spieler, N. Stebor, B. Steinbach, R. Stompor, A. Suzuki, S. Takakura, T. Tomaru, B. Wilson, A. Yadav, and O. Zahn. A Measurement of the Cosmic Microwave Background B-mode Polarization Power Spectrum at Sub-degree Scales with POLARBEAR. ApJ, 794(2):171, October 2014.

[122] POLARBEAR Collaboration, P. A. R. Ade, M. Aguilar, Y. Akiba, K. Arnold, C. Baccigalupi, D. Barron, D. Beck, F. Bianchini, D. Boettger, J. Borrill, S. Chapman, Y. Chinone, K. Crowley, A. Cukierman, R. Dünner, M. Dobbs, A. Ducout, T. Elleflot, J. Errard, G. Fabbian, S. M. Feeney, C. Feng, T. Fujino, N. Galitzki, A. Gilbert, N. Goeckner-Wald, J. C. Groh, G. Hall, N. Halverson, T. Hamada, M. Hasegawa, M. Hazumi, C. A. Hill, L. Howe, Y. Inoue, G. Jaehnig, A. H. Jaffe, O. Jeong, D. Kaneko, N. Katayama, B. Keating, R. Keskitalo, T. Kisner, N. Krachmalnicoff, A. Kusaka, M. Le Jeune, A. T. Lee, E. M. Leitch, D. Leon, E. Linder, L. Lowry, F. Matsuda, T. Matsumura, Y. Minami, J. Montgomery, M. Navaroli, H. Nishino, H. Paar, J. Peloton, A. T. P. Pham, D. Poletti, G. Puglisi, C. L. Reichardt, P. L. Richards, C. Ross, Y. Segawa, B. D. Sherwin, M. Silva-Feaver, P. Siritanasak, N. Stebor, R. Stompor, A. Suzuki, O. Tajima, S. Takakura, S. Takatori, D. Tanabe, G. P. Teply, T. Tomaru, C. Tucker, N. Whitehorn, and A. Zahn. A Measurement of the Cosmic Microwave Background B-mode Polarization Power Spectrum at Subdegree Scales from Two Years of polarbear Data. ApJ, 848(2):121, October 2017.

[123] K. T. Story, D. Hanson, P. A. R. Ade, K. A. Aird, J. E. Austermann, J. A. Beall, A. N. Bender, B. A. Benson, L. E. Bleem, J. E. Carlstrom, C. L. Chang, H. C. Chiang, H. M. Cho, R. Citron, T. M. Crawford, A. T. Crites, T. de Haan, M. A. Dobbs, W. Everett,

J. Gallicchio, J. Gao, E. M. George, A. Gilbert, N. W. Halverson, N. Harrington, J. W. Henning, G. C. Hilton, G. P. Holder, W. L. Holzapfel, S. Hoover, Z. Hou, J. D. Hrubes, N. Huang, J. Hubmayr, K. D. Irwin, R. Keisler, L. Knox, A. T. Lee, E. M. Leitch, D. Li, C. Liang, D. Luong-Van, J. J. McMahon, J. Mehl, S. S. Meyer, L. Mocanu, T. E. Montroy, T. Natoli, J. P. Nibarger, V. Novosad, S. Padin, C. Pryke, C. L. Reichardt, J. E. Ruhl, B. R. Saliwanchik, J. T. Sayre, K. K. Schaffer, G. Smecher, A. A. Stark, C. Tucker, K. Vanderlinde, J. D. Vieira, G. Wang, N. Whitehorn, V. Yefremenko, and O. Zahn. A Measurement of the Cosmic Microwave Background Gravitational Lensing Potential from 100 Square Degrees of SPTpol Data. ApJ, 810(1):50, September 2015.

[124] Kevork N. Abazajian, Peter Adshead, Zeeshan Ahmed, Steven W. Allen, David Alonso, Kam S. Arnold, Carlo Baccigalupi, James G. Bartlett, Nicholas Battaglia, Bradford A. Benson, Colin A. Bischoff, Julian Borrill, Victor Buza, Erminia Calabrese, Robert Caldwell, John E. Carlstrom, Clarence L. Chang, Thomas M. Crawford, Francis-Yan Cyr-Racine, Francesco De Bernardis, Tijmen de Haan, Sperello di Serego Alighieri, Joanna Dunkley, Cora Dvorkin, Josquin Errard, Giulio Fabbian, Stephen Feeney, Simone Ferraro, Jeffrey P. Filippini, Raphael Flauger, George M. Fuller, Vera Gluscevic, Daniel Green, Daniel Grin, Evan Grohs, Jason W. Henning, J. Colin Hill, Renee Hlozek, Gilbert Holder, William Holzapfel, Wayne Hu, Kevin M. Huffenberger, Reijo Keskitalo, Lloyd Knox, Arthur Kosowsky, John Kovac, Ely D. Kovetz, Chao-Lin Kuo, Akito Kusaka, Maude Le Jeune, Adrian T. Lee, Marc Lilley, Marilena Loverde, Mathew S. Madhavacheril, Adam Mantz, David J. E. Marsh, Jeffrey McMahon, Pieter Daniel Meerburg, Joel Meyers, Amber D. Miller, Julian B. Munoz, Ho Nam Nguyen, Michael D. Niemack, Marco Peloso, Julien Peloton, Levon Pogosian, Clement Pryke, Marco Raveri, Christian L. Reichardt, Graca Rocha, Aditya Rotti, Emmanuel Schaan, Marcel M. Schmittfull, Douglas Scott, Neelima Sehgal, Sarah Shandera, Blake D. Sherwin, Tristan L. Smith, Lorenzo Sorbo, Glenn D. Starkman, Kyle T. Story, Alexander van Engelen, Joaquin D. Vieira, Scott Watson, Nathan Whitehorn, and W. L. Kimmy Wu. CMB-S4 Science Book, First Edition. *arXiv e-prints*, page arXiv:1610.02743, October 2016.

[125] Mark Mirmelstein, Giulio Fabbian, Antony Lewis, and Julien Peloton. Instrumental systematics biases in CMB lensing reconstruction: A simulation-based assessment. *Phys. Rev. D*, 103(12):123540, 2021.

[126] Ryo Nagata and Toshiya Namikawa. A numerical study of observational systematic errors in lensing analysis of CMB polarization. *Progress of Theoretical and Experimental Physics*, 2021(5):053E01, May 2021.

[127] Yuto Minami and Eiichiro Komatsu. New Extraction of the Cosmic Birefringence from the Planck 2018 Polarization Data. *Phys. Rev. Lett.*, 125(22):221301, 2020.

[128] P. Diego-Palazuelos et al. Cosmic Birefringence from the Planck Data Release 4. *Phys. Rev. Lett.*, 128(9):091302, 2022.

[129] Johannes R. Eskilt and Eiichiro Komatsu. Improved Constraints on Cosmic Birefrin-

gence from the WMAP and Planck Cosmic Microwave Background Polarization Data. 5 2022.

[130] Eiichiro Komatsu. New physics from the polarized light of the cosmic microwave background. *Nature Rev. Phys.*, 4(7):452–469, 2022.

[131] Blake D. Sherwin and Toshiya Namikawa. Cosmic birefringence tomography and calibration-independence with reionization signals in the CMB. *arXiv e-prints*, page arXiv:2108.09287, August 2021.

[132] Hiromasa Nakatsuka, Toshiya Namikawa, and Eiichiro Komatsu. Is cosmic birefringence due to dark energy or dark matter? A tomographic approach. *Phys. Rev. D*, 105(12):123509, 2022.

[133] Nanoom Lee, Selim C. Hotinli, and Marc Kamionkowski. Probing Cosmic Birefringence with Polarized Sunyaev Zel'dovich Tomography. 7 2022.

[134] Silvia Gasparotto and Ippei Obata. Cosmic birefringence from monodromic axion dark energy. *JCAP*, 08(08):025, 2022.

[135] Tomohiro Fujita, Yuto Minami, Kai Murai, and Hiromasa Nakatsuka. Probing Axion-like Particles via CMB Polarization. *arXiv e-prints*, page arXiv:2008.02473, August 2020.

[136] Naoya Kitajima, Fumiaki Kozai, Fuminobu Takahashi, and Wen Yin. Power spectrum of domain-wall network and its implications for isotropic and anisotropic cosmic birefringence. 5 2022.

[137] Mudit Jain, Ray Hagimoto, Andrew J. Long, and Mustafa A. Amin. Searching for axion-like particles through CMB birefringence from string-wall networks. 8 2022.

[138] Marc Kamionkowski. How to Derotate the Cosmic Microwave Background Polarization. Phys. Rev. Lett., 102(11):111302, March 2009.

[139] Arthur Kosowsky, Tina Kahniashvili, George Lavrelashvili, and Bharat Ratra. Faraday rotation of the Cosmic Microwave Background polarization by a stochastic magnetic field. *Phys. Rev. D*, 71:043006, 2005.

[140] Amit Yadav, Levon Pogosian, and Tanmay Vachaspati. Probing primordial magnetism with off-diagonal correlators of CMB polarization. Phys. Rev. D, 86(12):123009, December 2012.

[141] Soma De, Levon Pogosian, and Tanmay Vachaspati. CMB Faraday rotation as seen through the Milky Way. *Phys. Rev. D*, 88(6):063527, 2013.

[142] Levon Pogosian. Searching for primordial magnetism with multifrequency cosmic microwave background experiments. *Mon. Not. Roy. Astron. Soc.*, 438(3):2508–2512, 2014.

[143] Simone Aiola et al. Snowmass2021 CMB-HD White Paper. 3 2022.

[144] Levon Pogosian, Meir Shimon, Matthew Mewes, and Brian Keating. Future CMB constraints on cosmic birefringence and implications for fundamental physics. *Phys. Rev. D*, 100(2):023507, 2019.

[145] Mingzhe Li and Bo Yu. New Constraints on Anisotropic Rotation of CMB Polarization. *JCAP*, 06:016, 2013.

[146] Toshiya Namikawa. cmblensplus: Cosmic microwave background tools. Astrophysics Source Code Library, record ascl:2104.021, April 2021.

[147] Lloyd Knox. Determination of inflationary observables by cosmic microwave background anisotropy experiments. *Phys. Rev. D*, 52:4307–4318, Oct 1995.

[148] Michael Kesden, Asantha Cooray, and Marc Kamionkowski. Lensing reconstruction with CMB temperature and polarization. Phys. Rev. D, 67(12):123507, June 2003.

[149] Duncan Hanson, Anthony Challinor, George Efstathiou, and Pawel Bielewicz. Cmb temperature lensing power reconstruction. *Phys. Rev. D*, 83:043005, Feb 2011.

[150] Francesco De Bernardis, Thomas D. Kitching, Alan Heavens, and Alessandro Melchiorri. Determining the Neutrino Mass Hierarchy with Cosmology. *Phys. Rev. D*, 80:123509, 2009.

[151] K. N. Abazajian et al. Neutrino Physics from the Cosmic Microwave Background and Large Scale Structure. *Astropart. Phys.*, 63:66–80, 2015.

[152] P. A. R. Ade et al. Planck 2015 results. XV. Gravitational lensing. *Astron. Astrophys.*, 594:A15, 2016.

[153] Toshiya Namikawa and Ryuichi Takahashi. Bias-Hardened CMB Lensing with Polarization. *Mon. Not. Roy. Astron. Soc.*, 438(2):1507–1517, 2014.

[154] Toshiya Namikawa and Ryuichi Takahashi. Bias-Hardened CMB Lensing with Polarization. *Mon. Not. Roy. Astron. Soc.*, 438(2):1507–1517, 2014.

[155] Luca Amendola. Non-Gaussian likelihood function and COBE data. *Monthly Notices of the Royal Astronomical Society*, 283(3):983–989, 12 1996.

[156] D. M. Regan, E. P. S. Shellard, and J. R. Fergusson. General cmb and primordial trispectrum estimation. *Phys. Rev. D*, 82:023520, Jul 2010.